

# Improving electrical characteristics of graphene neural electrode

with nanoparticles and doping

Merlin Palmar



# Improving electrical characteristics of graphene neural electrode

with nanoparticles and doping

by

Merlin Palmar

to obtain the degree of Master of Science  
in Biomedical Engineering  
at the Delft University of Technology,  
to be defended publicly on Wednesday, May 26, 2021 at 15:00.

Student number: 4946103  
Supervisors: Dr. Vasiliki Giagka  
Dr. ir. Sten Vollebregt  
Nasim Bakhshae Babaroud  
Thesis committee: Prof. dr. ir Wouter A. Serdijn, TU Delft  
Prof. dr. Peter G. Steeneken, TU Delft

*This thesis is confidential and cannot be made public until May 26, 2022.*

An electronic version of this thesis is available at <http://repository.tudelft.nl/>.



# Abstract

Neuroscientists use neural electrodes to explore the working mechanisms of the nervous system. Therefore, ideal electrodes should have a small size and the ability to record and stimulate at a single-cell resolution with low noise. Materials used for fabrication should be flexible and stable for a long period in the biological media. However, conventional recording and stimulation techniques do not have sufficient spatiotemporal resolution for neuroscience research. Combining electrical and optical modalities into one device helps overcome the resolution limits and record more detailed information. For this application, transparent conductive materials are needed.

Graphene is a potential solution due to its advantageous combination of properties, such as high conductivity, transparency, and flexibility. However, important characteristics of recording and stimulation electrodes, such as the impedance and charge injection capacity of graphene electrodes, do not reach the levels of conventional materials. The electrical characteristics of graphene could be improved further with surface modification, chemical doping, or stacking. Each method has been shown to improve the conductivity of graphene, although some affect the transparency of the layer.

In this work, three methods were used to improve the electrical characteristics of multilayer graphene neural electrode without losing transparency or flexibility. These methods include growing a thicker layer of graphene, adding metal nanoparticles to the surface of the electrode, and nitric acid doping of graphene.

For that purpose, graphene electrodes were fabricated on a silicon wafer. The electrical characteristics of these electrodes were assessed with electrochemical impedance spectroscopy, cyclic voltammetry and 4-point probe measurements. Furthermore, the optical transmittance is measured. The improvement methods were then tested on these electrodes, and the performance was evaluated.

Adding metal nanoparticles to the surface of the electrode showed the most promising results. With gold nanoparticles, the impedance at 1 kHz was lowered 82%, and charge storage capacity increased 529%. However, at the same time, 30% of the optical transmittance was lost. With lower nanoparticle density, 6% of transmittance was lost, and 7% of impedance gained. Nitric acid doping did not improve the impedance, but the charge storage capacity was increased up to 66%. Thicker layers of graphene displayed a lower sheet resistance. However, impedance or charge storage capacity were not improved.



# Acknowledgements

The past year has been full of challenges but also accomplishments. I would like to thank everyone who were a part of my improvement for the support and assistance.

First, I would like to express my deepest gratitude to my supervisors Vasso, Sten, and Nasim for introducing me to the world of graphene and neural electrodes, and for the guidance during the project. You have inspired and helped me in every step of the way. The weekly brainstorming sessions on the topic of 'why none of the measurements make sense?' seemed endless, but thanks to your encouragement, the day of my graduation has finally arrived. It has really been a great pleasure to collaborate with you!

I would like to extend my sincere thanks to Andra for attending the weekly meetings and providing her valuable insights.

I am grateful for the EKL staff for all the advice and help in the lab whenever needed.

I would also like to extend my gratitude to VSPARTICLE for allowing me to use their newest nanoprinter.

I would like to thank Leandro for the help with graphene transferring and Joost for the help with printing nanoparticles.

I am grateful that I got to be a part of the ECTM and BE groups. I wish to thank all the people who I met during this year for contributing to my development.

I also wish to thank my office mates and friends for the endless support. I could not have survived the setbacks in lab without the great humor of Shriya, Danai, and Jord. Cesc and Brian always had useful advice to every problem I encountered. Lotte and Jort kept my motivation high at all times. Thank you all!

Finally, I would like to thank my family and Miguel for encouraging and believing in me.

Delft, May 2021  
Merlin Palmar



# Contents

<b>Abstract</b>	<b>ii</b>
<b>Acknowledgements</b>	<b>iv</b>
<b>List of Figures</b>	<b>viii</b>
<b>List of Tables</b>	<b>xi</b>
<b>1 Introduction</b>	<b>1</b>
1.1 Neural activity measurement and tissue stimulation techniques . . . . .	2
1.1.1 Electrical recording and stimulation . . . . .	2
1.1.2 Optogenetics . . . . .	2
1.1.3 Imaging . . . . .	3
1.2 Electrode design evolution . . . . .	3
1.3 Thesis objectives and approach . . . . .	5
1.4 Outline of the report . . . . .	5
<b>2 Characterisation of neural electrodes</b>	<b>6</b>
2.1 Electrode-tissue interface . . . . .	6
2.2 Electrochemical impedance spectroscopy . . . . .	7
2.3 Cyclic Voltammetry . . . . .	9
2.4 Voltage Transients . . . . .	10
2.5 Sheet resistance measurement . . . . .	10
2.6 Optical transmittance . . . . .	11
<b>3 Literature study</b>	<b>12</b>
3.1 Transparent electrode materials . . . . .	12
3.2 Graphene . . . . .	12
3.2.1 Raman Spectroscopy . . . . .	14
3.2.2 Graphene neural electrodes . . . . .	14
3.3 Methods for improving electrical characteristics of graphene electrodes . . . . .	17
3.3.1 Stacking graphene layers . . . . .	17
3.3.2 Chemical doping . . . . .	17
3.3.2.1 Nitric acid doped graphene electrodes . . . . .	18
3.3.3 Surface modification . . . . .	19
3.3.3.1 Porous graphene electrodes . . . . .	20
3.3.3.2 Nanoparticle production methods . . . . .	20
3.3.3.3 Spark Ablation . . . . .	21
3.3.3.4 Nanoparticles on graphene electrodes . . . . .	21
3.4 Summary of the literature review . . . . .	23
<b>4 Methods</b>	<b>25</b>
4.1 Graphene electrodes and van der Pauw structures fabrication . . . . .	25
4.2 Graphene transfer . . . . .	29
4.3 Nanoparticle deposition . . . . .	30
4.4 Nitric acid doping . . . . .	32
4.5 Electrochemical measurements . . . . .	33
4.5.1 Electrochemical impedance spectroscopy . . . . .	34
4.5.2 Cyclic voltammetry . . . . .	34
4.6 Four-point measurements . . . . .	35
4.7 Optical transmittance measurements . . . . .	35

---

<b>5</b>	<b>Results and discussion</b>	<b>36</b>
5.1	Pristine graphene electrodes . . . . .	36
5.1.1	Electrochemical impedance spectroscopy . . . . .	36
5.1.2	Cyclic voltammetry . . . . .	37
5.1.3	Correlation analysis . . . . .	39
5.2	Graphene with different growth times . . . . .	40
5.2.1	Sheet resistance . . . . .	40
5.2.2	Electrochemical characterisation . . . . .	41
5.2.3	Optical transmittance. . . . .	41
5.2.4	Correlation analysis . . . . .	42
5.3	Graphene electrodes with nanoparticles . . . . .	43
5.3.1	Electrochemical impedance spectroscopy . . . . .	43
5.3.2	Cyclic Voltammetry . . . . .	45
5.3.3	Optical transmittance. . . . .	46
5.4	Graphene electrodes doped with nitric acid . . . . .	48
<b>6</b>	<b>Conclusions</b>	<b>49</b>
6.1	Future recommendations. . . . .	50
	<b>References</b>	<b>54</b>
<b>A</b>	<b>Measured sheet resistances for each location</b>	<b>55</b>
<b>B</b>	<b>Measured charge storage capacities before and after adding nanoparticles</b>	<b>57</b>

# List of Figures

1.1	Neural interfaces developed for various therapies [4]	1
1.2	(a) Electrical stimulation activating all neurons around it is illustrated. (b) optogenetic stimulation only affecting the genetically modified cells is depicted [9].	2
1.3	Inflammatory response creates an insulating scar tissue layer around the stiff electrode which disrupts the recording and stimulating [15]	3
1.4	Simultaneous observation of neural activity and vascular changes right under the electrode with transparent and opaque devices [17]	4
1.5	Illustrations of the improvement methods used in this work: (a) adding thickness, (b) depositing nanoparticles on the surface, (c) nitric acid doping	5
2.1	Electric double-layer around the electrode inside an electrolyte [20]	6
2.2	3-electrode setup for EIS and CV measurements [3]	7
2.3	(a) Typical Bode plot for an electrode [3]. (b) Equivalent circuit model of electrode-electrolyte interface.	8
2.4	Different shapes of CV plot according to the charge transfer mechanism. The inset illustrates the applied voltage on the working electrode [23]	9
2.5	CV measurement data expressed on (a) current vs voltage and (b) current vs time plots	9
2.6	Voltage transient measurement. The top graph indicates the stimulation current pulses and the bottom graph illustrates the voltage response on the electrode [3]	10
2.7	Van der Pauw structure for 4-point probe measurement	11
2.8	Optical transmittance measurement of graphene and chromium on PET substrate	11
3.1	(a) Illustration of the hexagonal graphene lattice. (b) Electronic band structure of graphene and the formation of Dirac cones [33].	13
3.2	Illustration of CVD of graphene in Ni [35]	13
3.3	Raman spectroscopy of graphene on silicon oxide with identifiable D, G, and 2D peaks [40]	14
3.4	Impedance (a), voltage transients (b), and cyclic voltammetry (c) measurements on graphene, gold, and gold with graphene coating [40, 43]	15
3.5	(a) Transmittance of stacked graphene monolayers (SLG) and bilayers (BLG). (b) Sheet resistance of stacked undoped and nitric acid doped monolayers (SLG) and bilayers (BLG) [49].	17
3.6	(a) Optical transmittance dependence on the number of layers and nitric acid doping. Sheet resistance dependence on the number of layers and nitric acid doping [50].	18
3.7	Impedance at 1kHz for graphene doped with different concentrations of nitric acid [47].	18
3.8	Cyclic voltammetry (a) and impedance (b) measurements on gold, graphene, and nitric acid doped graphene [54].	19
3.9	Calcium imaging with confocal and two-photon microscopy. Nitric acid doped graphene electrode can be seen as a square with darker edges. The cells under the electrode are clearly visible [54]	19
3.10	Porous graphene achieved with laser pyrolysis. Scale bar: $2\mu\text{m}$ . [26]	20
3.11	Spark ablation technique to create nanoparticles.	21
3.12	(a) Sheet resistance and transmittance measurements of pristine (black), nitric acid doped (blue), and gold doped (red) graphene. The numbers in the markers indicate the number of graphene layers. (b) Stability assessment showing the change in sheet resistance over time [60].	21
3.13	Scanning electron microscope images of platinum nanoparticles on graphene. a–c) coverage 14.65%, 67.27%, and 88.22% of the graphene surface for 5, 20, 50 s depositions respectively [29]	22

3.14	EIS, CV, and transmittance measurements for gold (magenta) bare graphene (black) and graphene with platinum nanoparticles with various deposition durations [29]	22
4.1	(a) Mask for Mo etching with graphene structures design. (b) Mask for openings of electrodes and contact pads.	26
4.2	(a) Raman spectroscopy of graphene grown at 915 °C. (b) Raman spectroscopy of graphene grown with bottom heater at 950°C and top heater at 1050°C.	26
4.3	Etching of Mo only from the electrodes by only half of the device being inside the $H_2O_2$ .	27
4.4	The final structure of the graphene electrode device. On the close-up image, graphene is with the darker purple color and silicon oxide under it with lighter pinkish color. The yellow circle around the electrode is Mo under photoresist, which is not etched.	27
4.5	The scheme of the fabrication process of graphene electrodes.	28
4.6	(a) A group of six Van der Pauw like structures used for 4-point measurements. (b) Wafer with half implant structures and half van der Pauw structures.	29
4.7	The Mo etching process for graphene transfer to a glass slide.	29
4.8	Graphene grown for 20 min (a), 40 min (b), and 60 min (c) transferred to a glass slide.	30
4.9	(a) VSP-G1 nanoparticle generator and VSP-P1 nanostructured material printer (VS Particle). (b) Devices and a glass slide in the chamber of the printer.	30
4.10	(a) The printing pattern with overlapping lines used in this work. (b) Nanoparticles printed on a glass slide in a 5x5 mm square. The darker dots show the corners of the printed squares.	31
4.11	(a) The original grey-scale SEM image. (b) The SEM image converted to a black-and-white image.	32
4.12	Electrodes (a) and contact pads (b) damaged after nitric acid doping.	32
4.13	(a) The electrode before Mo etching. (b) The electrode after Mo is removed with $H_2O_2$ . (c) The electrode after $HNO_3$ treatment	33
4.14	(a) Three-electrode set up immersed in PBS. (b) Autolab potentiostat used for CV and EIS measurements.	33
4.15	EIS measured against (a) the Ag/AgCl reference electrode and (b) against a platinum wire.	34
4.16	(a) Water reduction is demonstrated at the low voltage. (b) Water oxidation is shown at high voltage. (c) CV with the water window chosen after analysis.	34
4.17	The four-point probe measurement scheme.	35
5.1	Example EIS measurements showing (a) capacitive, (b) resistive, and (c) unexpected behaviour.	37
5.2	Various CV measurement results, where (a) no peaks occur, (b) a negative peak around -0.55 V, and (c) negative peaks around -0.5 V and 0.3 V, and a positive peak around -0.1 V	38
5.3	(a) Cathodic CSC measured at 0.1 V/s correlation with $ Z $ at 1kHz (b) Cathodic CSC measured at 0.1 V/s correlation with $ Z $ at 1kHz. The devices with only graphene on the contact pad are marked with blue (G) and devices with graphene and Mo on the contact pad are marked with orange (Mo+G). The dotted lines in blue and orange are the linear trendlines for G and Mo+G devices, respectively, and the grey dotted lines are trendlines for all the data.	39
5.4	Sheet resistance vs graphene growth time shows lower average $R_s$ and smaller variation for longer growth time	40
5.5	Transmittance of graphene with different growth times	42
5.6	Graphs illustrating correlations between $R_s$ , optical transmittance, and graphene growth time	42
5.7	The $ Z $ at 1 kHz measured before and after adding AuNPs.	43
5.8	The $ Z $ at 1 kHz measured before and after adding Pt NPs. Note that there are two y-axes.	44
5.9	The $ Z $ at 1 kHz measured before and after adding Au+Pt NPs.	44
5.10	The cathodic CSC measured at 0.1 V/s before and after adding Au NPs.	45
5.11	(a) CV with Pt NPs shows water reduction at -0.8 V. (b) CV range reduced to -0.6 V to 0.6 V for CSC calculation	45
5.12	The cathodic CSC measured at 0.1 V/s before and after adding Pt NPs.	46

---

5.13	The cathodic CSC measured at 0.1 V/s before and after adding Au+Pt NPs. . . . .	46
5.14	Optical transmittance measurements of (a) Au NPs, (b) Pt NPs, (c) Au+Pt NPs . . . . .	47
5.15	EIS measurements results (a) before doping, (b) after 69.99% nitric acid doping, (c) after 35% nitric acid doping . . . . .	48
5.16	Cathodic CSC at 0.1 V/s before and after nitric acid doping. . . . .	48
A.1	Wafer with van der Pauw structures. Structures 1 to 27 were used for sheet resistance measurements. . . . .	55
A.2	Sheet resistances in locations 1 to 27 for graphene grown for 20 min . . . . .	56
A.3	Sheet resistances in locations 1 to 27 for graphene grown for 40 min . . . . .	56
A.4	Sheet resistances in locations 1 to 27 for graphene grown for 60 min . . . . .	56

# List of Tables

3.1	Impedance at 1kHz of graphene vs metal electrodes with the same size . . . . .	16
3.2	CSC and CIC of graphene electrodes . . . . .	16
3.3	Improved graphene electrodes . . . . .	23
4.1	The nanoprinter settings and achieved densities of NPs . . . . .	32
5.1	The average impedance magnitude at 1 kHz for pristine graphene electrodes . . . . .	37
5.2	The cathodic CSC . . . . .	38
5.3	The total CSC . . . . .	39
5.4	Sheet resistances for different growth times . . . . .	40
5.5	CSC of 40 min and 60 min graphene electrodes ( $\mu C/cm^2$ ) . . . . .	41
5.6	Optical transmittance of graphene with different growth times . . . . .	42
5.7	$ Z $ at 1 kHz change with Au NPs . . . . .	43
5.8	$ Z $ at 1 kHz change with Pt NPs . . . . .	44
5.9	$ Z $ at 1 kHz change with Au+Pt NPs . . . . .	45
5.10	Optical transmittance . . . . .	47
B.1	CSC before and after adding nanoparticles ( $\mu C/cm^2$ ) . . . . .	58
B.2	CSC before and after nitric acid doping ( $\mu C/cm^2$ ) . . . . .	58

# Introduction

The most complex part of the human body is the nervous system. It controls all the organs and locomotion of the body. After discovering that the nervous system consists of neurons and they communicate with electrical pulses, neural electrodes were developed [1].

Electrodes serve as the interface to the neural tissue for either recording electrical activity or tissue stimulation. Signals emitted by neurons can be detected with recording electrodes. The measured electrical activity provides information about the neural circuitry at a cellular level, as well as knowledge of the physiological processes in health and disease [2]. Furthermore, harvested neural signals can be used to control external hardware, such as artificial limbs [3].

Neural electrodes are also used for stimulation by creating electric fields between two electrodes in the nervous tissue. Modulating neural activity helps to treat various neurological disorders mentioned in figure 1.1 or to replace a lost function such as motor, sensory or cognitive functions [3].

An electrode is a key element in an implantable device since it is the interface between technology and biology. The electrode surface is in physical contact with the tissue, and thus, recording and stimulation abilities are dependent on the properties of that interface [3]. Ideal electrodes should be able to record with a single-cell resolution and with a high signal-to-noise ratio (SNR) for a long period of time and to inject a sufficient amount of charge for stimulation [2]. Materials used for electrode fabrication need to survive in a biological environment without delaminating or corroding [3]. Furthermore, flexible materials should be used which are more similar to the tissue to avoid damage [2].

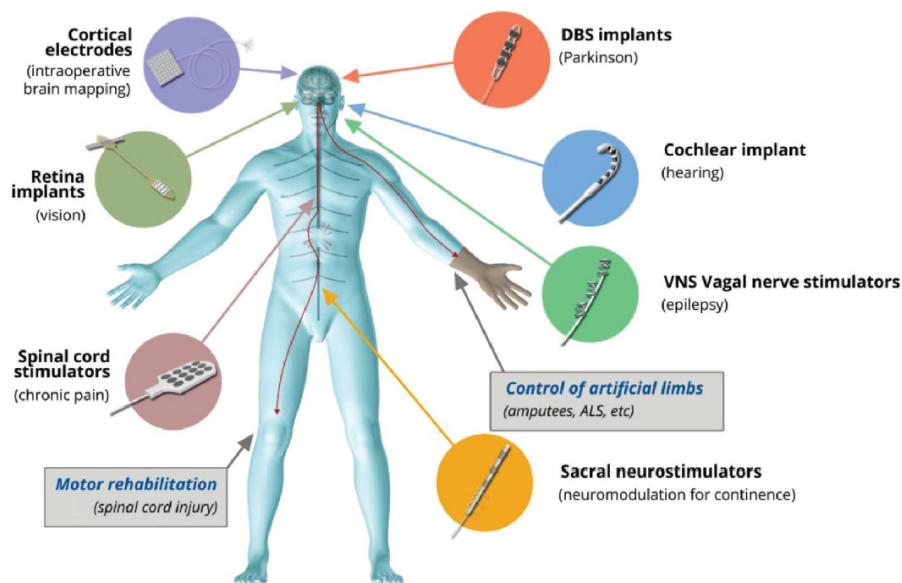


**Figure 1.1:** Neural interfaces developed for various therapies [4]

## 1.1. Neural activity measurement and tissue stimulation techniques

Electrodes are used in neuroscience to research the physiological processes at the cellular level to discover the underlying mechanisms of neurons connections [2]. Various techniques have been developed for recording and stimulating neural tissue.

### 1.1.1. Electrical recording and stimulation

Neurons communicate signals through electrical impulses. Electrical current in the body is created by an ion flow through the cell membrane. Since there are different amounts of positive and negative ions inside and outside of the cell, there is a difference between extracellular and intracellular potential called the membrane potential. The ions can move into and out of the cell through the ion channels in the cell membrane and therefore change the membrane potential. A suprathreshold depolarization of the membrane creates an action potential. This type of impulse will propagate along the axon of the neuron and transmit to other neurons [5]. These changes in the extracellular potential can be detected with an electrode. A recording electrode acts as a transducer, changing the ionic current into electronic current and thus enabling measurement of neuron activation.

During electrical stimulation, an ionic current flow is created in the tissue between 2 electrodes. One electrode serves as the cathode with negative potential, and the other electrode as the anode with positive potential. The created electric field changes the extracellular voltage distribution in the tissue, and therefore, the membrane potential. If then the membrane potential exceeds the threshold, an action potential is created artificially [6]. A downside of electrical stimulation is that focusing is difficult, therefore all structures in the vicinity of the electrode are activated [2].

### 1.1.2. Optogenetics

Investigating neuronal dynamics requires advanced technologies with high-resolution sensing and stimulation capabilities. Conventional methods provide insufficient spatiotemporal resolution for neuroscience research. To have more selective control over which neural structures are activated, optogenetics can be used.

Neurons can be genetically modified with light-sensitive proteins called opsins. These are delivered to the neuron's membrane and act as ion channels or pumps. The neuron is then sensitive to light with a specific wavelength which causes the ion channel to open or pump to activate. That results in depolarization of the cell and the creation of action potential.

Various opsins can be used, each of which reacts to different wavelengths of light [7]. Cell-type-specific control can be achieved by using gene targeting approaches [8]. As opposed to electrical stimulation, only the modified cells are activated, which makes the stimulation more selective, as illustrated in figure 1.2. Thanks to the high spatial and temporal resolution provided by optogenetics, more knowledge about neural circuits can be achieved [7].

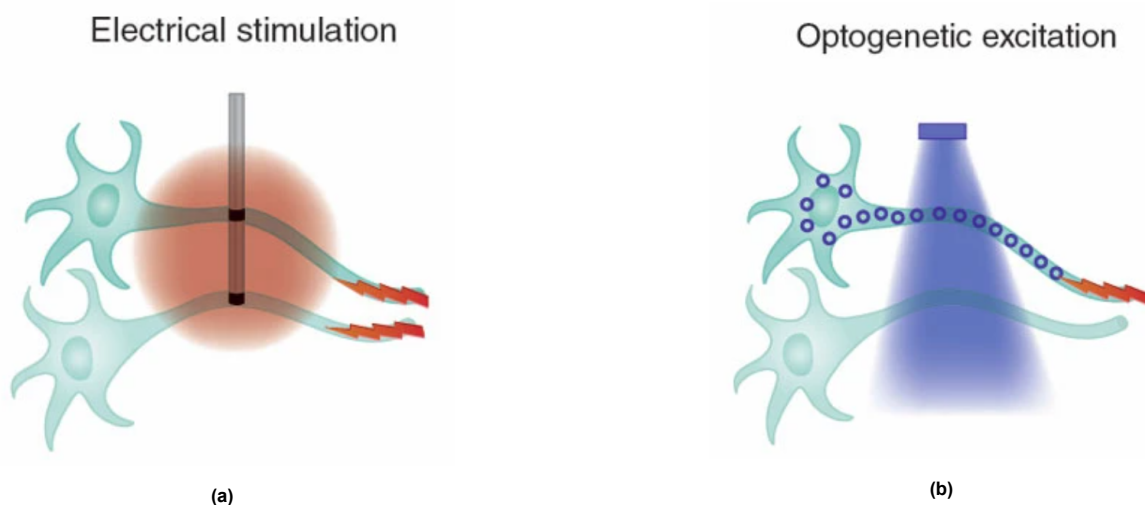


**Figure 1.2:** (a) Electrical stimulation activating all neurons around it is illustrated. (b) optogenetic stimulation only affecting the genetically modified cells is depicted [9].

### 1.1.3. Imaging

Various imaging techniques have been developed to monitor neural activity systematically. The organization of neurons is important to the functionality of the nervous system. Therefore, it is beneficial to monitor many neurons simultaneously to uncover the interconnections between the neurons.

Calcium ions take part in transferring intracellular signals. For calcium imaging, fluorescent indicators are introduced to the nervous tissue that activate when bound with calcium ions. Therefore, when an action potential is created and transferred to another neuron, the number of calcium ions and thus the fluorescence increases. These changes are detectable with microscopy techniques. In combination with two-photon microscopy, it is possible to monitor these indicators also in deep neurons [10].

Other imaging techniques used for noninvasive neuronal activity monitoring are voltage imaging, functional magnetic resonance imaging (MRI), electroencephalogram (EEG)/MRI, positron emission tomography (PET)/computed tomography (CT), and MRI/ magnetoencephalography (MEG) [11, 12].

In vivo imaging techniques can also be used to monitor other biological changes in the tissue, such as vascular changes, development of scar tissue, and microglial activation [13].

## 1.2. Electrode design evolution

Good electrical conductivity is the most important property of electrode materials because it has to transmit electrical signals. Conventionally, metal wires with high conductivity have been used as recording electrodes, such as stainless steel, tungsten, platinum [1, 2]. After that, insulated metal microelectrodes, where only the tip is exposed, were developed. In addition to previously used materials, gold, titanium, titanium nitride, platinum/iridium, iridium oxide were now adopted. Later on, microfabrication processes used for semiconductor technology also became interesting for biomedical applications. The main reason is high accuracy to create patterns with small feature sizes. In this process, a silicon substrate is used where metal electrodes and contacts are deposited. One problem with these types of electrodes is rigidity [1].

Stiff electrodes can damage the tissue during insertion or due to micromotion after implantation and trigger inflammatory reactions, which create an insulating layer of scar tissue around the electrode, as illustrated in figure 1.3 [14]. That results in an increase of the interface impedance, which disrupts the recording of neural signals. To avoid this mechanical mismatch, materials with a low Young's modulus, which is closer to the tissue, should be used [2]. Therefore, the design of implants extended towards flexible forms to reduce the damage to the neural tissue.

Polymer-based materials are being researched for encapsulating metal electrodes, such as Polydimethylsiloxane (PDMS), Parylene C, SU-8, and Polyimide, which are biocompatible and have low Young's modulus [1].

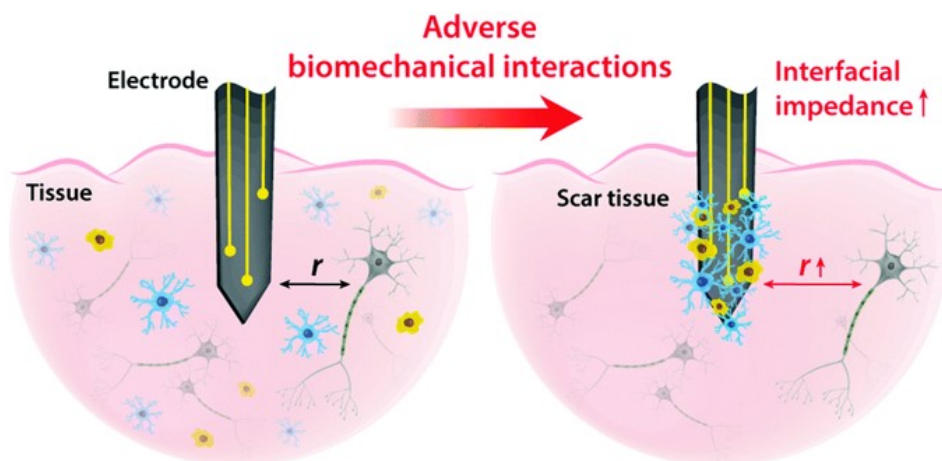


**Figure 1.3:** Inflammatory response creates an insulating scar tissue layer around the stiff electrode which disrupts the recording and stimulating [15]

Another issue with conventional metal electrodes is that they do not have sufficient spatiotemporal resolution for neuroscience research. To overcome the resolution limits, neurotechnologies combining electrical and optical modalities have been proposed [16]. Electrodes fabricated with transparent conductive materials enable stimulating with light and measuring neuronal activity electrically at the same location, or simultaneous electrical stimulation and imaging of the neuronal activity immediately beneath the electrode, which would be very difficult using only the electrical modality. Bringing these techniques together could give more information about the neurons' connections as well as detailed mechanisms of electrical stimulation [17].

It can be seen in figure 1.4 that with metal electrodes we lose some information while imaging that we can still observe with a transparent device. Thus, transparent conductive materials should be used to provide the optimal platform for neural monitoring and stimulating using both electrical and optical modalities.

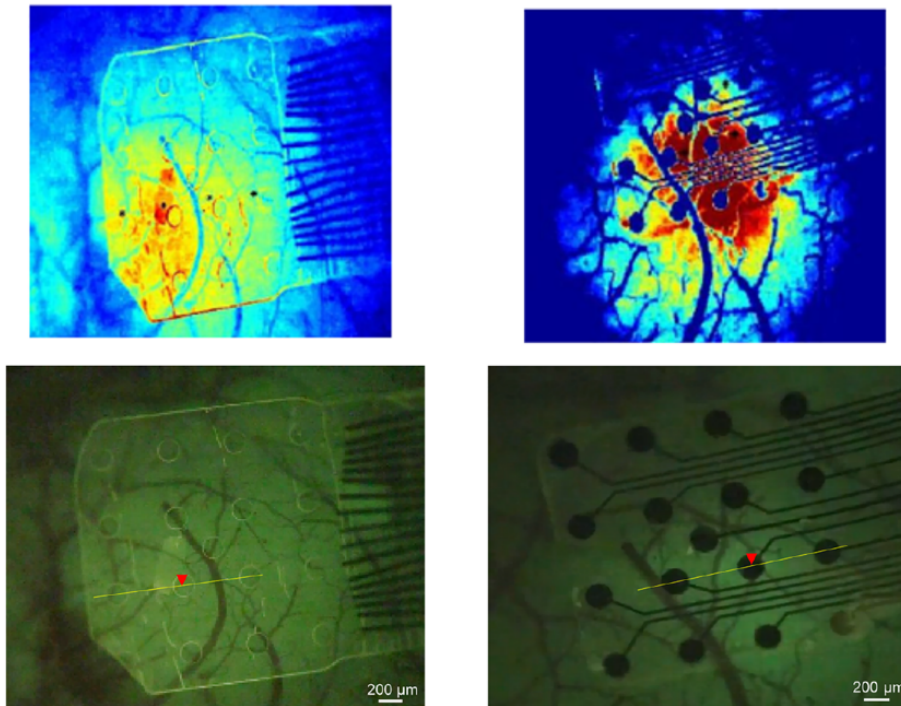


**Figure 1.4:** Simultaneous observation of neural activity and vascular changes right under the electrode with transparent and opaque devices [17]

Transparent and flexible electrodes have been fabricated with various materials such as indium tin oxide (ITO); ultrathin metals or nanostructured metals like gold and platinum, which have been thinned down to nanometer range (<10 nm) to be more mechanically compliant and transparent; conducting polymers like polystyrene sulfonate-doped poly(3,4-ethylene dioxythiophene) (PEDOT:PSS) and graphite-PDMS composite; and carbon-based materials (carbon nanotubes, graphene) [1, 18, 19].

Graphene has shown a lot of potential for use in optoelectronic devices, due to its unique combination of properties such as high electrical conductivity, flexibility, mechanical stability, and high optical transparency. Graphene has been investigated as a neural electrode material. Graphene electrodes have been shown to be able to record electrical activity, however, the impedance does not reach that of conventional recording electrode materials (e.g. gold). Furthermore, the stimulation capability of graphene electrodes in the literature is not sufficient to elicit a neural response.

Due to these reasons, various techniques have been investigated to improve the electrical characteristics of graphene. These include stacking multiple layers of graphene, chemical doping, and adding nanostructures on the surface. However, these methods have not been fully characterised for neural electrode application.

### 1.3. Thesis objectives and approach

This thesis aims to assess the neural recording and stimulation performance of graphene electrodes and explore how graphene electrodes can be improved for optogenetics applications. To achieve that, several research questions are addressed, such as what are the most relevant electrode performance indicators, furthermore, which methods of graphene functionalization are most suitable for transparent and flexible electrodes, and how do they affect the performance.

In this work, multilayer graphene electrodes are evaluated with electrochemical characterisation techniques, and the effect of various graphene improvement techniques on the performance of graphene electrodes for optogenetics application are quantified. This will be achieved with several steps, including:

1. Fabrication and characterisation of graphene electrodes
2. Modification of the graphene electrodes with three improvement methods:
  - (a) Adding thickness to the graphene layer
  - (b) Depositing gold and platinum nanoparticles on the electrode surface
  - (c) Chemical doping of graphene with nitric acid
3. Investigation of how the improvement methods affect the performance of graphene electrodes
4. Evaluation of how the improvement methods affect transmittance

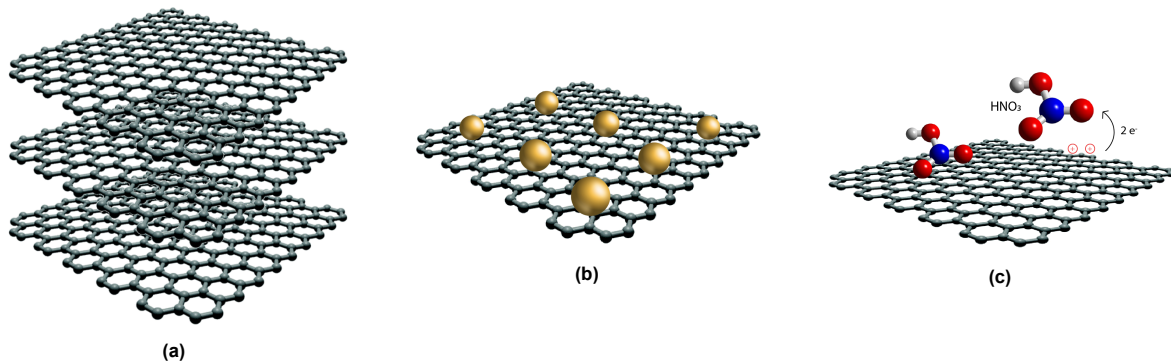


**Figure 1.5:** Illustrations of the improvement methods used in this work: (a) adding thickness, (b) depositing nanoparticles on the surface, (c) nitric acid doping

### 1.4. Outline of the report

In order to compare electrode materials, electrochemical characterisation is used. The main characterisation techniques and desired results are described in chapter 2. Transparent conductive materials are introduced in chapter 3, with the main focus on graphene. The literature review on graphene neural electrodes is presented. Next, various methods for improving the electrical characteristics of graphene are explored and the effects on electrode performance reported in the literature are shown.

In chapter 4, the fabrication of the graphene electrodes is described and the details for the characterisation techniques are given. Furthermore, the transfer process of graphene to a glass slide is explained. Next, the nanoparticle deposition and nitric acid treatment are described. In chapter 5, the results of the measurements are presented and discussed. Conclusions and recommendations for future work are given in chapter 6.

## Characterisation of neural electrodes

To evaluate the electrode performance and compare different materials as an implantable neural interface for recording and stimulating, several characterisation techniques are used, such as electrochemical impedance spectroscopy, cyclic voltammetry, and potential transients. Sheet resistance measurements are used for thin-film materials characterisation. For transparent electrode materials also the optical transmittance is evaluated. In this chapter, the performance tests and desired results are described.

### 2.1. Electrode-tissue interface

Electrical current from the electrode is transformed into an ionic current at the electrode-tissue interface. The performance of the electrode is highly dependent on that interface. Therefore, for electrode characterisation, simulating that interface is important. Simple saline with  $Na^+$  and  $Cl^-$  ions as charge carriers can replace the extracellular fluid around the electrode for short-term in vitro characterisation [3].

When an electrode is immersed in saline, the ions with dipolar water molecules will form a layer on the electrode surface. This layer and the charged electrode surface act as a double-layer capacitor. Other ions that are not on the surface diffuse away from the electrode [3]. The electrode double-layer capacitance ( $C_{dl}$ ) and the diffuse layer are depicted in figure 2.1.

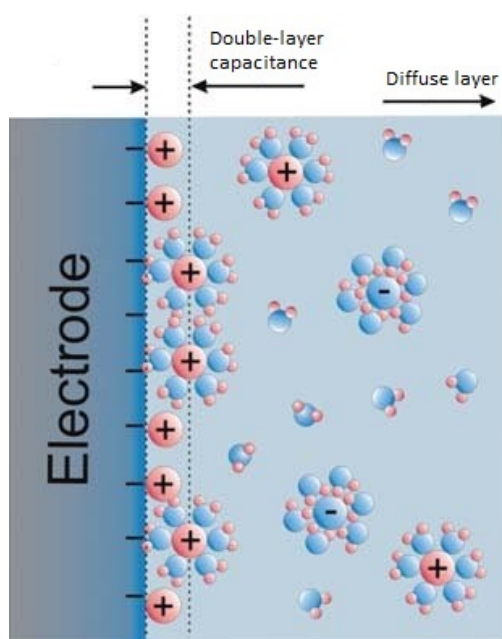


Figure 2.1: Electric double-layer around the electrode inside an electrolyte [20]

During stimulation, charge transfer between an electrode and electrolyte happens through capacitive and faradaic mechanisms. Capacitive charge transfer involves charging and discharging the  $C_{dl}$  and is fully reversible when the direction of the current is reversed. Faradaic transfer involves electrochemical reactions where an electron is transferred across the interface and some species are oxidized or reduced. Faradaic reactions that include only a monolayer on the electrode surface are also named pseudocapacitive [14]. A faradaic reaction can be reversible or irreversible.

An irreversible reaction generates volatile products, which means that all components will not be available during a reversed phase of a stimulation pulse. Thus, the original state of the electrode is not restored. Irreversible reactions should be avoided when stimulating, not to damage the tissue or the electrode. Common irreversible processes include water electrolysis, oxidative formation of soluble metal complexes, and corrosion. Therefore, capacitive charge injection is preferred due to its reversibility [14]. The potential limits where water oxidation and reduction start happening is called the 'water window'. During electrochemical measurements, the potential of the electrode should always be kept inside these limits not to induce irreversible water electrolysis [3].

## 2.2. Electrochemical impedance spectroscopy

Selectivity (spatial resolution) and sensitivity (to slight changes in the potential) are two crucial characteristics of a recording electrode. As the exposed area of the electrode decreases, the spatial resolution improves, but at the same time, the electrochemical impedance is increased due to the limited area for interaction with the extracellular fluid [3].

The electrode impedance should be as low as possible because the SNR during recording has an inverse relationship with electrode impedance. Furthermore, the required voltage to create a stimulation current increases with the electrode impedance. Increasing the voltage could result in electrolysis or corrosion [3].

Longevity and predictability are other important aspects of an electrode [3]. The electrode interface should preserve stable impedance over a long period of time [2] because once implanted, it should not be replaced in years since it requires surgical intervention [3].

The electrochemical characterisation for electrodes is usually done in a 3-electrode setup submerged in saline, as illustrated in figure 2.2. The electrode which performance is being evaluated is called a working electrode (WE). The ground, or current sink, used to close the circuit is called a counter electrode (CE) which needs to have a large surface area so that its contribution to the impedance would be negligible [3]. The third one is a reference electrode (RE), which is used to measure the electric potential variation on the working electrode, therefore the potential of this electrode cannot change over time [21].

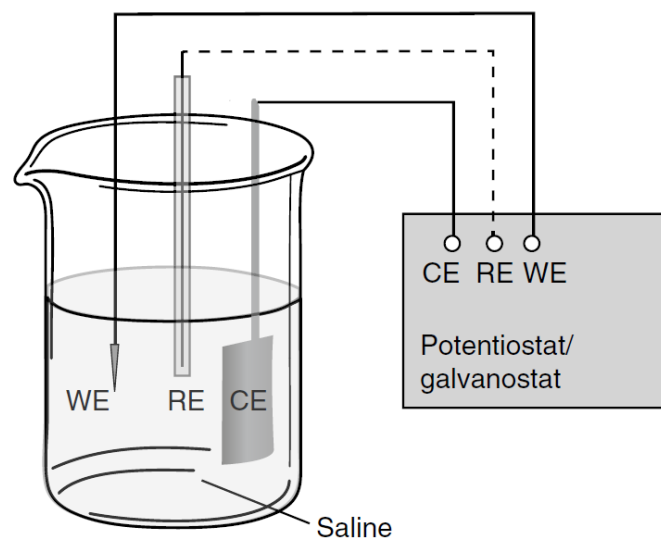
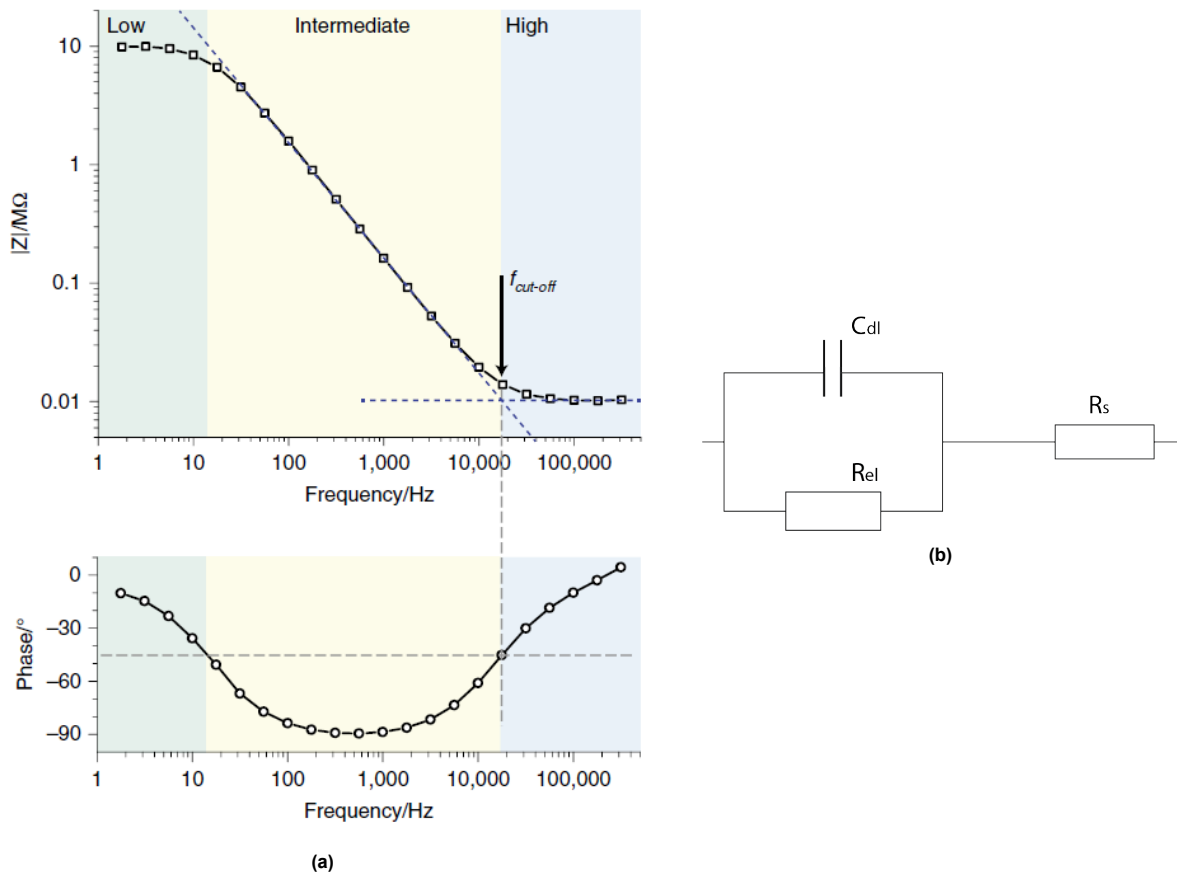


Figure 2.2: 3-electrode setup for EIS and CV measurements [3]

The impedance of a neural electrode is measured with Electrochemical Impedance Spectroscopy (EIS). This method is widely used as a characterisation tool for recording electrodes. During EIS, a sinusoidal voltage waveform with different frequencies is applied on the working electrode and the current response is measured with a counter electrode. The frequency ranges typically from 1Hz to 100kHz. The root-mean-square (RMS) of the voltage is generally between 10mV and 50mV, not to induce irreversible reactions on the electrode [3, 14]. The electrochemical impedance  $Z$  is found by comparing the amplitude and phase of the input signal with the recorded signal. The measured impedance is usually displayed with a Bode plot, where the magnitude of  $Z$  and the phase shift of  $Z$  are plotted separately. An example Bode plot can be seen in figure 2.5a [3].

The equivalent circuit model for the electrode-electrolyte interface usually consists of the electrolyte resistance ( $R_s$ ) and the charge transfer mechanisms that act in parallel: capacitive ( $C_{dl}$ ) and faradaic ( $R_{el}$ ) (figure 2.3b). At low frequencies, almost no charge crosses the capacitive double layer, thus, other surface reactions ( $R_{el}$ ) and the electrolyte resistance ( $R_s$ ) contribute to the impedance magnitude. In the intermediate frequency range, the interface contribution affects the timing and shape of the signal. More charge flows over the capacitor, thus, a reduction in the impedance magnitude and a  $90^\circ$  phase shift are expected [3]. The impedance at 1kHz is usually reported for recording electrodes for comparison [14]. At the high-frequency range, due to the effortless charge transfer over the interface, the impedance of the interface is negligible, and the resistive behaviour of the electrolyte ( $R_s$ ) contributes to the high-frequency impedance [14]. Therefore, in the high-frequency range, the signal transfer is frequency-independent and the phase is not shifted [3].



**Figure 2.3:** (a) Typical Bode plot for an electrode [3]. (b) Equivalent circuit model of electrode-electrolyte interface.

For flexible implants, electrochemical measurements should also be done under mechanical strain since the electrical characteristics of flexible materials are sensitive to stretching. The implant can be clamped to a platform that applies various displacements while the measurements are done. Therefore, strain-dependent electrical properties are obtained [22].

## 2.3. Cyclic Voltammetry

Cyclic Voltammetry (CV) is performed in the same 3-electrode setup as EIS, where the working electrode's potential is driven at a constant sweep rate with respect to a reference electrode between two limits that are within the water window, as shown in figure 2.4 inset. The current, which is measured through a counter electrode, gives information about the electrochemical reactions at the electrode surface [14]. Steady positive and negative currents are expected for an electrode only exhibiting double-layer capacitance. When the activation potential of a reaction is reached, the current will increase rapidly. This can be identified as a peak on the CV graph. When a current peak is present only during the forward scan and absent during reverse, it is the result of an irreversible reaction (figure 2.4) [3, 23].

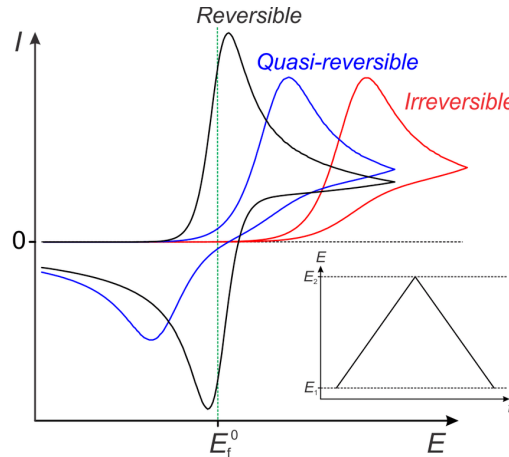


**Figure 2.4:** Different shapes of CV plot according to the charge transfer mechanism. The inset illustrates the applied voltage on the working electrode [23]

For a stimulation electrode, the (cathodic) charge storage capacity (CSC) is an important characteristic. It is calculated from the time integral of the (cathodic) current during the CV. CSC represents the amount of charge that can be stored reversibly in an electrode. It is dependent on the electrode material, size, and shape, as well as the composition of electrolyte and stimulus waveform [14].

CV measurements are highly affected by the sweep rate. With an increased sweep rate, the time of the measurement is decreased. To transfer the same charge over the interface, the current has to be higher. However, when CV voltage data is converted to time, it can be seen that the area under the curve for slow sweep rate is higher (figure 2.5). Under a high sweep rate, pore resistance limits access to all the available charge [14]. Furthermore, the reaction rates at the surface depend on the concentration of the solution close to the electrode. With fast scan rates, the concentration of the reactant is smaller due to slower flux [24]. Therefore, CSC is larger measured at low sweep rates. For comparison, CSC results must be accompanied by the measurement conditions [22].

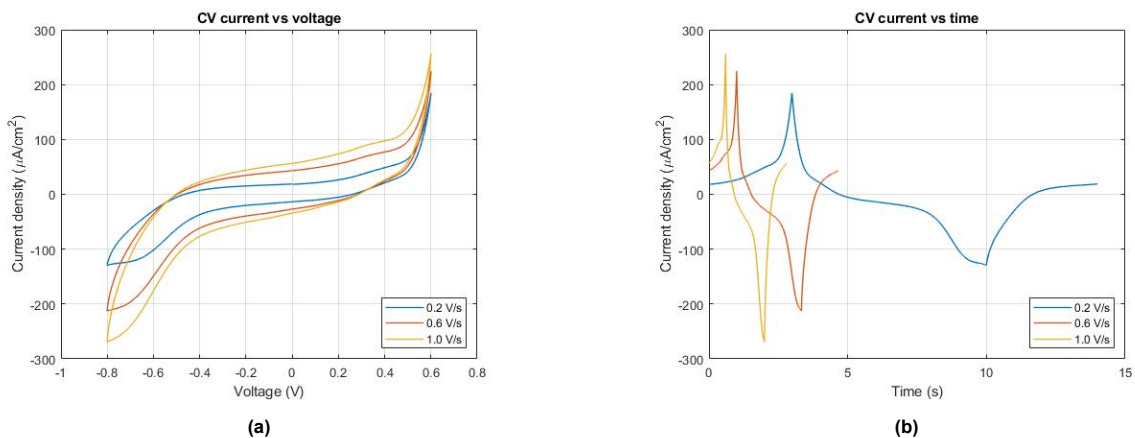


**Figure 2.5:** CV measurement data expressed on (a) current vs voltage and (b) current vs time plots

## 2.4. Voltage Transients

Voltage Transients (VT) are recorded in the same 3-electrode setup. Current-controlled stimulation pulses are injected through the working electrode and returned through the counter electrode. The voltage is measured between the working and reference electrode [22]. Typically biphasic, charge-balanced current pulses are used (figure 2.6, top) [14]. The measured voltage (figure 2.6, bottom) shows a fast voltage drop ( $V_A$ ) at the beginning of the phase, which is the ohmic voltage drop due to electrolyte resistance, followed by a gradual voltage reduction ( $V_{\mu E-C}$  - cathodic,  $V_{\mu E-A}$  - anodic) over the interface of the working electrode.

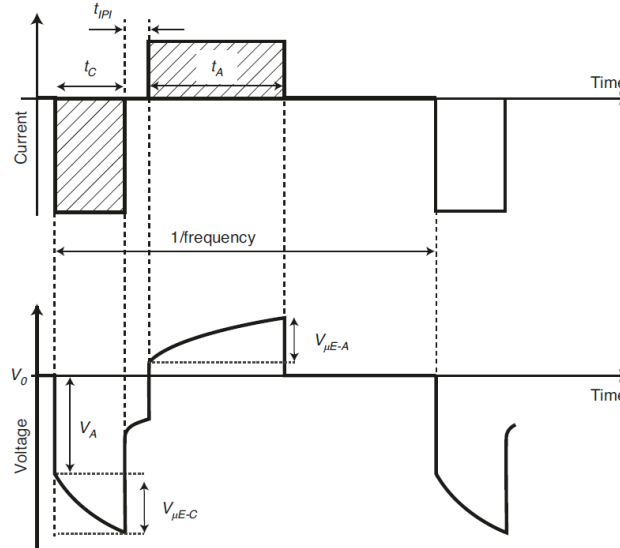


**Figure 2.6:** Voltage transient measurement. The top graph indicates the stimulation current pulses and the bottom graph illustrates the voltage response on the electrode [3]

During fast biphasic pulses at intermediate voltages, charge transfer is mainly capacitive. However, when the voltage is increased, the rate of faradaic reactions is also increased. 'Maximally safe charge injection capacity' ( $CIC_{max}$ ) defines the maximum amount of charge that can be injected without the occurrence of water electrolysis [3]. During the VT measurements, the current of the stimulus pulse is gradually increased until the  $V_{\mu E-C}$  and  $V_{\mu E-A}$  are just inside the water window. The current at that point determines the  $CIC_{max}$  [3, 14]. The  $CIC_{max}$  has been shown to be higher with a larger pulse width. That is possibly due to non-uniform distribution of the current over the electrode area. During short pulses, the central area of the electrode is not used [25].

In order to elicit a neural response, CIC in the order of hundreds of  $\mu C/cm^2$  with pulse widths between 100  $\mu s$  and 1ms is needed [4]. Changes in electrode characteristics after thousands of stimulation pulses can give an indication of electrode stability [26].

## 2.5. Sheet resistance measurement

Sheet resistance is a key property for materials that are used as thin films, such as used in electrodes. Since the ability to transfer signal depends on the conductivity of a material, lower sheet resistance materials are desired for neural electrodes.

Sheet resistance can be measured with a two-point or a four-point technique. In a two-point measurement, voltage (V) is applied on two ends of a thin rectangular structure and the current (I) is measured. The resistance R is then:

$$R = \frac{V l}{I A} \quad (1)$$

Where A is the cross-sectional area and l the length of the rectangle, respectively.

The four-point measurement technique uses four probes connected to the material with equal spacing. This technique is independent of the size of the sample measured and the contact resistance is eliminated from the measurement. However, the sample should be flat and homogeneous and the measurement probes should be far away from the measured area. The advantage of this technique is that contact resistance is not included.

Van der Pauw structures, as depicted in figure 2.7, are generally used. Current is set to flow between A and B contacts ( $I_{AB}$ ) and voltage is measured between C and D ( $V_{CD}$ ). The sheet resistance can then be calculated by:

$$R_s = \frac{V_{CD}}{I_{AB}} * \frac{\pi}{\ln 2} \quad (2)$$

Sheet resistance is expressed in  $\Omega/sq$  (ohms per square) to differentiate it from bulk resistance [27].

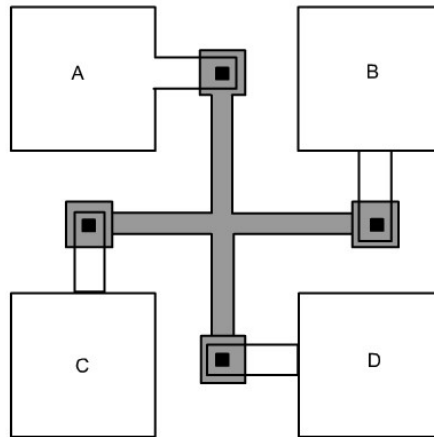


Figure 2.7: Van der Pauw structure for 4-point probe measurement

## 2.6. Optical transmittance

Optical transmittance measurements show how much light is absorbed by the material. Light with various wavelengths is passed through the sample. The light intensity is measured before ( $I$ ) and after ( $I_0$ ) passing the sample and the transmittance (%T) is expressed as the ratio  $I/I_0$  [28].

Transmittance values from ultraviolet (UV) to infrared (IR) range (350 to 900nm) are important for optoelectronic device materials. For calcium imaging, 50% transmittance is sufficient [29], however, for optogenetics applications, the transmittance should be higher than 90% to reduce light-induced artefacts during recording [17].

Example result of optical transmittance measurement is shown in figure 2.8.

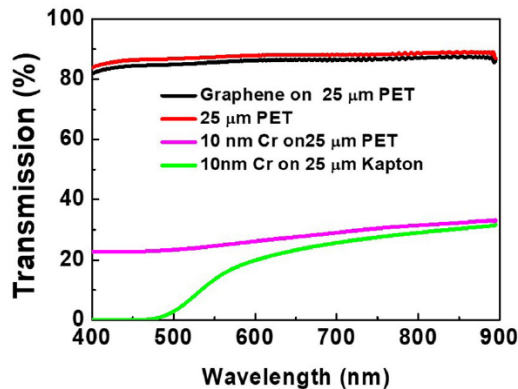


Figure 2.8: Optical transmittance measurement of graphene and chromium on PET substrate

# 3

## Literature study

### 3.1. Transparent electrode materials

For optoelectronic devices, materials with high conductivity and broad-wavelength transparency are needed. Indium tin oxide (ITO) is widely used due to relatively high transmittance ( $\sim 80\%$ ) and very good electrical conductivity, but the material is intrinsically brittle and therefore not suitable for flexible implants. Metal nanomesh (15nm) [12] and ultrathin metals ( $<10$  nm) [18] have been used to replace ITO, which have better flexibility. They have been shown to endure thousands of bending cycles without deteriorating sheet resistance, but poor adhesion to the substrates makes the morphology rough and discontinuous, therefore the transmittance suffers (broad-wavelength transmittance  $\sim 60\%$ ) [18, 13].

Conducting polymers are an emerging material for optoelectronic applications. PEDOT:PSS, being the most outstanding, has remarkable flexibility and transmittance, but the conductivity does not reach that of ITO. Furthermore, PEDOT has shown to degrade over time in aqueous solutions, which is not suitable for long-term implants [4].

Carbon-based materials are considered as transparent conductive materials, such as graphene, graphene oxide, and carbon nanotubes (CNT). While CNTs have very high electron mobility and conductivity, the random placement of the nanotubes on a large foil reduces the optical properties, and therefore, is not preferred for optoelectronic devices. Graphene oxide has inferior transmittance and conductivity to graphene. Therefore, graphene could be the preferred conductive material for flexible and transparent devices [18].

### 3.2. Graphene

For optoelectronic applications, graphene has recently drawn a lot of attention. Graphene is one atom thick layer of pure carbon atoms in a honeycomb lattice (figure 3.1a). It is an interesting material for many applications due to the combination of properties such as optical transparency, flexibility, mechanical stability, high electrical conductivity, and biocompatibility [16, 30].

Graphene is a 2-dimensional (2D) material with long mean free paths for electrons, thus exhibits a very high charge carrier mobility at room temperature [31]. The great properties of graphene are related to the spatial arrangement of the carbon atoms. The material is composed of  $sp^2$  hybridized carbon atoms in a hexagonal lattice [32]. The symmetric distribution of valence band and conduction band on two sides of the Fermi level is unique among 2D semiconductor materials. Furthermore, the bands intersect at their extremities, forming Dirac cones (figure 3.1b), which makes graphene a zero band-gap semiconductor. Due to this linear dispersion, the free electrons in graphene act as massless particles, which is why graphene has high electron mobility [33].

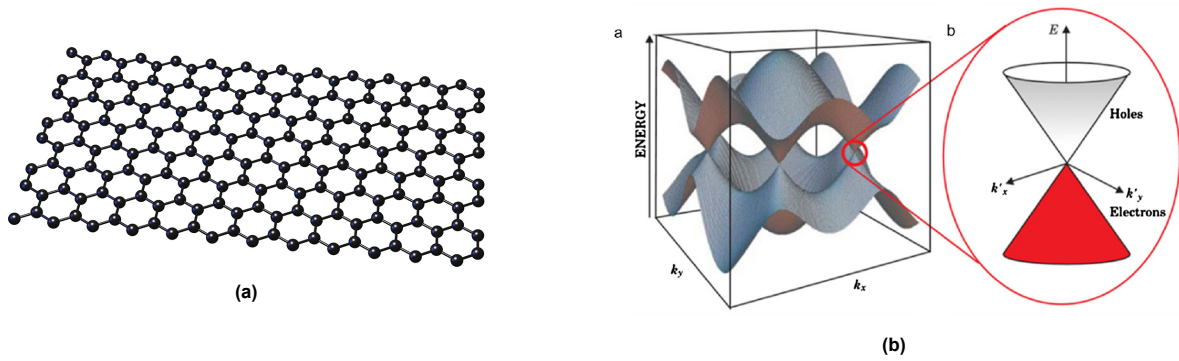


**Figure 3.1:** (a) Illustration of the hexagonal graphene lattice. (b) Electronic band structure of graphene and the formation of Dirac cones [33].

Graphene has a very high transmittance ( $>90\%$ ) from UV to IR frequency range [13]. Monolayer graphene absorbs  $\sim 2.3 \pm 0.1\%$  of the visible light [33]. It is possible to calculate the exact number of graphene layers in multilayer graphene from the optical transmittance measurement. By dividing the total absorbance of the multilayer with the monolayer absorbance, the number of layers can be determined.

There are various methods to fabricate graphene. The first method to create a single layer of graphene from graphite was discovered in 2004. It was the scotch tape method (exfoliation) developed by Novoselov and Geim [32]. Later on, epitaxial growth, chemical oxidation-reduction of graphite, and chemical vapour deposition (CVD) were developed [34]. CVD is the most commonly used method since it is relatively inexpensive and scalable. CVD enables growing graphene on metal foils and thin-films, e.g. Cu, Ni, Mo, and many others [30]. With this technology, large-area graphene sheets can be fabricated [1].

The process of CVD, illustrated in figure 3.2, includes a gas species with carbon atoms (i.e.  $CH_4$ ) passing through a hot chamber where the metal catalyst is previously annealed. In the chamber, hydrocarbon is decomposed to carbon radicals which then dissolve on the metal surface, resulting in supersaturation. The process is usually done at high temperatures (800 to 1200 °C) [35, 36]. A higher temperature has been shown to grow graphene with lower defect density [30]. There are two possible methods for graphene growth: isothermal and precipitation. The isothermal growth process refers to supersaturation being achieved via continuous exposure to hydrocarbon at a constant temperature. The parameters that affect the thickness of graphene are the precursor pressure, catalyst thickness and exposure time. Furthermore, carbon solubility and diffusibility of the catalyst affects the growth [37]. During cooling, additional growth may occur when the carbon atoms precipitate or segregate to the surface of the catalyst to form graphene films [36].

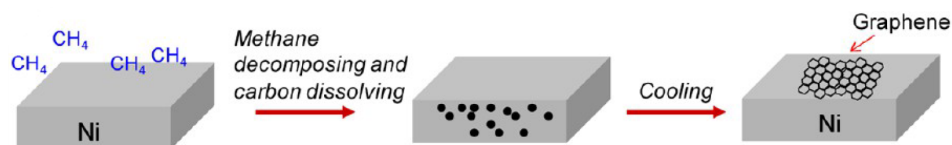


**Figure 3.2:** Illustration of CVD of graphene in Ni [35]

After graphene growth, it should be separated from the metal foil and transferred onto the desired substrate based on the application. For that, polymethyl methacrylate (PMMA) is typically used. PMMA is coated on top of graphene, after which the metal is etched. Next, the PMMA/graphene film will be transferred to the target substrate and then PMMA is removed with acetone [35].

However, the transfer process can leave polymer residues and induce wrinkles or defects into the graphene layer. A transfer-free graphene fabrication process has been reported by Vollebregt et al. [38]. Molybdenum (Mo) was deposited on a wafer with  $SiO_2$  and CVD graphene was grown on the catalyst, after which Mo was etched with phosphoric acid and the graphene layer attached to the substrate with  $SiO_2$ . Another advantage of this method is that Mo can be patterned before graphene growth, resulting in location-specific growth of graphene [38].

### 3.2.1. Raman Spectroscopy

To evaluate the quality of the graphene layer, Raman spectroscopy is used. The method is based on the interaction of light with the chemical bonds within a material. A small amount of light from a laser source is scattered at different wavelengths, which depend on the chemical structure of the analyte [39].

Raman spectroscopy gives information about the presence of graphene, the number of layers, and the number of defects in the layer. Generally, a laser with 514nm or 633nm wavelength is used. Three distinct peaks can be observed: D peak around  $1330\text{ cm}^{-1}$  (with 633nm), G peak around  $1580\text{ cm}^{-1}$ , and 2D peak around  $2700\text{ cm}^{-1}$  (figure 3.3). The ratio between the intensities of D and G peak ( $I_D/I_G$ ) indicates the defects in the graphene layer. The higher the  $I_D/I_G$ , the greater the number of defects. The G peak is related to the  $sp^2$  carbon bonds and the 2D peak is related to the number of layers present. The ratio between the intensities of 2D and G peak ( $I_{2D}/I_G$ ) is typically larger than 1 for monolayer graphene and smaller than 1 for multilayer graphene [33, 13, 30].

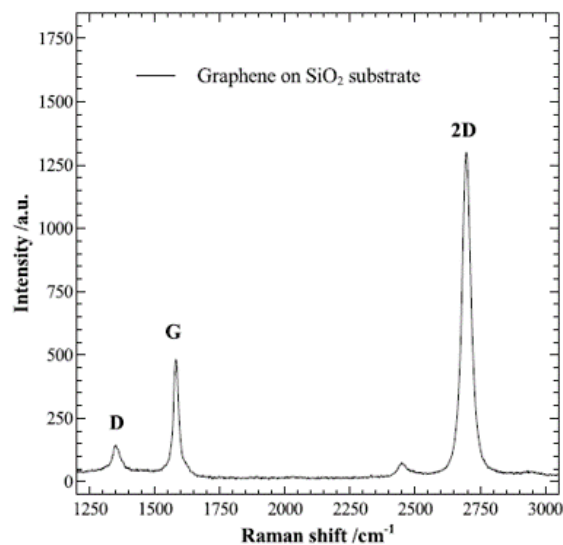


Figure 3.3: Raman spectroscopy of graphene on silicon oxide with identifiable D, G, and 2D peaks [40]

### 3.2.2. Graphene neural electrodes

Monolayer, as well as multilayer graphene, has been used to fabricate neural electrodes. In this section, the characteristics of the electrodes made from both graphene from the literature will be discussed.

Reported CICs of microscale graphene electrodes are generally around tens of  $\mu\text{C}/\text{cm}^2$ , which is lower than that of conventional materials like gold ( $50\text{-}350\ \mu\text{C}/\text{cm}^2$ ) and platinum ( $4\text{-}10\ \text{mC}/\text{cm}^2$ ) [41, 42]. Novel materials, like iridium oxide (IrOx) and PEDOT-CNT composition, have CIC in the  $\text{mC}/\text{cm}^2$  range, which is substantially higher than graphene [4].

Since gold is commonly used for recording electrodes, due to the low impedance, monolayer graphene electrodes were compared with 50 nm thick gold electrodes by Koerbitzer et al. [40]. Graphene was transferred on a  $\text{SiO}_2$  substrate with a polymer-free process. The impedance at 1kHz was 30% lower for the gold electrode with equal size ( $0.31\ \text{mm}^2$ ). In another work by Koerbitzer et al [43], electrodes with the size of  $700\ \mu\text{m}^2$  of gold, graphene, and gold with graphene layer coating were fabricated. The impedance at 1kHz was reported  $1.08 \pm 0.46\ \text{M}\Omega$  for gold and  $2.65 \pm 0.46\ \text{M}\Omega$  for graphene electrode while gold-graphene showed the lowest impedance of  $860 \pm 70\ \text{k}\Omega$ . Furthermore, the electrodes were used for cell culturing for 4-6 weeks, after which the impedance for plain gold electrode was increased an unexpected 34% while gold-graphene showed only 2% increase and bare graphene electrode did not show any increase. Therefore, graphene exhibits stability and reliability in a biochemical environment. SNR for graphene electrode was reported 35.8 and 66.6 for the gold-graphene electrode [43].

The reported CICs were very different for the different electrode sizes. For  $0.31\ \text{mm}^2$ , the CIC was shown to be greater for graphene electrode  $0.8\ \text{mC}/\text{cm}^2$  compared to gold  $0.03\ \text{mC}/\text{cm}^2$  [40]. For  $700\ \mu\text{m}^2$  size electrode The CIC was reported  $0.15\ \text{mC}/\text{cm}^2$  for graphene and  $0.16\ \text{mC}/\text{cm}^2$  for gold. In both cases, it does not reach the level of conventional materials such as TiN ( $0.87\ \text{mC}/\text{cm}^2$ ) or IrOx

( $4 \text{ mC/cm}^2$ ) that are used for stimulation electrodes. The CSC measured with  $1 \text{ V/s}$  scan rate was reported  $910 \text{ } \mu\text{C/cm}^2$  for graphene and  $730 \text{ } \mu\text{C/cm}^2$  for gold electrode [43]. CSCs reported for  $0.049 \text{ mm}^2$  platinum electrodes are  $4.1 \pm 0.4 \text{ mC/cm}^2$  smooth surface electrode and  $10.4 \pm 1.2 \text{ mC/cm}^2$  for roughened surface electrode at  $250 \text{ mV/s}$  [42]. Whereas, CSC reported for TiN is  $4.82 \text{ mC/cm}^2$  and IrOx  $21 \text{ mC/cm}^2$  at  $100 \text{ mV/s}$ . [44].

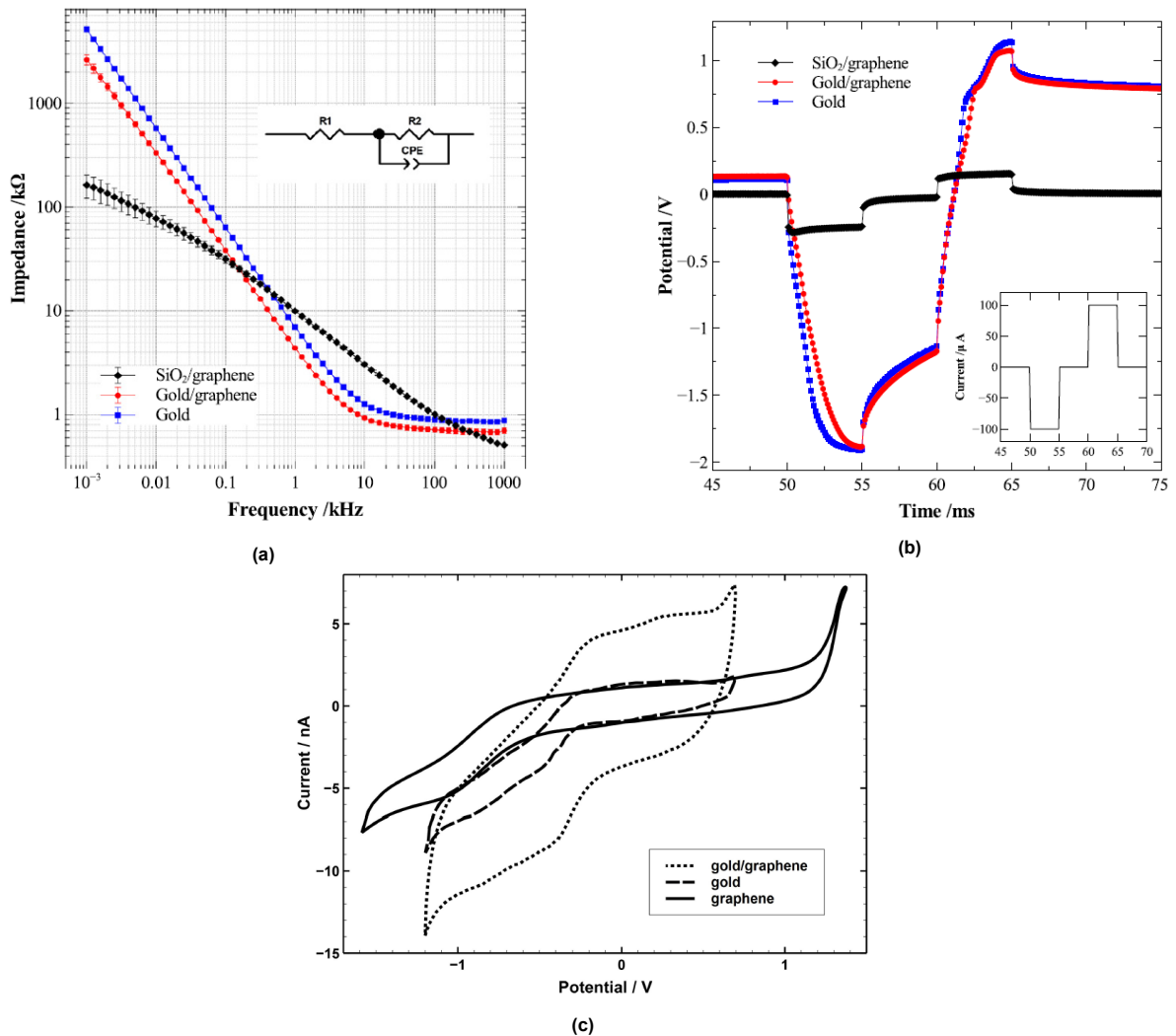


**Figure 3.4:** Impedance (a), voltage transients (b), and cyclic voltammetry (c) measurements on graphene, gold, and gold with graphene coating [40, 43]

Biocompatibility is one of the most important properties of neural electrode materials. Graphene's biocompatibility has been studied with cell cultures. These studies show that human neural stem cells cultured on graphene have a higher survival rate, enhanced adhesion, and improved differentiation than on glass. However, cell culture studies have shown the biostability of graphene up to one month, thus longer studies in vivo are necessary to confirm the biocompatibility of graphene [16, 4, 40].

Electrodes were fabricated with monolayer CVD graphene stacked into four layers with the PMMA transfer method described in section 3.2, by Park et al. [17]. These were used for electrophysiology recording with optogenetic stimulation and calcium imaging. Calcium imaging performed during electrical stimulation showed minimal to no artefact with graphene electrodes, while platinum electrodes obstructed the imaging (figure 1.4). The optogenetics experiments on mice showed light-induced artefacts in the measurements for both graphene and platinum electrodes. This can be due to increased absorption by the multiple layers of graphene [17].

Another study, using a different method for transferring graphene monolayer, showed artefact-free recording during optogenetic stimulation and integration with 2-photon imaging. Here, PMMA was

spin-coated on graphene/copper bilayer, which was then connected to a cathode of a DC power supply and anode submerged in NaOH in deionized water, which created hydrogen gas bubbles between the graphene and copper layer and separated the graphene. That method avoided crack formation and provided a high yield [45].

A summary of the properties of graphene neural electrodes found in the literature is given in tables 3.1 and 3.2. In these papers, the CV and VT measurements were done with different parameters. As mentioned previously, a lower sweep rate for CV increases the CSC. Furthermore, different water windows were used in these studies because the exact water window for graphene is unknown. Therefore, a study of the safe window for charge injection for graphene would be very useful.

**Table 3.1:** Impedance at 1kHz of graphene vs metal electrodes with the same size

Graphene	size ( $\mu m^2$ )	Z at 1kHz	metal	Z at 1kHz	reference
stacked multilayer	314	$170 \pm 11.1 \text{ k}\Omega$	gold	$186 \pm 3.4 \text{ k}\Omega$	[46]
monolayer	700	$2.65 \pm 0.46 \text{ M}\Omega$	gold	$1.08 \pm 0.46 \text{ M}\Omega$	[43]
monolayer	7 800	$1 \text{ M}\Omega$	gold	$300 \text{ k}\Omega$	[47]
stacked 4 layers	7 854	$286.4 \pm 92.6 \text{ k}\Omega$			[17]
monolayer	10 000	$1 \text{ M}\Omega$	gold	$300 \text{ k}\Omega$	[29]
monolayer	10 000	$963 \text{ k}\Omega$			[45]
stacked 4 layers	17 671	$248.7 \pm 125.0 \text{ k}\Omega$			[17]
stacked 4 layers	17 671	$243.5 \pm 5.9 \text{ k}\Omega$	platinum	$188.8 \pm 92.9 \text{ k}\Omega$	[48]
stacked 4 layers	31 416	$215.7 \pm 120.4 \text{ k}\Omega$			[17]
monolayer	310 000	$10.0 \pm 0.2 \text{ k}\Omega$	gold	$7.0 \pm 0.06 \text{ k}\Omega$	[40]

**Table 3.2:** CSC and CIC of graphene electrodes

Graphene	size ( $\mu m^2$ )	CSC ( $\mu C/cm^2$ )	sweep rate	water window	CIC ( $\mu C/cm^2$ )	pulse width	amplitude	reference
monolayer	700	910 (total)	1 V/s	-1.4 V to 1.2 V	150	1 ms	0.1-5 $\mu A$	[43]
4 layers	17 671	87.8 (cathodic)	1 V/s	-0.6 V to 0.8 V	57.13	0.5 ms	10-80 $\mu A$	[17]
monolayer	310 000			-0.6 V	800	5 ms	1-500 $\mu A$	[40]

Graphene electrodes used for neural recording have shown sufficient SNR, however, the impedance of monolayer graphene electrodes does not reach the level of the traditionally used gold electrode. The CSC and CIC vary greatly between the electrodes, but it appears that they remain lower than for currently used materials like Tin and IrOx. Optogenetics integration has shown to produce light-induced artefacts in some cases, but calcium imaging is not affected with the graphene electrode. Short-term cell culture studies have shown the biostability of graphene, but further investigation is required. Based on the literature, graphene has potential for neural recording application, however, CSC and CIC should be improved for stimulation.

### 3.3. Methods for improving electrical characteristics of graphene electrodes

Previously developed graphene electrodes have shown to be able to record with high SNR but the impedance compared to conventional materials is still high. Since SNR during recording is reciprocal to the electrode impedance, a lower impedance is desired. In addition to recording, electrodes are also used for stimulation. The CSC and CIC for small-size graphene electrodes are too low to inject a sufficient amount of charge for activation of neural structures.

Various methods to improve the electrical characteristics of neural electrodes have been developed. Techniques that can be integrated with graphene without losing the advantageous properties are adding layers of graphene, chemical doping, and surface modification with nanostructures. These methods have been shown to increase the conductivity of graphene without losing flexibility or transparency. The effects of these methods on the impedance, CSC, CIC, and transmittance of graphene neural electrodes reported in the literature are described in the following section and summarised in table 3.3.

#### 3.3.1. Stacking graphene layers

Stacking multiple graphene layers provides additional transport paths for the charge carriers, which increases the conductivity of graphene. Several layers of graphene were stacked to see the effect on sheet resistance by Lee et al. [49] and Kasry et al. [50]. A trade-off between conductivity and optical transmittance has been reported [13, 49, 50]. With each added graphene layer the transmittance is reduced and conductivity improved. A lower number of graphene layers is more cost and time effective but more layers enhances mechanical and electrical reliability [13]. Optical transmittance is reduced due to the added graphene layers but also due to the polymer residues on each layer from the transfer process. Lee et al. [49] reported the differences of stacking monolayers and bilayers. Using bilayers reduces the number of transfers, and thus, the polymer residues, and results in higher transmittance. Furthermore, since the transfer process can induce defects to the graphene lattice, fewer transfers show lower sheet resistance (figure 3.5) [49].

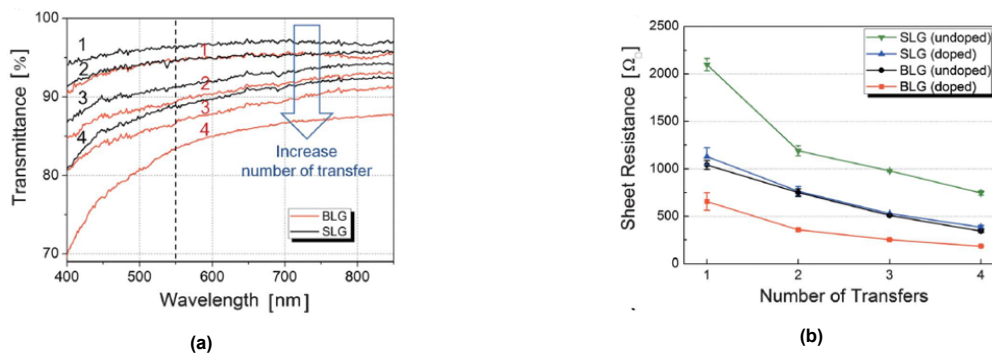


**Figure 3.5:** (a) Transmittance of stacked graphene monolayers (SLG) and bilayers (BLG). (b) Sheet resistance of stacked undoped and nitric acid doped monolayers (SLG) and bilayers (BLG) [49].

#### 3.3.2. Chemical doping

Chemical doping of graphene can be achieved with acids ( $H_2SO_4$ ,  $HCl$ ,  $HNO_3$ , etc.) or metal chlorides (Au, Ir, Os, Pd, etc.). Among those, nitric acid ( $HNO_3$ ) doping has been widely used [51].

Pristine graphene exhibits high charge carrier mobility but very low intrinsic carrier density. Nitric acid ( $HNO_3$ ) has been used to dope graphene to increase the number of charge carriers. Nitric acid doping is an adsorptive type, which is far less invasive than substitutional doping. Thus, it does not alter the graphene lattice or perturb the unique properties of graphene [52].

D'Arsie et al. [52] have hypothesised the mechanism behind nitric acid doping of graphene. The  $HNO_3$  molecules are physisorbed onto the graphene, thus the C-C bonds are not broken. The molecule then dissociates into two radicals  $NO_2^0$  and  $NO_3^0$ , and water, which are all physisorbed. These radicals have a singly occupied state below the Fermi energy of graphene. Two electrons from graphene transfer into these states, forming holes in the graphene and giving it p-type doping [52].

They reported that sheet resistance of graphene was lowered more with higher concentration and temperature of nitric acid, whereas exposure time did not have an effect. 65% Nitric acid treatment

resulted in a 90% reduction in sheet resistance. Thermal stability was addressed with post-annealing up to 300°C, which showed that higher acid concentration and temperature samples were more stable. Raman spectra show  $I_D/I_G$  ratio around 0.03, which proves the non-destructive nature of nitric acid doping. Furthermore, nitric acid doped graphene showed high optical transmittance of 97.4% [52].

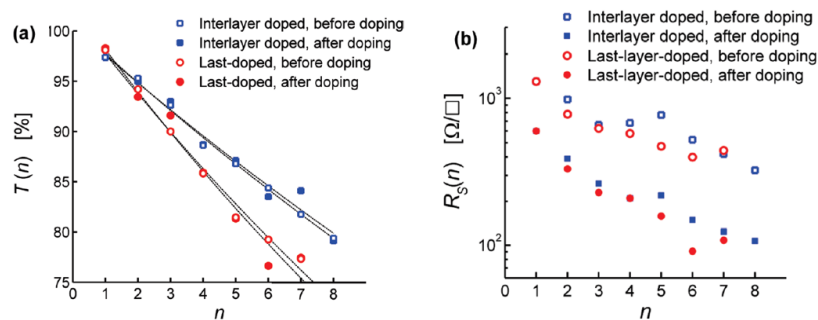


**Figure 3.6:** (a) Optical transmittance dependence on the number of layers and nitric acid doping. Sheet resistance dependence on the number of layers and nitric acid doping [50].

Lee et al. [49] and Kasry et al. [50] have reported sheet resistance values for different numbers of stacked doped layers of graphene. Doping was shown to reduce sheet resistance by a factor of 3, resulting in  $90 \Omega/sq$  with a transmittance of 80% for 8-layer graphene. Two different doping methods were used: either each layer was doped separately and then stacked, or layers were stacked first and then doped in the end. Sheet resistance was comparable in both cases, but transmittance was higher for the inter-layer doping method (figure 3.6). This is probably because the polymer residues between the layers are cleaned [50]. These results indicate that nitric acid doping should also work for CVD multilayer graphene.

Lee et al. [49] also characterised changes in sheet resistance with strain and compared to other materials. At the 2.14% strain, while graphene sheet resistance increased 10-15%, ITO showed an enormous 321% increase, proving the superior flexibility of graphene over ITO.

Nitric acid doping was used to enhance the conductivity of nanopatterned graphene by Choi et al. [53]. Via nanopatterning, areas of graphene were removed, and thus, the conductivity was lowered by a factor of 15. At the same time, transmittance enhanced from 85% to 98%. With nitric acid doping, the sheet resistance was lowered to the level of non-patterned graphene while maintaining the high transmittance [53].

### 3.3.2.1. Nitric acid doped graphene electrodes

A closed-loop optogenetics system was developed by Liu et al. [47]. Monolayer graphene was doped with 35% and 70% nitric acid for 30 seconds. Impedance measured at 1kHz was lower for higher concentration  $HNO_3$  (figure 3.7). Simultaneous optogenetic stimulation and electrical recording were achieved without light-induced artefacts with graphene electrode, whereas gold electrode exhibited prominent artefacts [47].

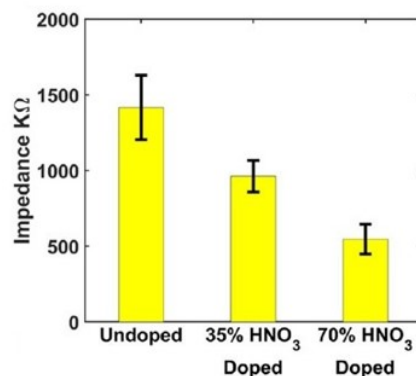


**Figure 3.7:** Impedance at 1kHz for graphene doped with different concentrations of nitric acid [47].

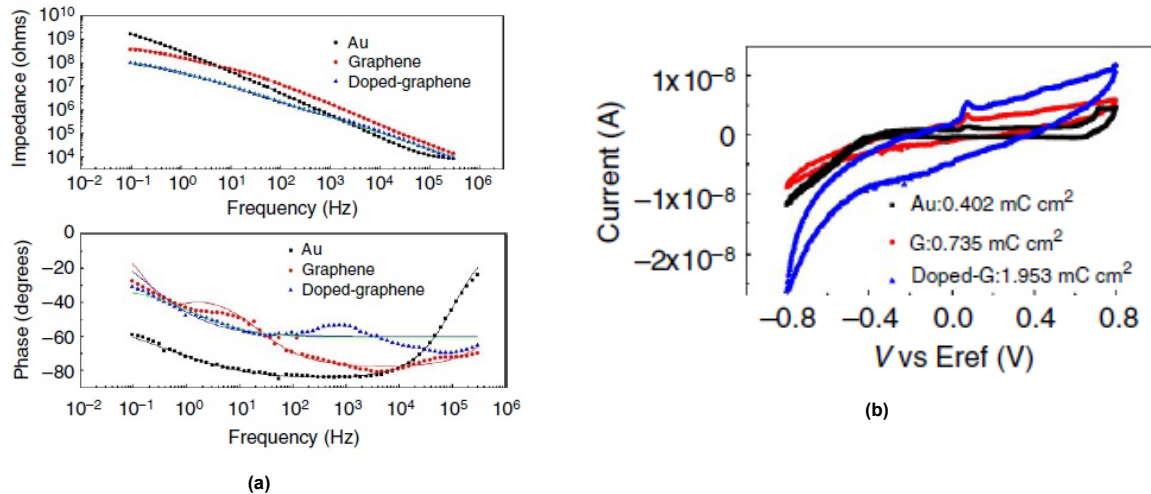


**Figure 3.8:** Cyclic voltammetry (a) and impedance (b) measurements on gold, graphene, and nitric acid doped graphene [54].

Nitric acid doped monolayer graphene electrodes were fabricated by Kuzum et al. [54]. 70% nitric acid was used for doping. Impedance measurements (figure 3.8a) of  $2500 \mu\text{m}^2$  electrodes show that with doping, the impedance of graphene was closer to that of the gold electrode. Furthermore, CV measurements show increased CSC for doped graphene (figure 3.8b). In vivo neural recording was performed on rat models, which showed SNR 40.8 [54]. That is higher than previously reported 35.8 [43]. Calcium imaging showed that neurons under the graphene electrode are clearly visible without any light-induced artefact (figure 3.9), which shows the compatibility of nitric acid doping with optical modalities [54].

A platform with graphene electrodes for electrical and optical monitoring of human stem cell-derived cardiomyocytes was developed by Rastogi et al. [55]. The monolayer graphene was doped with 69%  $\text{HNO}_3$  for 2 hours. Cell viability was not affected by the graphene with nitric acid doping [55].

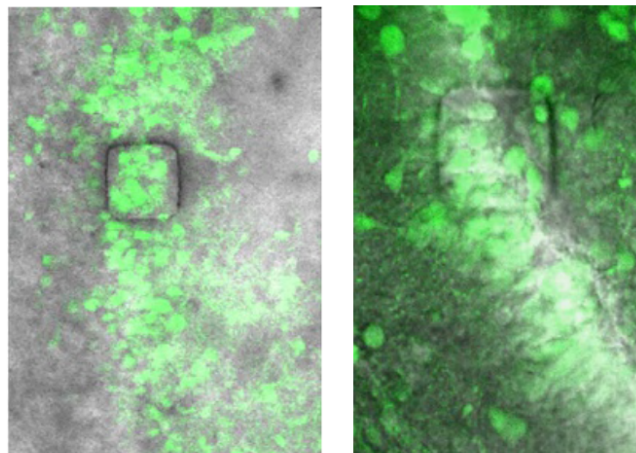


**Figure 3.9:** Calcium imaging with confocal and two-photon microscopy. Nitric acid doped graphene electrode can be seen as a square with darker edges. The cells under the electrode are clearly visible [54]

### 3.3.3. Surface modification

Electrodes with a larger size have lower electrical impedance, but smaller electrodes have a better spatial resolution. This trade-off can be solved by maximizing electrochemical surface area while maintaining the small geometrical surface area of the electrode [2]. Increasing the electrochemical surface area also increases the capacitive double-layer at the electrode-tissue interface and thus the magnitude

of capacitive charge transfer [14]. Therefore, the CSC and CIC are also improved, which are important for stimulation electrodes [16].

To increase the electrochemical surface area, surface modification has been used with various electrode materials [34]. These techniques include metal coatings, metal nanostructure (nanopillar, -rod, -flake, -grain) coating, carbon-based material (CNT, graphene) coating, composite material (CNT-Au composite) coating [2]. Metal coating over the electrode area would impede the light transmittance and is therefore not suitable for optogenetics application. Metal nanostructures, however, could be an option. Nanoparticles have been used widely since they have a high surface-area-to-volume ratio. Gold nanoparticles are favoured for this purpose due to their high specific surface area, high conductivity, and biocompatibility [34]. Another method to increase the electrochemical surface area is to use porous material [26].

### 3.3.3.1. Porous graphene electrodes

Porous graphene is achieved by laser pyrolysis by Lu et al. [26]. The resulting 3D graphene foam (figure 3.10) electrodes showed great capabilities. Chemical doping with nitric acid was adopted to improve the electrode even further. The impedance at 1kHz for the gold electrode ( $62\,500\ \mu\text{m}^2$ ) was measured  $27.3\ \text{k}\Omega$ , which was compared to graphene ( $90\,000\ \mu\text{m}^2$ ), which showed  $637\ \Omega$  for undoped and  $519\ \Omega$  for the doped electrode. Impedance remained stable over 28 days in saline. The CIC for undoped porous graphene was reported  $2\ \text{mC}/\text{cm}^2$ , which was increased even further with doping to  $3.1\ \text{mC}/\text{cm}^2$ . This result is greatly above the monolayer and multilayer graphene electrodes mentioned earlier (up to  $0.8\ \text{mC}/\text{cm}^2$ ). Even after 1 million stimulation cycles, electrodes did not show delamination or degradation. Furthermore, in vivo tests showed that porous graphene electrode is viable for recording as well as stimulation without tissue damage [26]. However, the transparency of porous graphene is not sufficient for combining with optical modalities. Furthermore, the laser resolution is not sufficient to create electrodes smaller than  $250\ \mu\text{m}$  in diameter. To reduce the size, using a shadow mask is suggested [26].

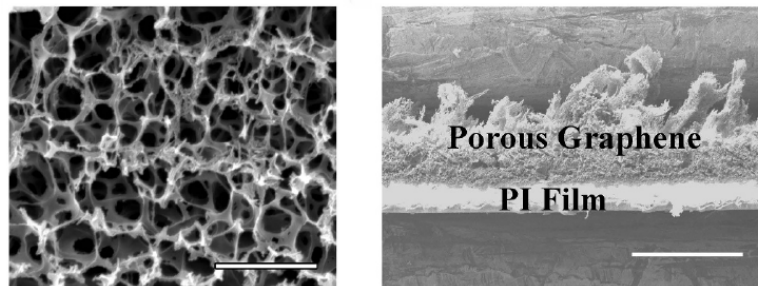


Figure 3.10: Porous graphene achieved with laser pyrolysis. Scale bar:  $2\ \mu\text{m}$ . [26]

### 3.3.3.2. Nanoparticle production methods

Nanoparticle production methods are divided into two categories: top-down, where the particle size is reduced, and bottom-up, where the particles are created from chemicals. Top-down refers to the mechanical crushing of the source material, therefore the size range of the particles is broad and there is no control over particle shapes. The bottom-up method, where structures are built up by chemical processes, is based on physicochemical principles of molecular and atomic self-organization. This approach produces more complex structures with better control over size, shape, and size ranges [56]. These methods include liquid phase and gas phase techniques:

- Liquid phase: The precipitation of solids from a metal ion-containing solution [57]. Electrodeposition has been used for electrodes. It is a process where a potential difference is applied to an electrode at an electrolyte interface resulting in electron transfer between the electrode and ionic species in the electrolyte and the subsequent deposition of atoms of that species onto the electrode [58].
- Gas phase: particles are created by producing a vapour of the product material using chemical or physical means. Further particle growth involves condensation (transition from gaseous into the liquid aggregate state), chemical reactions on the particle surface and/or coagulation processes (adhesion of particles), as well as coalescence processes (particle fusion) [57].

### 3.3.3.3. Spark Ablation

The spark ablation method is one of the gas phase nanoparticle production techniques. It includes generating electrical discharges between two electrodes of a desired conductive material and an inert gas to carry the nanoparticles to the substrate (figure 3.11). The spark plasma ablates material from the electrodes, from which nanoparticles form by condensation. Each spark produces a small vapour cloud which is rapidly mixed into an inert gas flow and starts cooling. That results in supersaturated vapour where atomic clusters start to form by condensation, which further combine into larger particles. Thus, the particle size can be regulated by varying the gas flow, which changes the time that the particles have to coagulate. Furthermore, by changing the current that runs through the electrodes, the frequency of the spark is altered, and thus, the number of nanoparticles produced per unit time. The process creates a highly concentrated aerosol of nanoparticles which can be directly printed on a substrate. The particle size is typically between 5 and 20 nm [59].

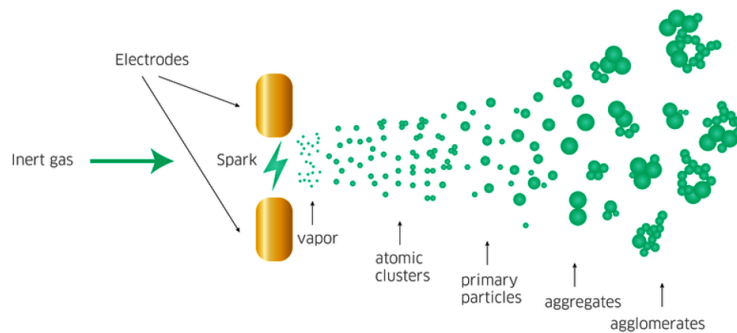


Figure 3.11: Spark ablation technique to create nanoparticles.

### 3.3.3.4. Nanoparticles on graphene electrodes

Graphene with gold particles has been fabricated by Gunes et al. [60]. Gold particles and ions are formed on the graphene surface by  $AuCl_3$  doping. Doping was done separately for four layers, which were then stacked, or doping was done after stacking. Sheet resistance and transmittance were assessed and compared to ITO and nitric acid doped graphene.  $AuCl_3$  doping showed a greater reduction in sheet resistance than  $HNO_3$ , while transmittances were similar. There are no significant differences between layer-by-layer (LbL) of top-doped methods at first. The samples were exposed to air for 21 days, during which the LbL method showed better stability (figure 3.12 [60]).

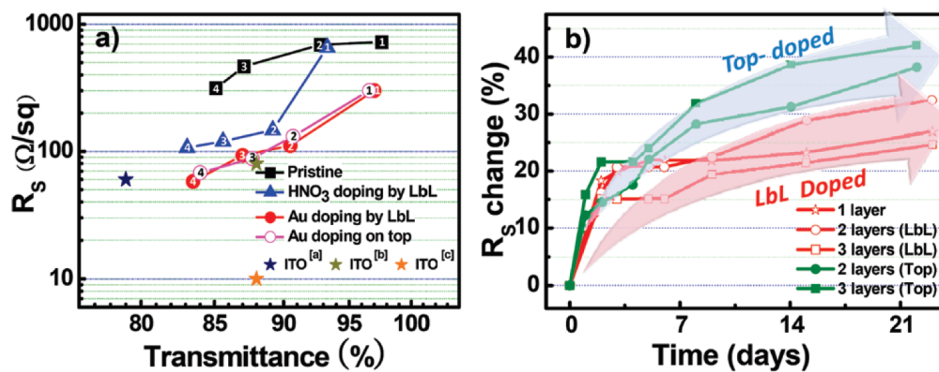


Figure 3.12: (a) Sheet resistance and transmittance measurements of pristine (black), nitric acid doped (blue), and gold doped (red) graphene. The numbers in the markers indicate the number of graphene layers. (b) Stability assessment showing the change in sheet resistance over time [60].

Graphene electrodes with platinum nanoparticles have been reported by Lu et al. [29]. The author claims that graphene has high impedance due to the limitation of quantum capacitance, which could be overcome by creating an alternative conduction path with nanoparticles at the electrode-electrolyte

interface. Platinum nanoparticles would serve as a redox catalyst at the interface and increase the amount of faradaic charge transfer.

Electrodeposition of platinum with various time periods was done. Different coverages of the electrode surface were achieved (figure 3.13), which also affected the characteristics. Impedance and transmittance show a reduction, and CSC an enlargement with increased platinum deposition time. In figure 3.14 comparison between gold, bare graphene, and graphene with platinum nanoparticles can be seen. At 1kHz, graphene with nanoparticles can achieve a 100 times reduction in impedance, but at the same time, the transmittance is reduced to <40%.

Electrodes were tested in vivo for simultaneous electrophysiology recording and two-photon calcium imaging. It was concluded that platinum nanoparticles did not impact the imaging even with the highest coverage, thus adding metal nanoparticles can be a viable solution for optoelectronic devices.

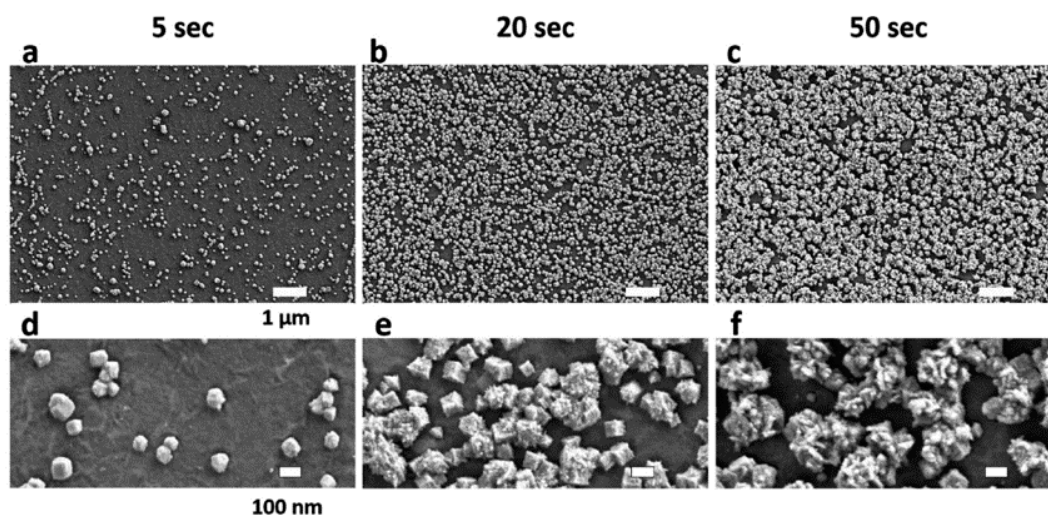


**Figure 3.13:** Scanning electron microscope images of platinum nanoparticles on graphene. a–c) coverage 14.65%, 67.27%, and 88.22% of the graphene surface for 5, 20, 50 s depositions respectively [29]

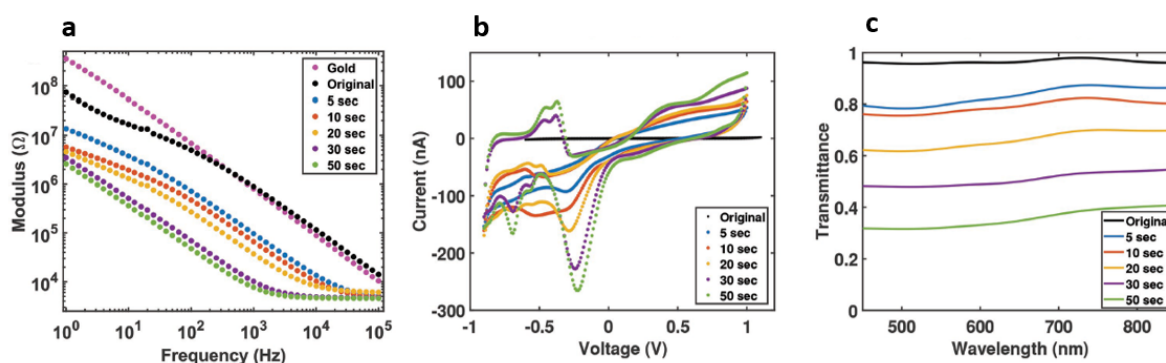


**Figure 3.14:** EIS, CV, and transmittance measurements for gold (magenta) bare graphene (black) and graphene with platinum nanoparticles with various deposition durations [29]

**Table 3.3:** Improved graphene electrodes

Graphene	doping	size ( $\mu\text{m}^2$ )	Z at 1kHz		%T	reference
			Before	After		
Porous graphene	70% nitric acid	90 000	637 $\Omega$	519 $\Omega$	-	[26]
monolayer	70% nitric acid	2 500		541 k $\Omega$		[54]
monolayer	69 % nitric acid	2 500	2.1 $\pm$ 0.3 M $\Omega$	1.5 $\pm$ 0.2 M $\Omega$	97.7%	[55]
monolayer	35% nitric acid	10 000	1.4 M $\Omega$	872 k $\Omega$	>90%	[47]
monolayer	platinum nanoparticles	10 000	1 M $\Omega$	100 k $\Omega$ (5sec) 15 k $\Omega$ (30sec)	>90% (5sec) >50% (30sec)	[29]

Graphene	doping	size ( $\mu\text{m}^2$ )	Before	After	water window	reference
Porous graphene	70% nitric acid	90 000	CIC before: 2 $\text{mC}/\text{cm}^2$	CIC after: 3.1 $\text{mC}/\text{cm}^2$	-1.5 V to 0.8	[26]
monolayer	70% nitric acid	2 500	CSC before: 735 $\mu\text{C}/\text{cm}^2$ (total)	CSC after: 1953 $\mu\text{C}/\text{cm}^2$ (total)	-0.8 V to 0.8 V (200 mV/s)	[54]

### 3.4. Summary of the literature review

An ideal neural electrode is small in size, to have a good spatial resolution, and flexible to reduce tissue damage. Recording electrodes should have low impedance for high SNR recording and stimulation electrodes require large CSC and CIC to be able to induce neural activity. The electrode should be stable and reliable for a long period of time. To increase the spatiotemporal resolution compared to conventional techniques, electrical and optical modalities can be integrated. For this application, many transparent conductive materials have been researched and graphene has shown a lot of potential. Graphene has dramatically better flexibility than ITO and higher broad-wavelength transmittance compared to ultrathin metals. It is also biocompatible and stable.

Transparent graphene electrodes would allow simultaneous optogenetic stimulation and electrical recording, which can improve neuroscience research. Furthermore, imaging of various biological processes under the electrode during electrical stimulation can help to discover the mechanisms of electrical stimulation and neurons' connections in more detail. Combining two-photon imaging and surface recording enables measuring the concurrent activity of the surface and deeper layers. This technology would allow for more accurate neural disorders detection and treatment.

Although graphene has many great properties, the 2D flat surface limits the charge injection capabilities. It also affects the electrode-tissue interface, resulting in higher impedances than conventional electrode materials. Several methods have been researched to improve the electrical characteristics of graphene electrodes. Porous graphene can be fabricated by laser pyrolysis, which shows substantial improvement of CSC and CIC, but it cannot be combined with optical modalities due to opacity. Stacking multiple layers of graphene has shown a trade-off between conductivity and transmittance, but transparency to some level is maintained. However, optogenetics experiments have shown light-induced artefacts with a multilayer graphene electrode but not with a monolayer. Nitric acid doping has been shown to improve the conductivity of graphene without lowering transmittance, although the reduction in impedance is not sufficient to scale an electrode for single-cell resolution, it could be used to improve monolayer graphene for optogenetics application. Adding metal nanoparticles on the electrode surface has shown a great improvement of impedance and CIC, but that is on account of transmittance. Nanoparticles did not affect imaging neural activity, but the impact on simultaneous

optogenetic stimulation and electrical recording has not been investigated.

Comparing electrochemical characteristics of graphene electrodes is troublesome because the exact water window for graphene is unknown. Therefore, a systematic study of the charge injection safety window for graphene should be done. Furthermore, different parameters have been used for CV and VT measurements, which means the results are not comparable. Specific and relevant characterisation settings should be agreed on.

The improvement methods for graphene should also be researched further. The effect of different thicknesses or nitric acid doping of multilayer graphene on the electrical characteristics relevant to neural electrodes has not been reported. Furthermore, the stability of nitric acid doped and nanoparticle-modified graphene after a large number of stimulation pulses has not been measured. Stability testing in a biological environment would be valuable as well. How metal nanoparticles on graphene affect the light-induced artefact caused by optogenetics during recording should be studied.

To summarise, graphene is a suitable material for optoelectronic devices. In order to use graphene electrodes for high SNR recording and tissue stimulation, electrical characteristics should be improved. Stacking graphene layers, nitric acid doping, or adding metal nanoparticles are promising methods to achieve that for graphene neural electrodes.

# 4

## Methods

The first goal of this project is to fabricate graphene electrodes and characterise them with neural electrode characterisation techniques. In this work, graphene electrodes are created using a microfabrication process which is described in this chapter. Electrochemical characterisation tools are used to assess the performance of these electrodes. The measurement details are given in this chapter. Furthermore, for optical transmittance measurement, graphene had to be transferred onto a transparent substrate. The transfer method will be presented.

The second goal of this project is to evaluate the effect of various improvement methods on multi-layer graphene electrode's performance. For that, graphene with different thicknesses is achieved by varying the time in the CVD process. Gold, platinum, and gold and platinum alloy nanoparticles are deposited on the surface of graphene electrodes with spark ablation technology. Nitric acid is used for p-type doping of graphene. Electrochemical measurements are performed before and after introducing the improvement method to quantify the effect. Details of these processes are described in this chapter.

### 4.1. Graphene electrodes and van der Pauw structures fabrication

The flexible implants with graphene have been developed in the group earlier by Velea [61] and Wardhana [62]. The final design consisted of graphene electrodes and tracks with PDMS encapsulation. However, the full fabrication process for these implants is time-consuming and complex. To have more devices faster for electrochemical characterisation, a simpler design was opted.

Microfabrication techniques are used to create the electrodes on a wafer level, which provides accuracy and reproducibility. The process flow of the fabrication of the graphene electrodes used in this work is described in this section. The fabrication was done in Else Kooi Laboratory (EKL) at TU Delft.

Graphene electrodes used in this work were fabricated on a single side polished, 500  $\mu\text{m}$  thick, 4-inch silicon wafer. All structures were fabricated on the front side of the wafer. The process started with growing 300 nm wet thermal oxide at 1000°C on the wafer to electrically insulate the graphene structures from the wafer. After that, 50 nm of molybdenum (Mo) catalyst was sputtered at 50°C and patterned with the photolithography process. The masks used for photolithography were designed by Velea for spinal cord implants for mice [61]. Next, 2.1  $\mu\text{m}$  of positive photoresist SPR3012 was spin-coated on the wafer and exposed with UV light through a chromium mask with the implant structure designs (figure 4.1a). The photoresist was then developed with Shipley MF322 developer, after which the photoresist remained only on the areas of the desired structures. Molybdenum was dry-etched in Trikon  $\Omega$ mega 201, or AMS110 when Trikon  $\Omega$ mega was unavailable. After that, the photoresist was removed with oxygen plasma.

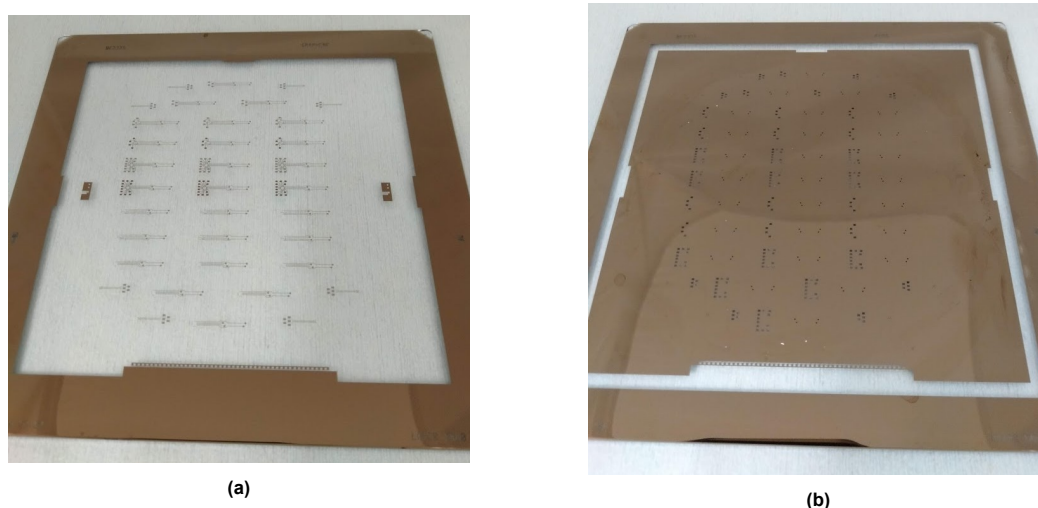


**Figure 4.1:** (a) Mask for Mo etching with graphene structures design. (b) Mask for openings of electrodes and contact pads.

Next, graphene was grown on the Mo catalyst using CVD in the Aixtron BlackMagic tool. The previously determined standard recipe at 915°C resulted in low quality graphene. Raman spectroscopy did not show distinct peaks, as seen in figure 4.2a. This was possibly due to the decrease in the amount of power supplied. The heaters and thermocouples in the tool had been swapped and it may have changed the heat coupling, however, the exact cause is unknown. A new recipe was created, where the bottom heater of the chamber was set to 950°C and the top heater to 1050°C. Preannealing of Mo was done for 20 min to remove oxidized Mo from the surface, after which  $CH_4$  was introduced to the chamber for 20 min. To achieve thicker graphene,  $CH_4$  was kept in the chamber for 40 min or 60 min. Raman spectroscopy of the resulting graphene is given in figure 4.2b which shows pronounced peaks and a low D peak, demonstrating higher quality graphene.

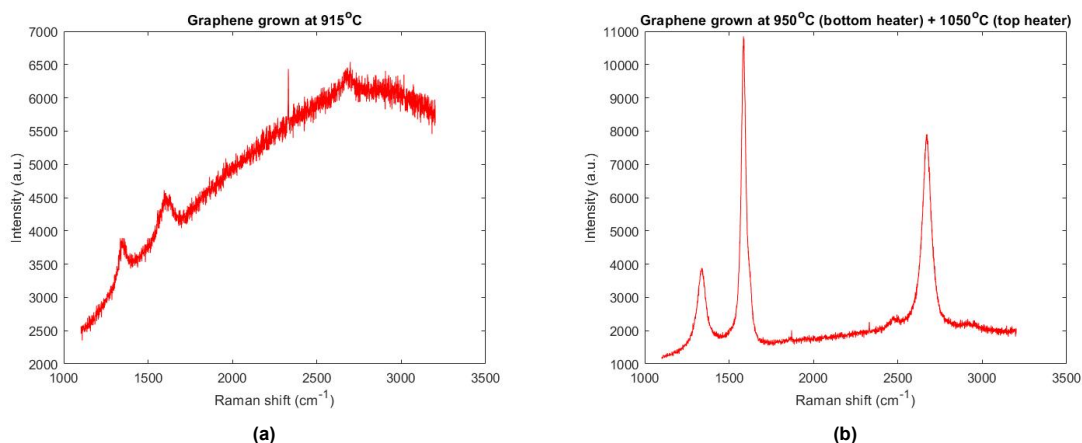


**Figure 4.2:** (a) Raman spectroscopy of graphene grown at 915 °C. (b) Raman spectroscopy of graphene grown with bottom heater at 950°C and top heater at 1050°C.

In this work, a transfer-free process for graphene fabrication is used, inspired by Vollebregt et al. [38]. Mo can be etched from under the graphene with hydrogen peroxide ( $H_2O_2$ ). At first, wet etching of Mo with  $H_2O_2$  was tried after graphene growth. The graphene layer should attach to the  $SiO_2$ . However, the adhesion is not sufficient and many structures broke during rinsing due to the large dimensions and lack of polymer support. Dry etching with  $SF_6$  gas was then tested in the AMS110 tool. However, that method introduced many defects into the graphene layer, based on Raman spectroscopy assessment before and after Mo etching. It could be possible to develop the etching recipe further, but since it falls out of the scope of this thesis, it was not pursued. It was then decided to etch Mo under graphene in the later steps.

To insulate the tracks from the saline during measurements, 4  $\mu\text{m}$  thick photoresist AZ ECI 3027 was spin-coated on the wafer. It was then exposed, using a mask with contact and electrode openings structures (figure 4.1b), and developed. For some samples, wet etching of Mo with  $\text{H}_2\text{O}_2$  was done after adding the photoresist. Thus, Mo was removed on the contact and electrode openings. After that, the wafer was manually diced using a diamond cutter. Stainless steel 7-strand wire with 76.2  $\mu\text{m}$  bare diameter (139.7  $\mu\text{m}$  with coating) was bonded to the contact pad of the device with silver (Ag) ink. The wire was further secured with a drop of PDMS over the contact pads area. For later samples, Mo etching on the electrodes was done only after wire bonding, as shown in figure 4.3, thus, leaving Mo still under the graphene on the contact pad. This was done to improve the contact between the wire and the sample. The fabrication process is illustrated in figure 4.5, where the different order of steps is shown in the end.

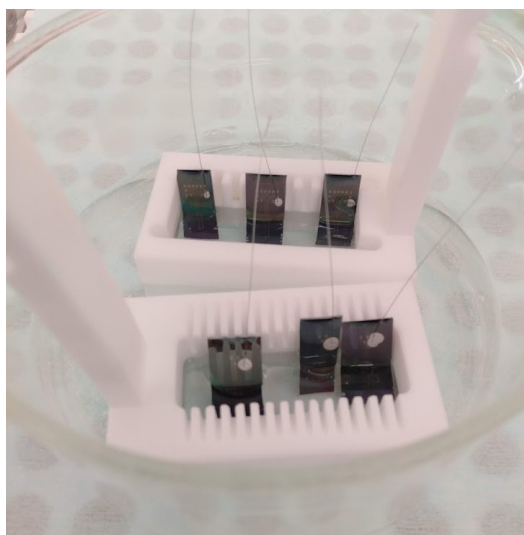


**Figure 4.3:** Etching of Mo only from the electrodes by only half of the device being inside the  $\text{H}_2\text{O}_2$ .

The final structure of the graphene electrode is shown in figure 4.4. The electrode openings have a diameter of 340  $\mu\text{m}$ . The width of the Mo + graphene track is 70  $\mu\text{m}$ , and the size of each contact pad is 650 x 510  $\mu\text{m}$ . As seen in figure 4.4, the wire was bonded to only one contact pad on each device to avoid an accidental connection between two contact pads.

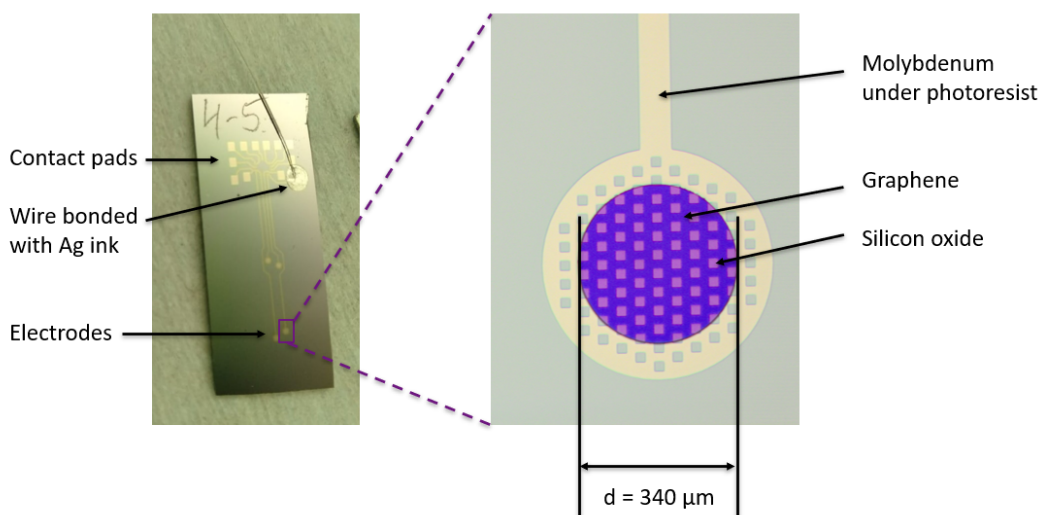


**Figure 4.4:** The final structure of the graphene electrode device. On the close-up image, graphene is with the darker purple color and silicon oxide under it with lighter pinkish color. The yellow circle around the electrode is Mo under photoresist, which is not etched.

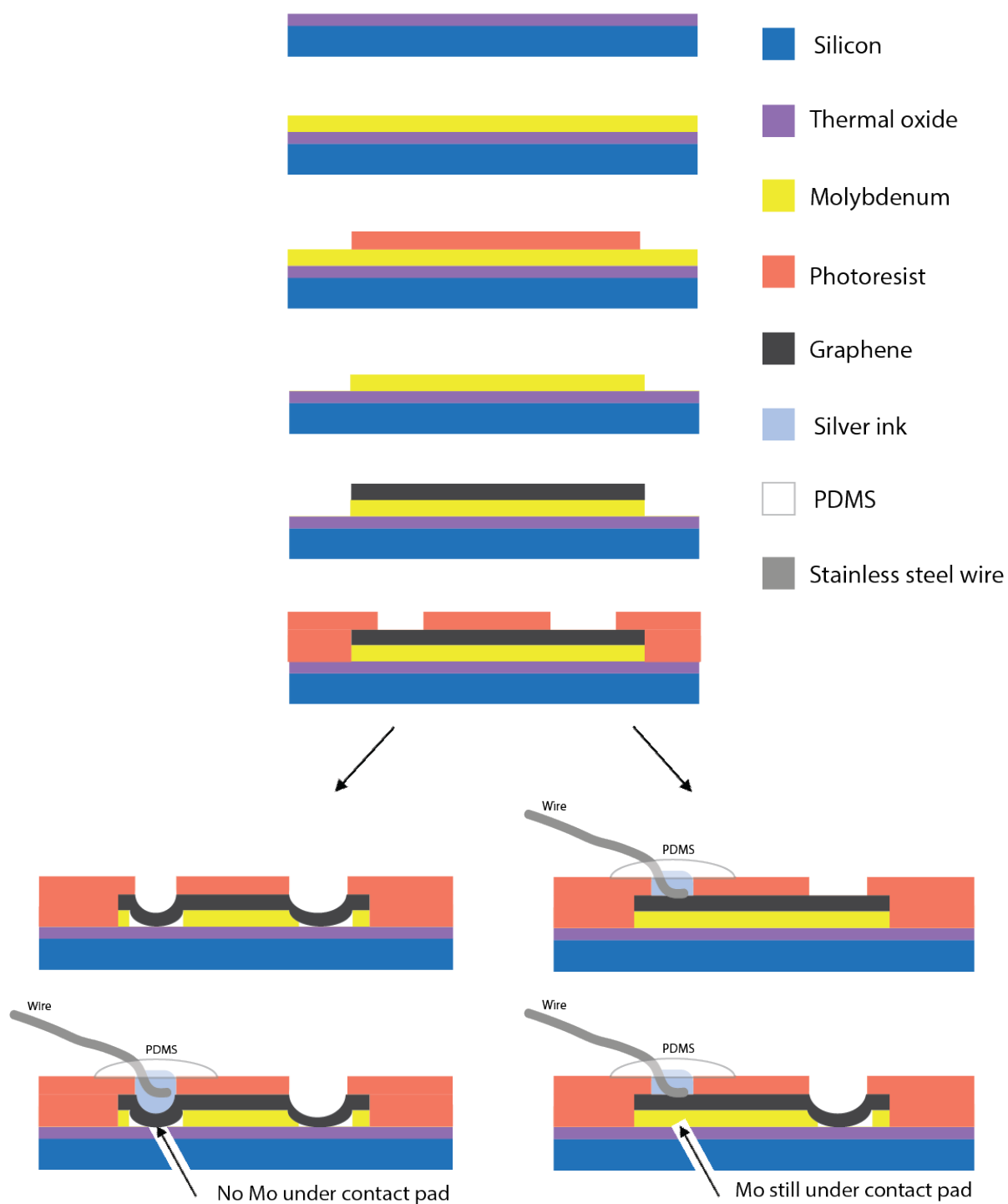


**Figure 4.5:** The scheme of the fabrication process of graphene electrodes.

To measure sheet resistance, van der Pauw like structures were used (figure 4.6a). During the lithography step after Mo deposition, exposure was done with 2 masks. For half of the wafer, previously shown graphene structures mask was used, and for the other half, a mask with van der Pauw structures was used. Furthermore, for the insulating photoresist, half of the wafer was exposed with the contact and electrode openings mask, and the half with van der Pauw structures was completely exposed, so there would be no photoresist left on that half. The resulting structures are shown in figure 4.6b. Dots with Ag ink were added to the extremities of the structures to reduce damage to the graphene when placing measurement probes on it. Furthermore, the dots were added only to three structures out of the group of six to prevent multiple current paths.

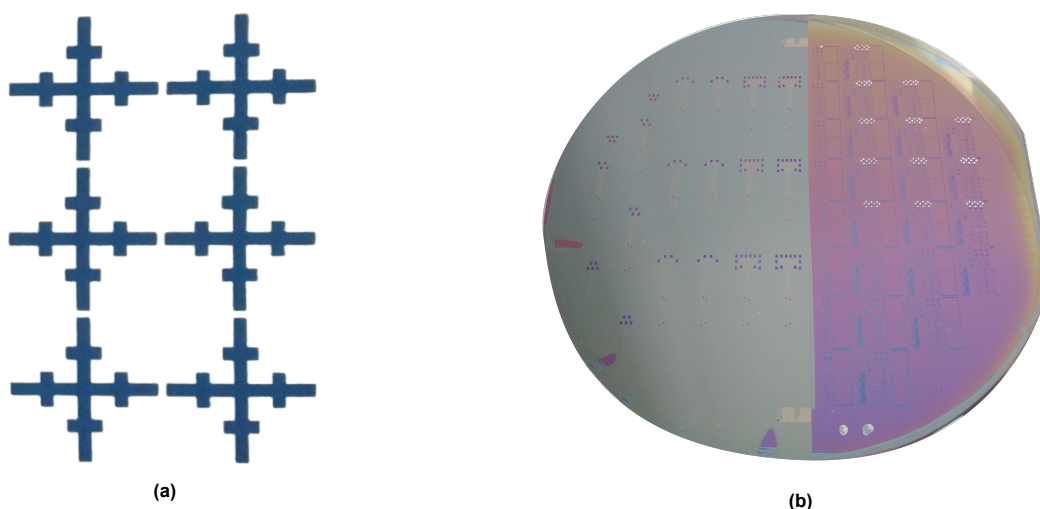


**Figure 4.6:** (a) A group of six Van der Pauw like structures used for 4-point measurements. (b) Wafer with half implant structures and half van der Pauw structures.

## 4.2. Graphene transfer

Like mentioned before, the graphene electrodes in this work are fabricated on a silicon wafer and not on a transparent substrate. Therefore, for optical transmittance measurements, graphene had to be transferred to a glass slide.

The method used in this work is different from the techniques mentioned in the literature. A full wafer of graphene was grown on non-patterned Mo. The wafer was then manually diced into roughly  $2\text{ cm}^2$  pieces. These were then placed in a beaker where  $\text{H}_2\text{O}_2$  was added just until the height of the silicon piece with graphene. Mo then started to etch from the sides towards the centre, as illustrated in figure 4.7. After all the Mo was etched, the graphene was separated from the silicon piece and floated on the surface of the liquid while the silicon fell to the bottom of the beaker. DI water was then added very gently with a pipette until the level of the liquid rose about 2 cm. The floating graphene was then scooped on the glass slide. In the case when graphene kept slipping away, 1 drop of Triton X-100 was added to 1 litre of DI water and 50 ml of triton-water solution was added to the  $\text{H}_2\text{O}_2$  in the beaker to reduce surface tension. The resulting glass slides are shown in figure 4.8

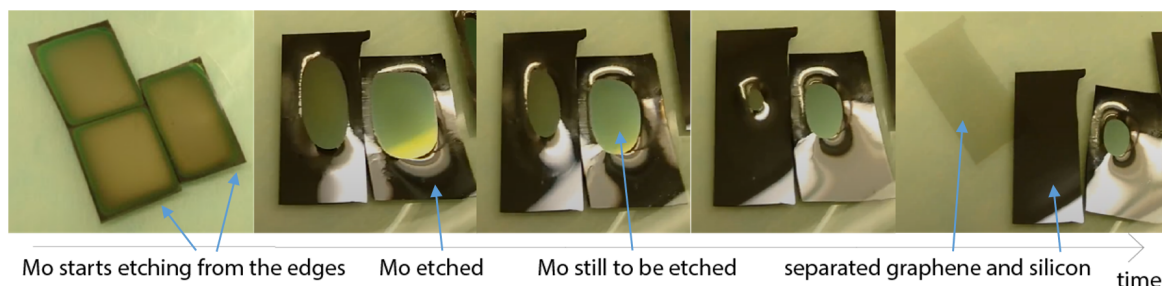


**Figure 4.7:** The Mo etching process for graphene transfer to a glass slide.

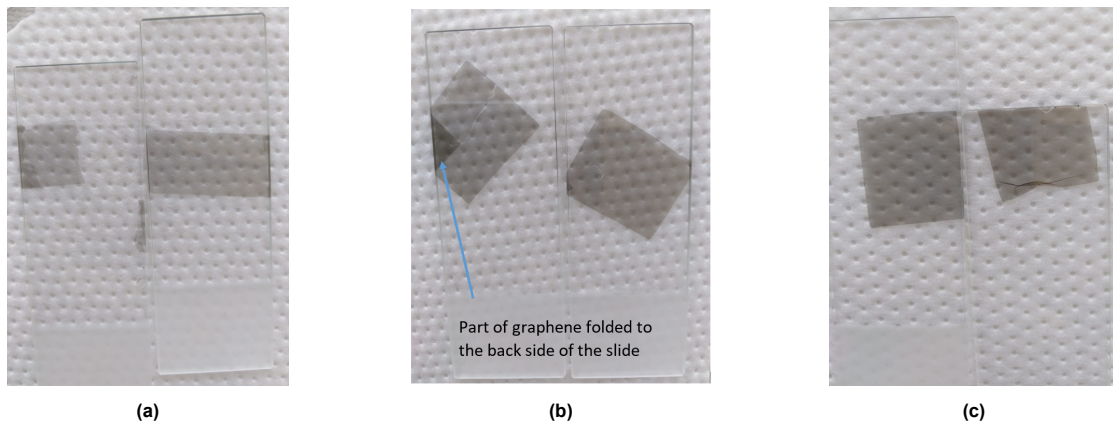
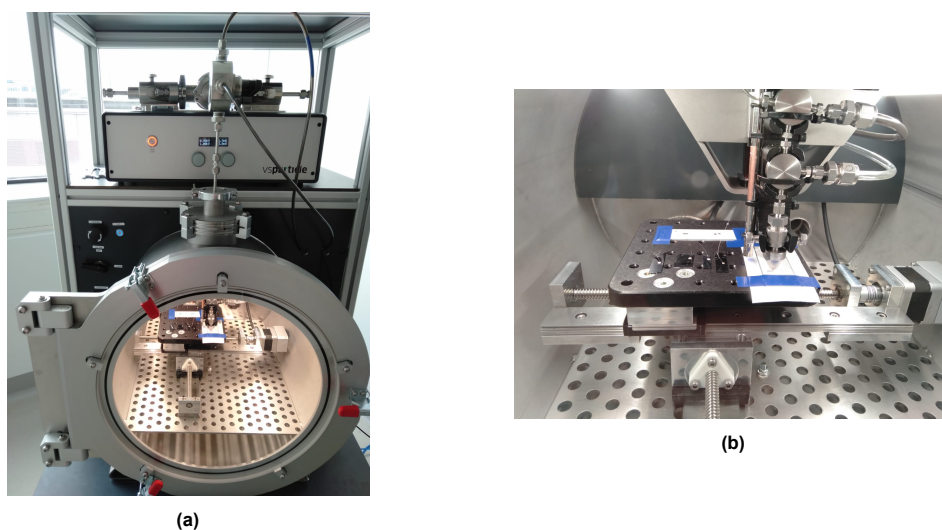


**Figure 4.8:** Graphene grown for 20 min (a), 40 min (b), and 60 min (c) transferred to a glass slide.

### 4.3. Nanoparticle deposition

One of the methods to improve the electrical characteristics of graphene is adding nanostructures to its surface. In this work, gold and platinum nanoparticles were chosen. Gold nanoparticles (AuNPs) have a high surface-area-to-volume ratio, and therefore, are expected to increase the electrochemical surface area, and in turn, lower the impedance [34]. Platinum is a traditionally used material in stimulation electrodes. Adding platinum nanoparticles (PtNPs) on the surface of graphene should increase the amount of faradaic charge transfer over the electrode-electrolyte interface and thus, increase the CSC [29]. Furthermore, gold and platinum alloy nanoparticles (Au+Pt NPs) have shown to possess nanoporosity [63]. Thus, with the very rough surface, they could improve the electrical characteristics even further. In this work, gold, platinum, and gold and platinum alloy nanoparticles are used.

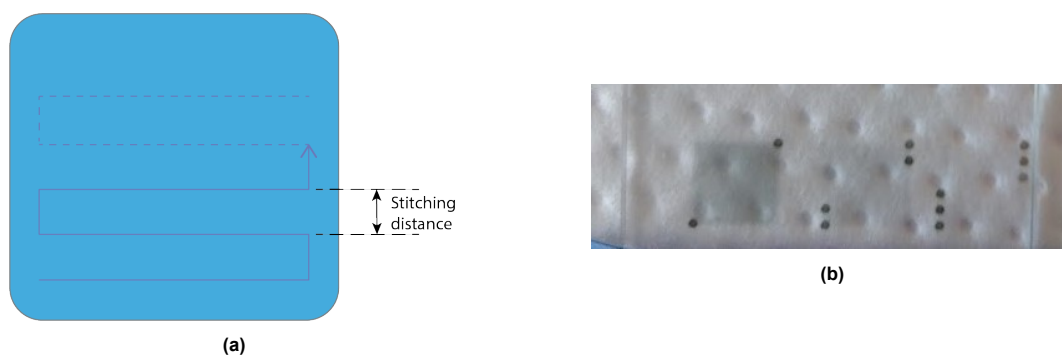
Nanoparticles were deposited using spark ablation technique with VSP-G1 nanoparticle generator connected to VSP-P1 nanostructured material printer (VS Particle) shown in figure 4.9. The spark ablation technique is advantageous for this project since it is a local and dry process. That means it can be used with soft polymers, which are used for encapsulation of the implants. Soft polymers can be permeable for vapours, and thus, wet chemical processes should be avoided. With the spark ablation technique, no further processing steps are required, which makes it also time-effective. Furthermore, the size of the nanoparticles produced with this technique is 5-20 nm. The ratio between the increase in the surface area and the area obstructed for light is larger for smaller nanoparticles. Thus, better electrical characteristics and optical transmittance is expected compared to the 100-200 nm Pt NPs reported in literature [29].



**Figure 4.9:** (a) VSP-G1 nanoparticle generator and VSP-P1 nanostructured material printer (VS Particle). (b) Devices and a glass slide in the chamber of the printer.

Optimisation of the printing parameters had to be done to achieve less than a monolayer nanoparticle coverage with various densities. The spark was generated with 1 kV, and the argon gas flow between the electrodes was set to 1.5 l/min. The current was first set to 8mA, which resulted in too thick layers of nanoparticles for this project. Therefore, the current was lowered to 3mA to achieve transparent layers. For Au+Pt NPs, the gas flows from two generators - one with gold electrodes and one with platinum electrodes - were combined and the Au NPs and Pt NPs combined during agglomeration. The settings for the generators were identical: 1kV, 3mA, and 1.5 l/min gas flow for each generator. The outputs for Au and Pt with the same parameters are different. With the settings used in this work, maximum output for Au is 1.49 mg/h, and for Pt 0.93 mg/h. Thus, the expected ratio of Au to Pt in the allow nanoparticles is roughly 6:4 [64].

The first tests included printing in one location for one second. This is the minimum recommended time for printing. Lower than that, the aerosol flow does not have time to stabilise and the result could be not reproducible. However, the desired density was not achieved. The nanoparticles were then printed in a line over the electrode area. The diameter of the electrode is 340  $\mu\text{m}$ . Depending on the nozzle height (distance from the substrate), the line widths were between 400  $\mu\text{m}$  and 650  $\mu\text{m}$  with 0.8 to 1.6 mm nozzle height. Therefore, the line width is enough to cover the electrode area, however, that did not result in a homogeneous coverage. A pattern with several overlapping lines printed at high speeds was then opted for. To make sure that the whole electrode area is covered, a square with 500  $\mu\text{m}$  width was printed by moving the nozzle back and forth with 100  $\mu\text{m}$  stitching distance. The pattern is illustrated in figure 4.10a. Nanoparticles were also printed on glass slides for optical transmittance assessment in a 5x5mm square, shown in figure 4.10b.

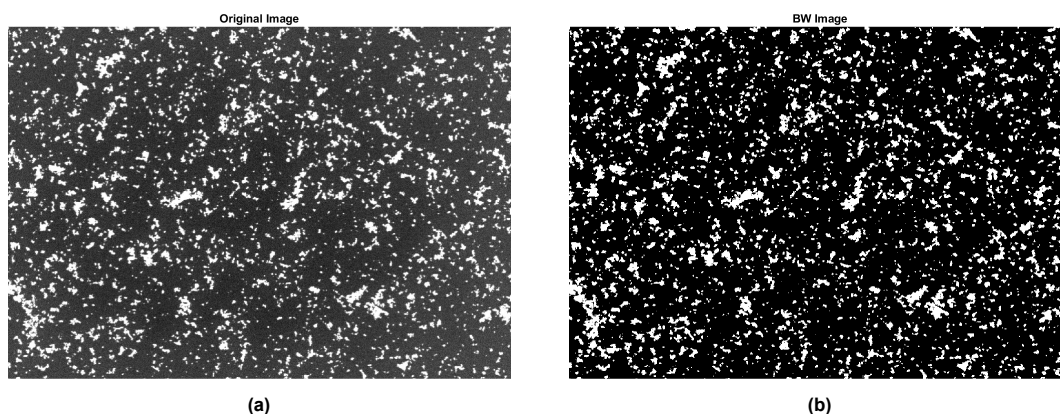


**Figure 4.10:** (a) The printing pattern with overlapping lines used in this work. (b) Nanoparticles printed on a glass slide in a 5x5 mm square. The darker dots show the corners of the printed squares.

The densities were calculated from Scanning Electron Microscope (SEM) (Hitachi Regulus 8230) images taken with 3kV and 50000x magnification. The grey-scale SEM images were converted to black-and-white images (figure 4.11) using MATLAB R2019b (MathWorks). The pixels of the image were considered white if the luminance was higher than 0.45. The white pixels represent the area covered with nanoparticles and the percentage of white pixels out of all pixels was considered the density of the nanoparticles. The densities of gold and platinum nanoparticles were measured for various printing speeds and nozzle heights from the substrate. Unfortunately, due to lack of time Au+Pt NPs densities could not be optimised, so they vary from the other densities. The desired densities were 10%, 25%, and 50% coverages. The final print settings used and densities calculated based on 4-8 SEM images for Au, Pt and Au+Pt NPs are given in table 4.1.

**Table 4.1:** The nanoprinter settings and achieved densities of NPs

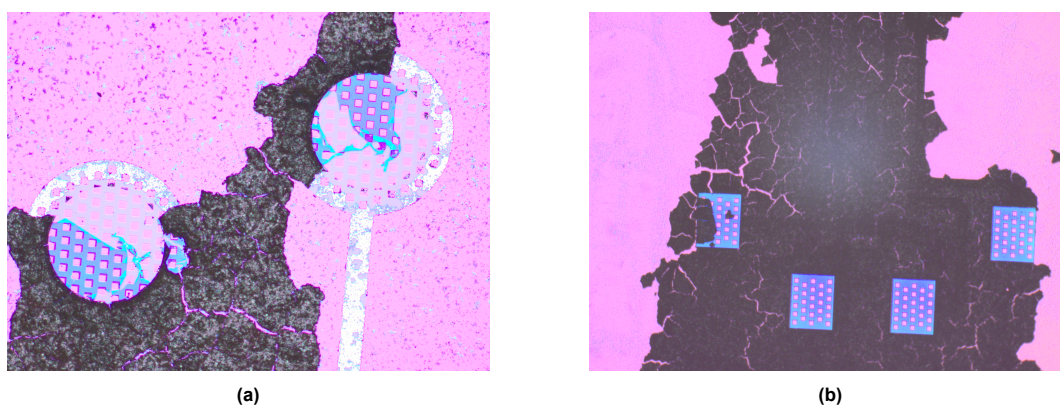
Generator settings	1kV, 3mA	Nozzle height	1.2 mm	Pattern size	500x500 $\mu\text{m}$
Gas (Ar) flow	1.5 l/min	Nozzle size	0.2 mm	Stitching distance	100 $\mu\text{m}$
<b>Au NPs</b>		<b>Pt NPs</b>		<b>Au+Pt NPs</b>	
Nozzle speed	Density	Nozzle speed	Density	Nozzle speed	Density
100 mm/min	47.3 $\pm$ 5.6 %	70 mm/min	47.4 $\pm$ 2.0 %	170 mm/min	29.3 $\pm$ 0.5 %
300 mm/min	26.2 $\pm$ 4.7 %	215 mm/min	22.1 $\pm$ 1.7 %	515 mm/min	14.6 $\pm$ 1.6 %
900 mm/min	10.4 $\pm$ 0.2 %	660 mm/min	8.2 $\pm$ 0.1 %	1550 mm/min	6.4 $\pm$ 0.5 %

**Figure 4.11:** (a) The original grey-scale SEM image. (b) The SEM image converted to a black-and-white image.

#### 4.4. Nitric acid doping

Nitric acid doping has shown to give graphene p-type doping, and thus, improve the electrical characteristics [52]. Furthermore, higher concentration acid has shown to lower the impedance more [47]. In this work, 69.99%  $\text{HNO}_3$  and a diluted acid with 35% concentration was used.

As mentioned earlier, photoresist was used as the top insulating layer on the devices. When placing the devices in the 69.99%  $\text{HNO}_3$ , the photoresist was removed (figure 4.12). To avoid that, the samples were baked for 1h at 70°C, after which the photoresist was not significantly damaged based on visual inspection with a microscope.

**Figure 4.12:** Electrodes (a) and contact pads (b) damaged after nitric acid doping.

Since  $HNO_3$  also etches Mo, the last process step of removing Mo from the electrodes and  $HNO_3$  doping were done simultaneously. However, since the measurement results of pristine graphene can vary, it was not possible to quantify the potential improvement. Therefore, for later samples, Mo was etched first with  $H_2O_2$  and the before-measurements were carried out. After that, the  $HNO_3$  treatment and after-measurements were performed (figure 4.13). For the  $HNO_3$  treatment, the electrodes were submerged in  $HNO_3$  for 4 minutes and then rinsed in DI water for 4 minutes.

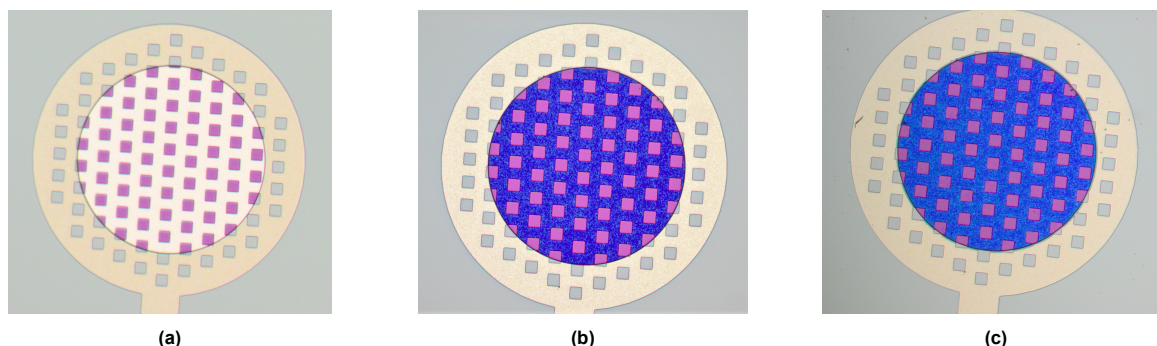


**Figure 4.13:** (a) The electrode before Mo etching. (b) The electrode after Mo is removed with  $H_2O_2$ . (c) The electrode after  $HNO_3$  treatment

## 4.5. Electrochemical measurements

CV and EIS were used to assess the electrochemical properties of the graphene electrodes. The measurements were performed in a three-electrode set-up (WE, CE and RE). The electrodes were immersed in phosphate-buffered saline (PBS) and kept inside a Faraday cage during the measurements. The device with graphene electrode served as the WE and only the half of the device with the electrode was immersed in saline. The RE was placed as close to the graphene electrode as possible, while the CE was in the bottom of the beaker. All the electrodes were connected to a potentiostat (Autolab PG-STAT302N) which was used to set the voltage and measure the current. The set-up is illustrated in figure 4.14.

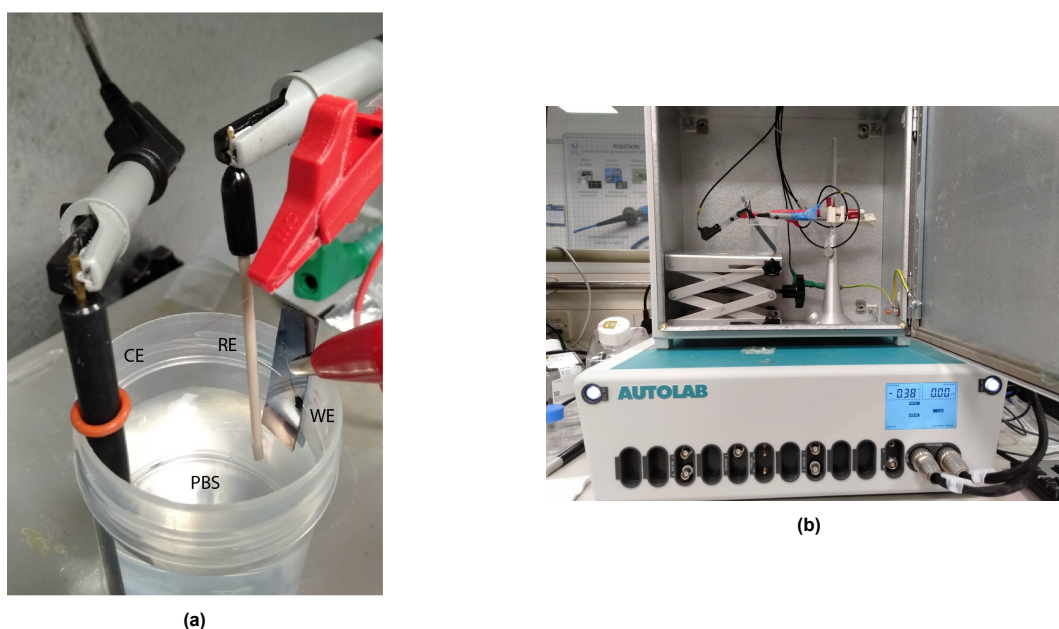


**Figure 4.14:** (a) Three-electrode set up immersed in PBS. (b) Autolab potentiostat used for CV and EIS measurements.

### 4.5.1. Electrochemical impedance spectroscopy

A sinusoidal voltage waveform with 10mV RMS was used for EIS. The frequency ranged from 1 Hz to 100 kHz. The graphene electrode was used as the working electrode, a platinum electrode served as the counter electrode and at first, silver/silver chloride (Ag/AgCl) as the reference electrode. During EIS measurements it was noticed that the phase in the high-frequency range is returning to higher values which was not expected (figure 4.15a). This might happen due to the high intrinsic impedance of the reference electrode. Thus, the reference electrode was switched to platinum wire for EIS measurements which solved that issue (figure 4.15b).

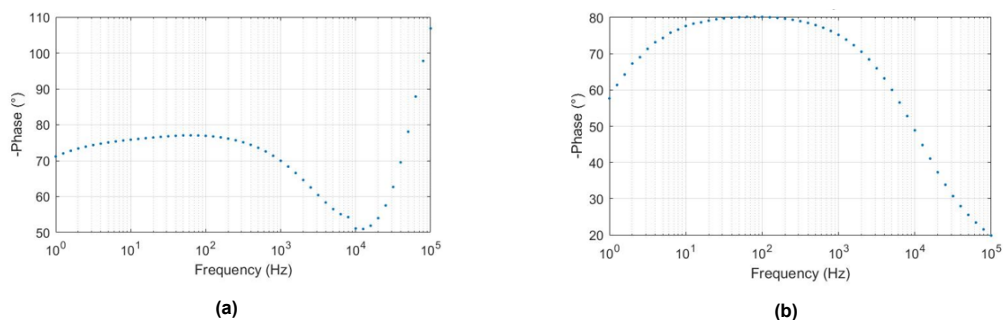


**Figure 4.15:** EIS measured against (a) the Ag/AgCl reference electrode and (b) against a platinum wire.

### 4.5.2. Cyclic voltammetry

As mentioned earlier, the water window for graphene is not exactly known. Therefore, the first devices were used to determine the approximate water window. As seen in figure 4.16a, at the lower potential limit the current peaks and does not stabilise after that, which means that the water reduction is already happening. In figure 4.16b, water oxidation is shown. Based on this, the water window for this work was chosen to be -0.8 V to 0.6 V (figure 4.16c). This was used as the CV potential range for all the electrodes (if not mentioned otherwise).

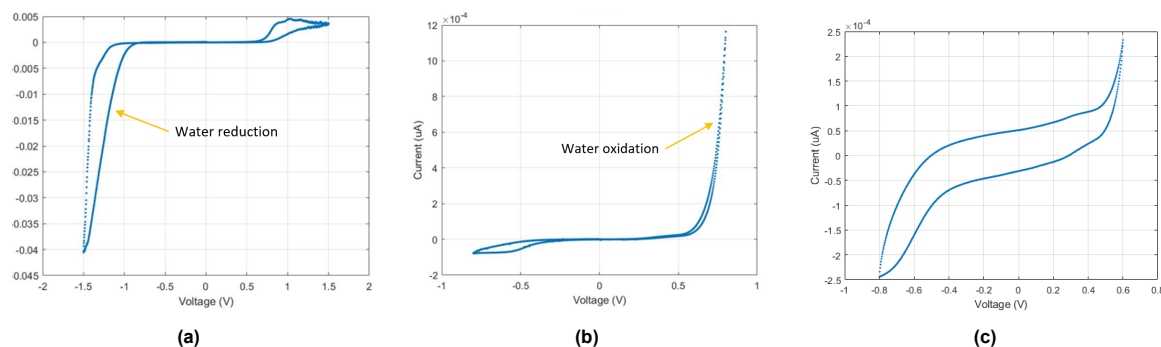


**Figure 4.16:** (a) Water reduction is demonstrated at the low voltage. (b) Water oxidation is shown at high voltage. (c) CV with the water window chosen after analysis.

The CV measurements were performed with various sweep rates. As mentioned in the literature, the CSC depends highly on the sweep rate. Thus, to compare the results with the ones reported in the literature, the same sweep rate should be used. In this work, the following sweep rates were used: 0.1 V/s, 0.2 V/s, 0.6 V/s, and 1.0 V/s. The CV scan started at 0 V, then the potential increased until the upper limit (0.6 V). Next, the potential decreased to the lower limit and after that reached back to 0 V. The scan was repeated 3 times to stabilise the signal, and the third scan was used in the calculation of CSC.

The measurement data was then imported to MATLAB, where the voltage data was converted to time using the sweep rate and the current is divided with the electrode area ( $90\,792\ \mu\text{m}^2$ ) to obtain the current density. CSC is calculated from the time integral over the current measured during the CV. For cathodic CSC, only the negative current part is considered. The integral is calculated using a trapezoidal numerical integration. The CSC is typically expressed in  $\mu\text{C}/\text{cm}^2$ .

## 4.6. Four-point measurements

Four-point probe measurements were performed with a probe station by Cascade Microtech. The four probes were positioned on the Ag ink dots on the extremities of the van der Pauw like structures (figure 4.17). The current was forced between probes 1 and 2 ( $I_{1,2}$ ), by setting the probe 1 potential from -1 V to 1 V with 8 mV steps and probe 2 acting as ground. The voltage was measured between probes 3 and 4 ( $V_{3,4}$ ). The recorded data was exported to MATLAB, where the sheet resistance was calculated with equation (3) for each point, which were then averaged, excluding the values around  $I=0$ .

$$R_s = \frac{V_{3,4}}{I_{1,2}} * \frac{\pi}{\ln 2} \quad (3)$$

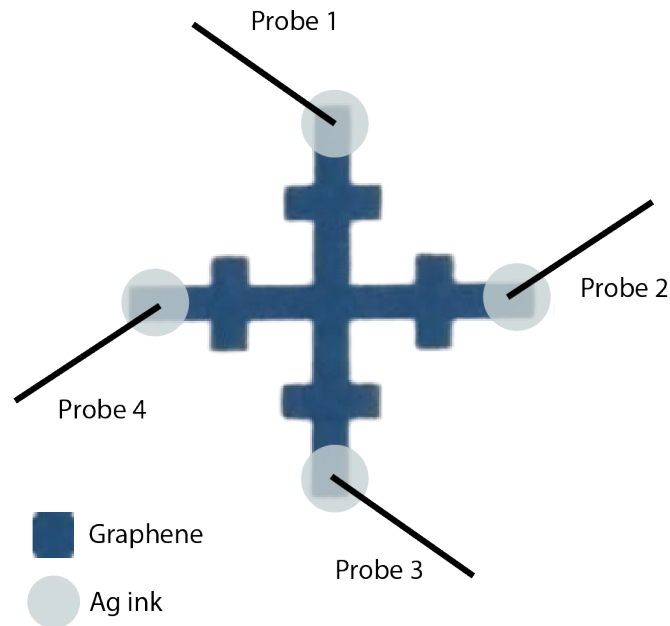


Figure 4.17: The four-point probe measurement scheme.

## 4.7. Optical transmittance measurements

Optical transmittance was measured using a UV/Vis spectrometer (PerkinElmer LAMBDA). The wavelength range for the measurement was from 300 nm to 800 nm. Transmittance measurements were performed on graphene grown for 20 min, 40 min, and 60 min transferred on a glass slide. From the results, the number of graphene layers was calculated by dividing the total absorbance by the absorbance of monolayer graphene (2.3 %). The transmittance of Au, Pt, and Au+Pt NPs printed on a glass slide was measured as well. The measurements were done also for only the glass slide for reference. The absorbance of the glass was then subtracted from the absorbance of the other samples to achieve the optical transmittance of these samples.

# 5

## Results and discussion

In this chapter, the results of the electrochemical characterisation of graphene electrodes are presented and discussed. Optical transmittance measurement results will be given. The effect of the improvement methods (growing thicker graphene, adding Au, Pt, Au+Pt NPs, and nitric acid doping) on the performance of the electrodes will be presented and discussed.

### 5.1. Pristine graphene electrodes

The characterisation results for electrodes fabricated with graphene grown for 20 min are presented and discussed in this section. EIS measurement results and the impedance magnitude ( $|Z|$ ) at 1 kHz, as well as cyclic voltammetry (CV) measurements and calculated charge storage capacities (CSC), are reported.

#### 5.1.1. Electrochemical impedance spectroscopy

EIS measurements were done on 52 devices. The first 25 devices have only graphene on the contact pad (Mo was removed). Out of those, ten electrodes showed expected capacitive behaviour, as illustrated in figure 5.1a. Two devices showed resistive behaviour (figure 5.1b). The behaviour of the remaining 13 electrodes was unexpected. An example is shown in figure 5.1c. This variation was assumed to be the result of bad contact between the wire and the device. Thus, it was decided to keep Mo under graphene on the contact pads.

27 devices with Mo and graphene on the contact pads were measured. Out of those, six devices exhibited resistive behaviour. Devices with resistive behaviour were assumed broken and were excluded from further analysis. Ten electrodes indicated capacitive behaviour. However, 11 devices still showed an unexpected result. Several test measurements were performed to confirm the correct functioning of the potentiostat and its contacts, which all demonstrated proper performance. Furthermore, since silicon is conductive, the participation of silicon in the reactions was tested, which did not show the involvement of silicon. It is unknown what causes these different behaviours, but the contact between the wire and the device likely plays a significant role.

Instead of silver ink, carbon paste was used to attach the wire to the structure for 6 devices with Mo and graphene on the contact pad. None of the electrodes showed the expected capacitive behaviour. Three electrodes showed resistive behaviour. The other three devices exhibited the unexpected behaviour. The average  $|Z|$  at 1 kHz for these electrodes was  $25\,813 \pm 12\,351 \, \Omega$ . These electrodes were not included in the further analysis.

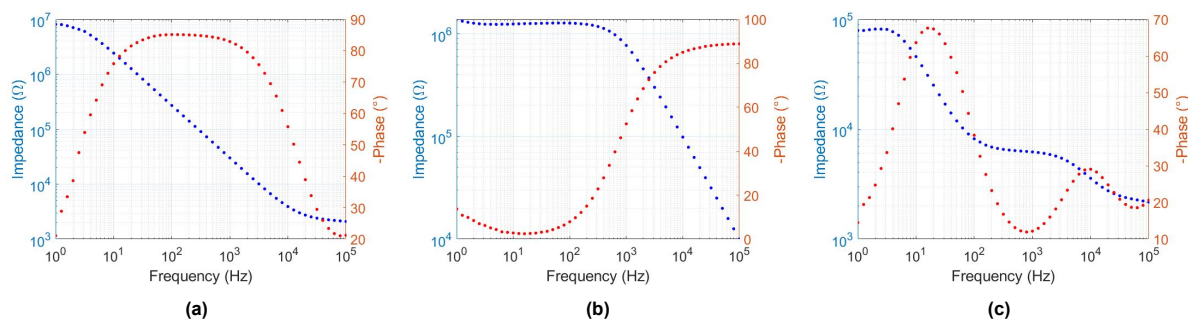


**Figure 5.1:** Example EIS measurements showing (a) capacitive, (b) resistive, and (c) unexpected behaviour.

EIS measurements results are divided into two groups, with Mo and graphene on the contact pad and the devices with only graphene. The average impedance at 1kHz, which is typically reported for neural electrodes, varies greatly between the two groups due to the contact quality between the wire and the device. A distinction between electrodes with expected capacitive behaviour and unexpected behaviour is also made. The means and standard deviations (SD) of impedances at 1kHz for the different types of devices are given in the table 5.1.

**Table 5.1:** The average impedance magnitude at 1 kHz for pristine graphene electrodes

contact pad	behaviour	nr of samples	$ Z $ at 1 kHz ( $\pm$ SD)
only graphene	capacitive	10	$29\,531 \pm 8\,877 \Omega$
	unexpected	13	$34\,599 \pm 19\,706 \Omega$
	total	23	$32\,396 \pm 15\,832 \Omega$
Mo + graphene	capacitive	10	$12\,753 \pm 14\,594 \Omega$
	unexpected	11	$11\,748 \pm 5\,967 \Omega$
	total	21	$12\,226 \pm 10\,673 \Omega$

It is interesting to note that the SD is extensive for devices with Mo and graphene on the contact pad that showed capacitive behaviour. The distribution of the results can explain this. The average  $|Z|$  at 1 kHz for four devices from one wafer is  $29\,700 \pm 700 \Omega$ . The other six devices (from 2 wafers) have the average  $|Z|$  at 1kHz only  $1\,454 \pm 312 \Omega$ . The lowest measured  $|Z|$  at 1 kHz of all the graphene electrodes was  $993 \Omega$ .

It is not known what might have caused the large difference in impedance values. The wafers had the same fabrication process, but there are possible explanations for the variation in behaviour. Photoresist residues may have remained after Mo patterning, which could have disrupted uniform graphene growth. Although cracks were not seen during a visual inspection, some microcracks or defects may have been induced during the last photoresist patterning and Mo etching from the electrodes. Unfortunately, the Raman spectroscopy tool was unavailable, and thus, the correlation between graphene quality and impedance behaviour could not be investigated.

### 5.1.2. Cyclic voltammetry

Cyclic voltammetry was performed on 27 electrodes. Out of those, 13 devices had only graphene on the contact pad (6 with capacitive and 7 with unexpected EIS behaviour) and 14 devices with Mo and graphene on the contact pad (10 with capacitive and 4 with unexpected EIS behaviour).

Cyclic voltammetry measurements varied greatly between electrodes. For four electrodes, there were no distinct current peaks, as shown in figure 5.2a. For the rest, negative current peaks occurred around  $-0.4$  V to  $-0.5$  V (figure 5.2b). This might be due to Mo on the electrode edge taking part in the reactions. In an electrolyte with pH 7, such as PBS, Mo oxide can form around these potentials [65]. For some samples, a positive current peak was present around  $-0.2$  V and another negative

peak around 0.3 V or 0.5 V. To know precisely which reaction those peaks represent, experiments with various electrolytes with different compositions should be done.

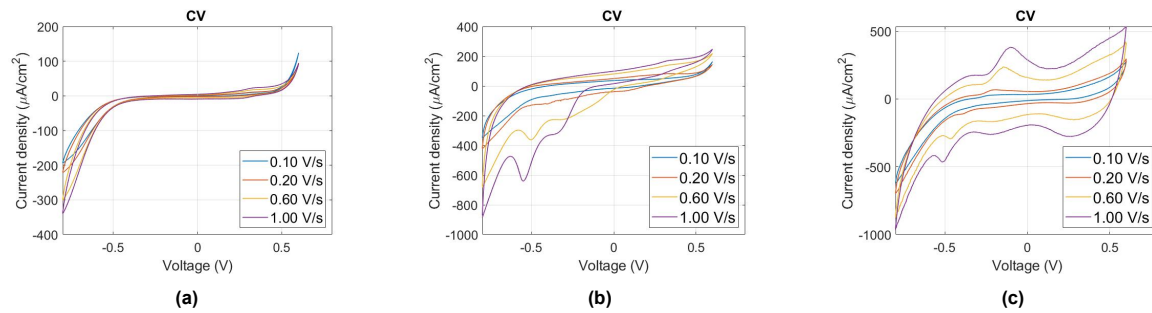


**Figure 5.2:** Various CV measurement results, where (a) no peaks occur, (b) a negative peak around -0.55 V, and (c) negative peaks around -0.5 V and 0.3 V, and a positive peak around -0.1 V

The average cathodic and total CSCs at 0.1 V/s, 0.2 V/s, 0.6 V/s, and 1.0 V/s for all the conditions are given in tables 5.2 and 5.3, respectively. The highest measured total CSCs were  $4.98 \text{ mC}/\text{cm}^2$  at 0.1 V/s,  $2.76 \text{ mC}/\text{cm}^2$  at 0.2 V/s,  $1.52 \text{ mC}/\text{cm}^2$  at 0.6 V/s, and  $1.30 \text{ mC}/\text{cm}^2$  at 1.0 V/s. The values of CSC are higher with slower sweep rate due to pore resistance and slower reactant flux to the electrode surface as explained in section 2.3. It can be seen that the SD is quite large for all the conditions. That might be due to the unknown water window. It is possible that at -0.8 V, water reduction is already happening for some samples, and thus, the CSC is overestimated. Furthermore, the different occurring peaks affect variation in the CSC. It can also be observed that electrodes with unexpected EIS behaviour have larger cathodic and total CSC for both groups, devices with only graphene and devices with Mo and graphene contact pads. Furthermore, the average CSCs are higher for the devices with Mo and graphene on the contact pad.

**Table 5.2:** The cathodic CSC

Contact pad	Behaviour	nr of samples	cathodic CSC ( $\pm$ SD) ( $\mu\text{C}/\text{cm}^2$ )			
			0,1 V/s	0,2 V/s	0.6 V/s	1.0 V/s
only graphene	capacitive	6	$1212 \pm 746$	$691 \pm 409$	$316 \pm 181$	$217 \pm 125$
	unexpected	7	$1968 \pm 588$	$1158 \pm 297$	$638 \pm 111$	$525 \pm 92$
	total	13	$1619 \pm 748$	$942 \pm 416$	$489 \pm 219$	$383 \pm 190$
Mo + graphene	capacitive	10	$2097 \pm 1093$	$1170 \pm 570$	$531 \pm 241$	$390 \pm 177$
	unexpected	4	$2853 \pm 799$	$1609 \pm 441$	$755 \pm 197$	$590 \pm 145$
	total	14	$2313 \pm 1049$	$1296 \pm 559$	$595 \pm 245$	$447 \pm 188$

Table 5.3: The total CSC

Contact pad	Behaviour	nr of samples	total CSC ( $\pm$ SD) ( $\mu\text{C}/\text{cm}^2$ )			
			0,1 V/s	0,2 V/s	0.6 V/s	1.0 V/s
only graphene	capacitive	6	1656 $\pm$ 956	921 $\pm$ 520	427 $\pm$ 248	297 $\pm$ 178
	unexpected	7	3127 $\pm$ 761	1839 $\pm$ 419	1075 $\pm$ 244	907 $\pm$ 212
	total	13	2448 $\pm$ 1120	1416 $\pm$ 654	776 $\pm$ 411	626 $\pm$ 369
Mo + graphene	capacitive	10	2782 $\pm$ 1376	1525 $\pm$ 706	729 $\pm$ 330	558 $\pm$ 265
	unexpected	4	3537 $\pm$ 967	1976 $\pm$ 524	997 $\pm$ 245	839 $\pm$ 190
	total	14	2998 $\pm$ 1286	1654 $\pm$ 673	806 $\pm$ 324	638 $\pm$ 273

### 5.1.3. Correlation analysis

The correlation between  $|Z|$  at 1 kHz and cathodic or total CSC was investigated. For the analysis, one outlier was removed ( $|Z|$  at 1 kHz = 94 830  $\Omega$ ). The scatter plots with trendlines in figure 5.3 illustrate the correlation. Considering devices with both contact types, the correlation with  $|Z|$  at 1 kHz is moderate for cathodic CSC ( $R^2 = 0.53$ ) and weak for total CSC ( $R^2 = 0.39$ ). CSC strongly correlates with  $|Z|$  at 1 kHz for the devices with Mo and graphene contact pads ( $R^2 = 0.71$  for cathodic CSC and  $R^2 = 0.75$  for total CSC). The devices with only graphene contact pads did not show correlation with  $|Z|$  at 1 kHz ( $R^2 = 0.12$  for cathodic CSC and  $R^2 = 0.04$  for total CSC).

The correlation coefficients might be affected by the large variation of  $|Z|$  at 1 kHz. The four Mo and graphene contact devices with  $|Z|$  at 1 kHz around 30 k $\Omega$  may be outliers. Removing these values would result in no correlation between CSC and  $|Z|$ . Thus, a larger sample set is required to conclude. The high impedance may be limited for the devices with only graphene contact pads, and thus, there are not many samples with high CSC and low impedance for this contact type.

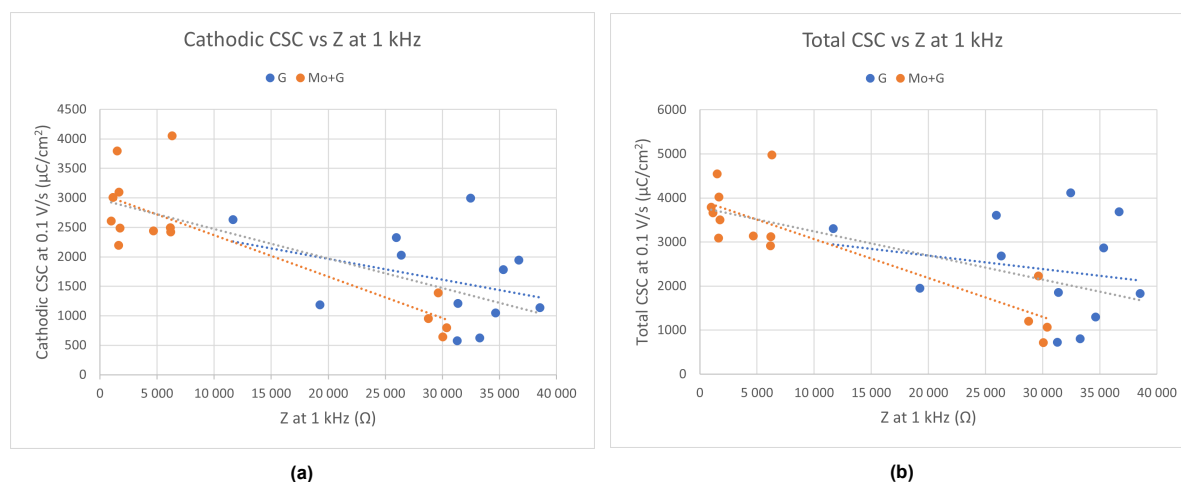


**Figure 5.3:** (a) Cathodic CSC measured at 0.1 V/s correlation with  $|Z|$  at 1kHz (b) Cathodic CSC measured at 0.1 V/s correlation with  $|Z|$  at 1kHz. The devices with only graphene on the contact pad are marked with blue (G) and devices with graphene and Mo on the contact pad are marked with orange (Mo+G). The dotted lines in blue and orange are the linear trendlines for G and Mo+G devices, respectively, and the grey dotted lines are trendlines for all the data.

Compared to other graphene electrodes reported in the literature, the electrodes presented in this work perform well. The average  $|Z|$  at 1 kHz for electrodes with Mo and graphene on the contact pad is 12 226  $\Omega$ , which is close to a graphene electrode with a much larger surface area (310 000  $\mu\text{m}^2$  with  $|Z|$  of 10 k $\Omega$  [40]) and lower than the electrodes with a smaller surface area. In terms of CSC, the

electrodes measured in this work are between the reported characteristics. The total CSC reported in the literature ( $910 \mu\text{C}/\text{cm}^2$  at 1 V/s [43]) is higher than the average CSC in this work. However, the average cathodic CSC measured in this work is much higher than what is reported in the literature ( $87.8 \mu\text{C}/\text{cm}^2$  at 1 V/s [17]). The CSC do not reach the values for Pt, Tin, or IrOx electrodes.

## 5.2. Graphene with different growth times

Electrode structures and van der Pauw structures were fabricated with graphene grown with three durations: 20 min, 40 min, and 60 min. The sheet resistances for the different graphene conditions are reported. The EIS and CV measurements for the electrodes are presented. The optical transmittances of the transferred graphene layers are shown.

### 5.2.1. Sheet resistance

Sheet resistance ( $R_s$ ) was measured on 27 van der Pauw structures per condition. There was a strong correlation between the  $R_s$  and the location on the wafer for all conditions. The structures in the wafer centre showed the lowest  $R_s$ , and the structures towards the edge showed higher  $R_s$ . This is possibly due to the central placement of the heating element in the chamber where graphene is grown. That creates a higher temperature close to the centre of the wafer, which results in thicker graphene with lower defect density. Furthermore, the average  $R_s$  was lower for the longer growth time, which was probably due to the increased thickness. The average  $R_s$  for each condition are given in the table 5.4. The variation of the  $R_s$  over the wafer was smaller for the higher growth time graphene. That could be explained by the isothermal growth process of graphene, which indicates that with the increased thickness of graphene, the growth is slower. Another explanation is the low solubility of Mo for carbon atoms. Mo will be saturated faster in the middle, and thus, thickness will not increase further. Therefore, with a longer growth time, the thickness of the graphene on the edges of the wafer becomes more similar to the thickness in the centre. The average  $R_s$  and the variations are depicted in figure 5.4. The measured  $R_s$  for each location measured can be seen in the appendix A.

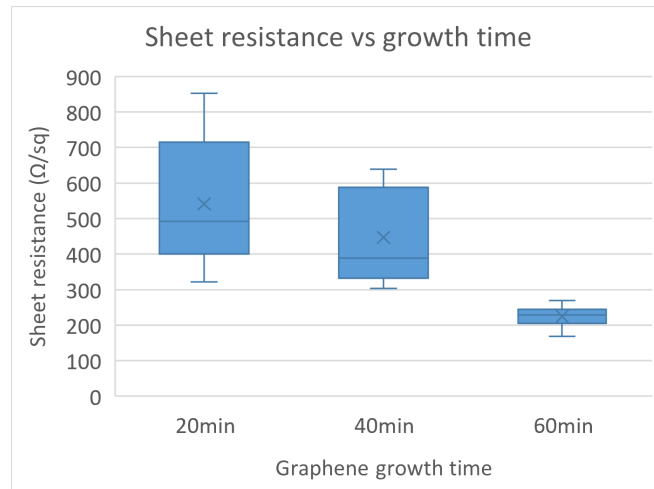


**Figure 5.4:** Sheet resistance vs graphene growth time shows lower average  $R_s$  and smaller variation for longer growth time

**Table 5.4:** Sheet resistances for different growth times

graphene growth time	average sheet resistance ( $\pm$ SD)	minimum $R_s$	maximum $R_s$
20 min	$541.05 \pm 171.12 \Omega/\text{sq}$	$321.14 \Omega/\text{sq}$	$852.13 \Omega/\text{sq}$
40 min	$447.18 \pm 126.47 \Omega/\text{sq}$	$301.89 \Omega/\text{sq}$	$639.01 \Omega/\text{sq}$
60 min	$224.92 \pm 26.25 \Omega/\text{sq}$	$168.51 \Omega/\text{sq}$	$269.49 \Omega/\text{sq}$

### 5.2.2. Electrochemical characterisation

A large number of samples was measured with the graphene grown for 20 min. Only three devices survived the fabrication process with graphene grown for 40 min and six devices with graphene grown for 60 min. Out of those, one device with 40-min-graphene and four devices with 60-min-graphene showed resistive behaviour, and therefore, were excluded from further analysis. All devices had Mo and graphene on contact pads.

The average  $|Z|$  at 1 kHz for 40-min-graphene was  $30\,885 \pm 3090 \, \Omega$  and for 60-min-graphene  $27\,065 \pm 1506 \, \Omega$ . These values are higher compared to 20-min-graphene electrodes with Mo and graphene on the contact pad. Based on the sheet resistance measurements, a decrease in impedance was expected with a longer growth time. It is possible that a poor contact between the wire and the device affected these measurements.

CSCs were higher for electrodes with 60-min-graphene than for 40-min-graphene. However, both were lower than the average CSCs for 20-min-graphene. The calculated cathodic and total CSCs are in the table 5.5

**Table 5.5:** CSC of 40 min and 60 min graphene electrodes ( $\mu C/cm^2$ )

growth time	CSC	0.1 V/s	0.2 V/s	0.6 V/s	1.0 V/s
40 min	total CSC	758.15	411.61	175.92	121.16
	cathodic CSC	688.23	375.10	158.44	107.66
40 min	total CSC	812.08	441.90	186.09	125.02
	cathodic CSC	716.63	394.84	166.03	110.74
60 min	total CSC	1 797.54	999.91	530.41	435.11
	cathodic CSC	1 274.35	698.50	355.88	284.03
60 min	total CSC	2 172.83	1 253.75	604.43	438.36
	cathodic CSC	1 716.01	987.09	464.99	331.29

### 5.2.3. Optical transmittance

Optical transmittance measurements performed on graphene grown for 20 min, 40 min, and 60 min are shown in figure 5.5. These confirm that increasing the growth time increases the thicknesses of graphene and reduces the optical transmittance. The optical transmittance at 550 nm is typically used for the calculation of graphene thickness. According to these measurements, the graphene thicknesses are  $\sim 7$ -8,  $\sim 9$  and  $\sim 11$  layers, for 20 min, 40 min, and 60 min growth times, respectively. During optogenetic stimulation, light-induced artefacts were observed by Park et al. [17] with stacked 4-layer graphene using the PMMA-transfer method described earlier. However, the artefacts were not induced using the bubbling-transfer method with monolayer graphene by Thunemann et al. [45]. It is uncertain if the artefact was induced due to the thickness or due to the polymer residues from the transfer process that lowered the transparency. Therefore, it is difficult to predict if using optogenetics with the CVD multilayer graphene electrodes used in this work would induce artefact. The graphene is thicker, but on the contrary, there are no polymer residues between the layers. Thus, light-induced artefact testing of graphene with different thicknesses would be valuable.

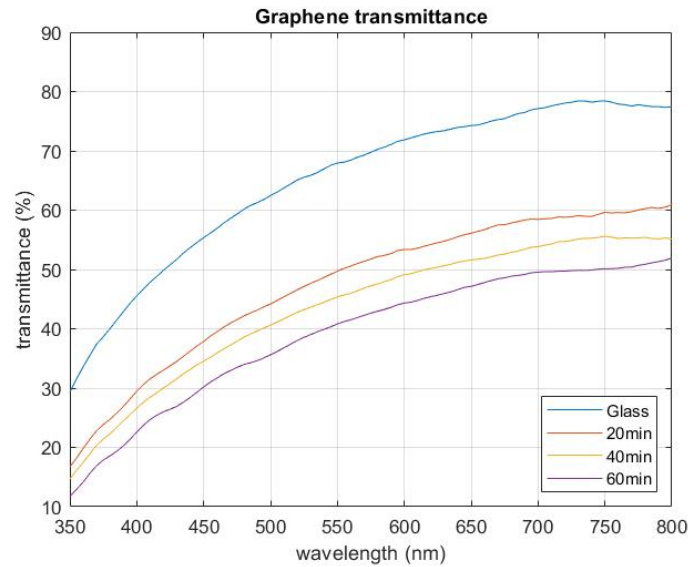


Figure 5.5: Transmittance of graphene with different growth times

Table 5.6: Optical transmittance of graphene with different growth times

Sample	Measured transmittance		Glass reduced	
	%T at 470 nm	%T at 550 nm	%T at 470 nm	%T at 550 nm
Glass	58,6	68,0		
20 min graphene	41,0	49,7	82,3	81,8
40 min graphene	37,3	45,4	78,6	77,4
60 min graphene	33,0	40,8	74,4	72,9

#### 5.2.4. Correlation analysis

Correlation between the  $R_s$ , graphene growth time and optical transmittance was investigated. The relationships are depicted in figure 5.6. The correlation coefficient between growth time and optical transmittance was  $R^2 = 1$ . The sample size was probably too small, nevertheless it shows a strong linear correlation. The  $R_s$  correlation with growth time and transmittance was also very strong ( $R^2 = 0.95$ ).

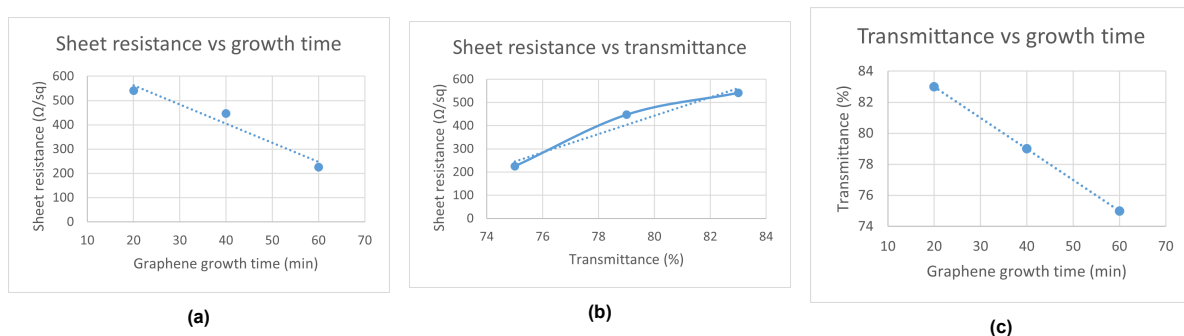


Figure 5.6: Graphs illustrating correlations between  $R_s$ , optical transmittance, and graphene growth time

The sheet resistance measured for graphene with different growth times correlated well with the transmittance. Electrochemical characterisation, however, did not follow that correlation. The impedance

of the electrodes with graphene grown for a longer period was not improved compared to 20 minutes growth time.

The CSCs were also lower than that of the 20-min graphene samples. However, 60-min graphene showed higher CSCs than the 40-min graphene electrodes.

### 5.3. Graphene electrodes with nanoparticles

In this work, graphene electrodes were decorated with Au, Pt and Au+Pt alloy NPs. The electrochemical characteristics measured before and after printing NPs are reported in this section. Furthermore, NPs were also printed on glass slides for optical transmittance measurement. These results are also presented here.

The NPs were printed with three different densities. Au NPs covered 47%, 26%, or 10% on 2 devices per condition. Pt NPs covered 47%, 22%, and 8% on two devices per condition. Au+Pt NPs covered 29%, 14% or 6% on 1 electrode per condition.

#### 5.3.1. Electrochemical impedance spectroscopy

Au NPs were printed on six samples with three different densities. The samples had a relatively high impedance before adding nanoparticles. The  $|Z|$  at 1 kHz was decreased in five cases. The most significant decrease was 82% for the highest density of Au NPs. The reduction in impedance values was greater for the higher density of NPs. However, the reduction values are quite different for the same density of NPs. The  $|Z|$  at 1 kHz measured before and after adding Au NPs are illustrated in figure 5.7. The changes in the impedance values are given in the table 5.7.

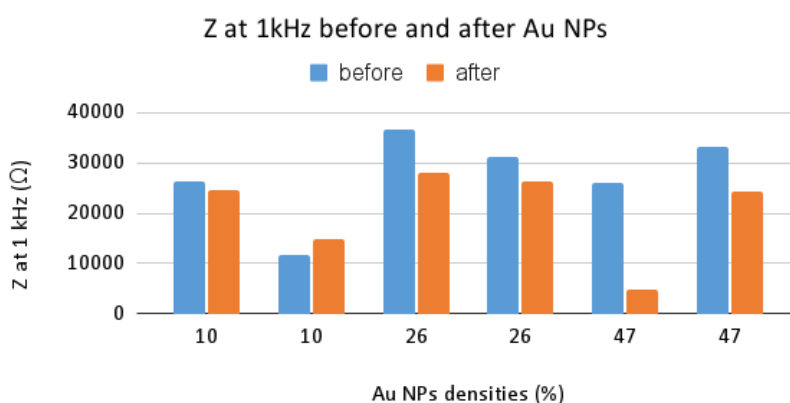


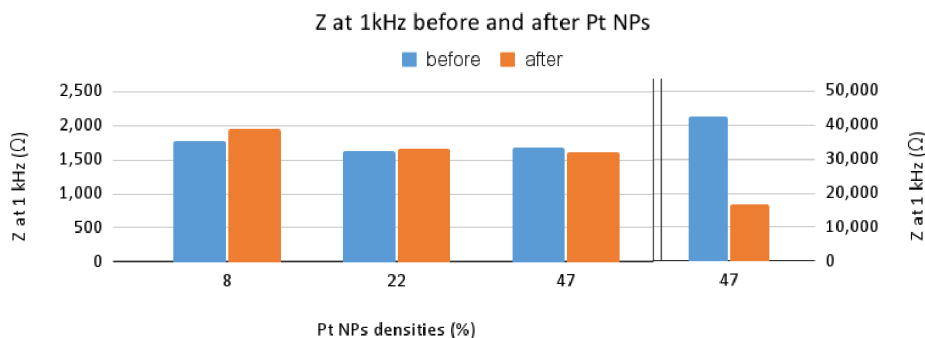
Figure 5.7: The  $|Z|$  at 1 kHz measured before and after adding AuNPs.

Table 5.7:  $|Z|$  at 1 kHz change with Au NPs

Au NPs density	$ Z $ at 1 kHz ( $\Omega$ )		change
	before	after	
10 %	26 380	24 590	-6.8 %
10 %	11 660	14 990	28.6 %
26 %	36 690	27 920	-23.9 %
26 %	31 290	26 270	-16.0 %
47 %	25 950	4 710	-81.8 %
47 %	33 270	24 380	-26.7 %

Out of the six devices where Pt NPs were printed, three had relatively high impedance and the other three, relatively low impedance. However, only 1 of the high-impedance samples survived until

the after measurement. The samples that had low impedance before Pt NPs did not show significant improvement. The electrode with the lowest density of Pt NPs showed a 10% increase in the  $|Z|$  at 1 kHz. The electrode with the highest density of Pt NPs showed a 5% decrease in the  $|Z|$  at 1 kHz. However, the device with high impedance before Pt NPs showed a 60% decrease in  $|Z|$  at 1 kHz. The impedances before and after adding Pt NPs are illustrated in figure,5.8 and the changes in  $|Z|$  at 1 kHz are given in the table 5.8.



**Figure 5.8:** The  $|Z|$  at 1 kHz measured before and after adding Pt NPs. Note that there are two y-axes.

**Table 5.8:**  $|Z|$  at 1 kHz change with Pt NPs

Pt NPs density	$ Z $ at 1 kHz ( $\Omega$ )		change
	before	after	
8 %	1 764	1 942	10.1 %
22 %	1 634	1 663	1.8 %
47 %	1 679	1 603	-4.5 %
47 %	42 440	16 810	-60.4 %

Au+Pt NPs were printed on three samples with low impedance before the NPs. An increase, rather than decrease, was seen after adding the Au+Pt NPs. The impedances before and after adding Au+Pt NPs are illustrated in figure,5.9 and the changes in  $|Z|$  at 1 kHz are given in the table 5.9.

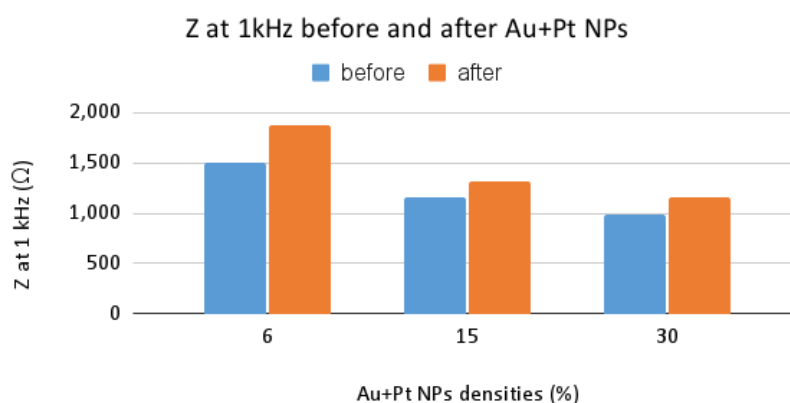


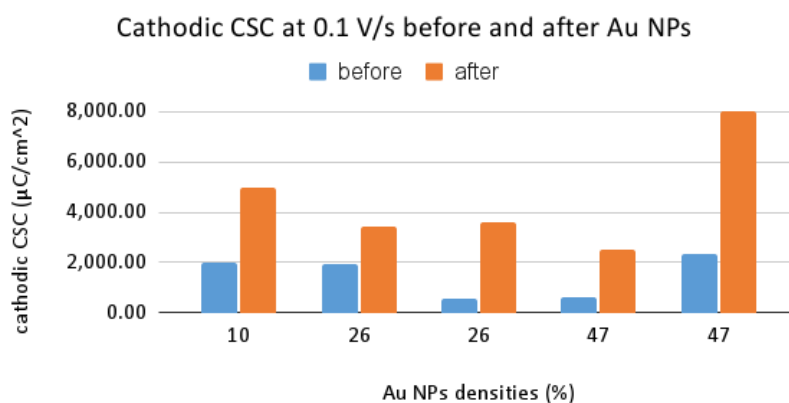
**Figure 5.9:** The  $|Z|$  at 1 kHz measured before and after adding Au+Pt NPs.

**Table 5.9:**  $|Z|$  at 1 kHz change with Au+Pt NPs

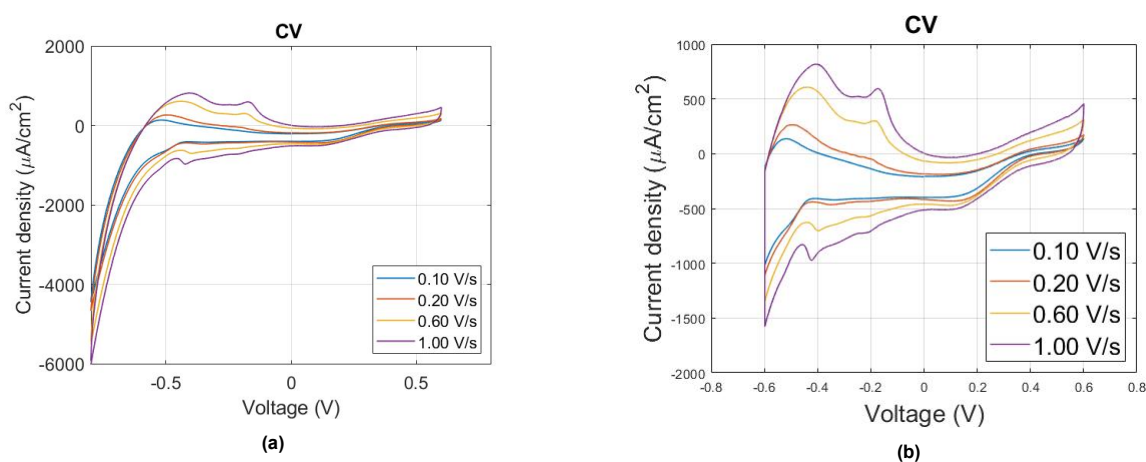
Au+Pt NPs density	$ Z $ at 1 kHz ( $\Omega$ )		change
	before	after	
6 %	1 504	1 868	24.2 %
15 %	1 151	1 322	14.9 %
30 %	993	1 153	16.1 %

### 5.3.2. Cyclic Voltammetry

With CV, changes in cathodic and total CSC were assessed. There was no linear correlation between the density of Au NPs and the change in CSC. The two devices with 26% coverage showed very different behaviour. In one case, the increase in CSC was the largest and in the other case, the smallest out of all the measurements. Cathodic CSC measured with CV at 0.1 V/s before and after adding Au NPs is shown in figure 5.12.

**Figure 5.10:** The cathodic CSC measured at 0.1 V/s before and after adding Au NPs.

After depositing Pt NPs on the electrodes, CV was performed with the potential limits -0.8 V and 0.6 V. However, the current around -0.8 V peaked as if the water reduction was already happening (figure 5.11a). This could be because adding Pt NPs may change the safe potential window for graphene. Therefore, for the calculation of CSC, the part of the water reduction was removed by setting -0.6 V as the lower potential limit (figure 5.11b).

**Figure 5.11:** (a) CV with Pt NPs shows water reduction at -0.8 V. (b) CV range reduced to -0.6 V to 0.6 V for CSC calculation

Although a smaller potential range was used for CSC calculation after NP deposition, the CSCs still showed improvement. There is a very weak correlation between the density of Pt NPs and the change in CSC. The cathodic CSC was improved more with a higher density of Pt NPs. However, the total CSC was enhanced the most with the medium density. The method of removing part of the data certainly affected these results. New measurements should be done with the same sweep range before and after adding NPs. Cathodic CSC measured with CV at 0.1 V/s before and after adding Pt NPs is shown in figure 5.12.

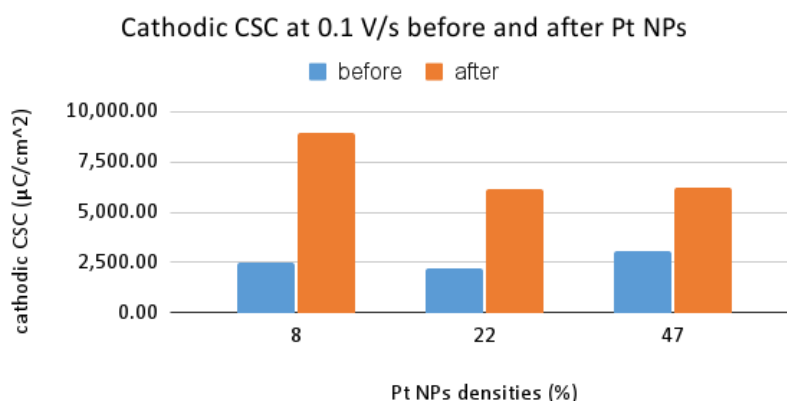


**Figure 5.12:** The cathodic CSC measured at 0.1 V/s before and after adding Pt NPs.

CV measurements after adding Au+Pt NPs showed similar behaviour to devices with Pt NPs. The water reduction potential was reached, and thus, the same method was used for the calculation of CSC.

The improvement of total CSC was more prominent for the highest density of Au+Pt NPs. Cathodic CSC was enhanced most with the medium density of Au+Pt NPs. Cathodic CSC measured with CV at 0.1 V/s before and after adding Au+Pt NPs is shown in figure 5.13.

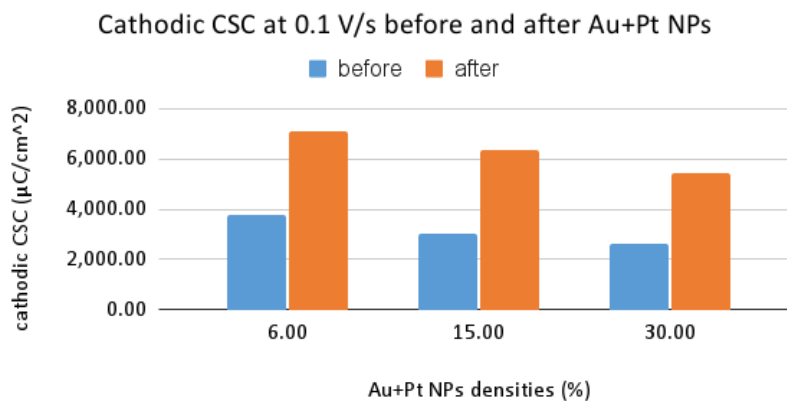


**Figure 5.13:** The cathodic CSC measured at 0.1 V/s before and after adding Au+Pt NPs.

The cathodic and total CSC results calculated for all the sweep rates before and after adding NPs are given in the appendix B.

### 5.3.3. Optical transmittance

The optical transmittance of nanoparticles on a glass slide was measured to learn how much they reduce the transmittance. In the table 5.10, optical transmittance at 470 nm is given since this wavelength is most commonly used for optogenetic stimulation and at 550 nm, which is typically used for graphene. The maximal reduction in optical transmittance was measured for Pt NPs with 47% density. The 71% transmittance would still enable neural activity imaging. For optogenetic stimulation, typically

higher than 90% optical transmittance is needed. Up to 15% NP density, less than 10% is absorbed. However, the absorbance of the graphene and substrate should be added.

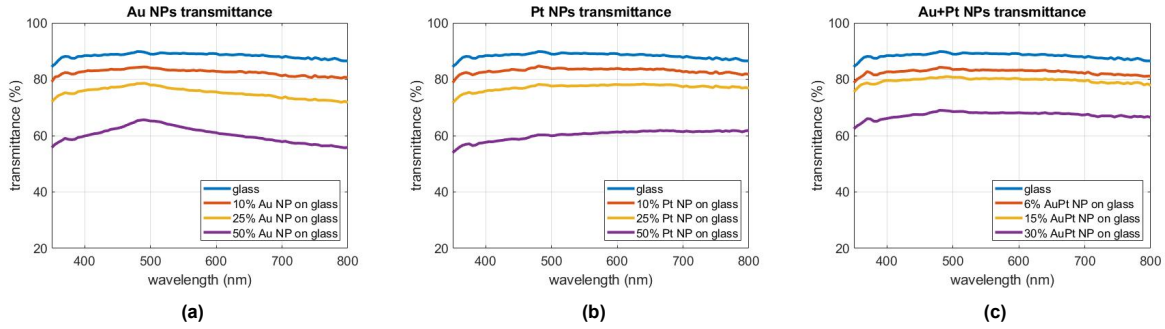


**Figure 5.14:** Optical transmittance measurements of (a) Au NPs, (b) Pt NPs, (c) Au+Pt NPs

**Table 5.10:** Optical transmittance

Sample	Measured transmittance		Glass reduced	
	%T at 470 nm	%T at 550 nm	%T at 470 nm	%T at 550 nm
Glass	89,3	89,3		
~10% Au NP on glass	84,0	83,2	94,8	93,9
~26% Au NP on glass	78,1	76,5	88,8	87,3
~47% Au NP on glass	64,3	62,9	75,0	73,7
~8% Pt NP on glass	84,0	83,7	94,8	94,5
~22% Pt NP on glass	77,6	77,7	88,3	88,4
~47% Pt NP on glass	59,8	60,8	70,5	71,5
~6% AuPt NP on glass	83,6	83,3	94,4	94,0
~15% AuPt NP on glass	80,5	80,3	91,3	91,0
~30% AuPt NP on glass	68,4	68,1	79,1	78,9

There is a correlation between the density of NPs and the reduction in  $|Z|$  at 1 kHz. Au NPs showed the largest decrease in impedance (82%). However, using high-impedance samples with Au+Pt NPs might change that conclusion. The cathodic CSC showed an improvement after adding NPs for all the conditions. Total CSCs were improved in 42 cases out of 44. The highest total CSCs were measured for samples with 22% and 47% Pt NPs coverage:  $9.40 \text{ mC}/\text{cm}^2$  at 0.1 V/s,  $4.90 \text{ mC}/\text{cm}^2$  at 0.2 V/s,  $2.24 \text{ mC}/\text{cm}^2$  at 0.6 V/s, and  $1.79 \text{ mC}/\text{cm}^2$  at 1.0 v/s. There seems to be a weak correlation between the density of NPs and the improvement in CSC. However, only one or two devices were measured per condition. Thus, measurements on a more extensive sample set would be needed to study the correlation.

Optical transmittance measurements correlate well with the densities of NPs. With 47% coverage, only 30% of the light is absorbed. Therefore, NPs should not affect neural activity imaging. Since the nanoparticles are metal NPs, light-induced artefact testing should be performed to investigate the viability of graphene electrodes with metal nanoparticles for optogenetics application.

Graphene electrodes with Pt NPs in literature have achieved a 99% reduction was achieved while maintaining higher than 90% optical transmittance. In this work, while maintaining high transmittance, only a 7% reduction in impedance was observed with 10% coverage of Au NPs. The biggest improvement in impedance (82%) occurred with 47% coverage with Au NPs, but the optical transmittance was lowered by 30%.

## 5.4. Graphene electrodes doped with nitric acid

Nitric acid doping was done with 69.99%  $HNO_3$  for two devices and 35%  $HNO_3$  for two devices. The electrodes exhibited capacitive behaviour with an average  $|Z|$  at 1 kHz of  $29700 \pm 700 \Omega$  before the doping (figure 5.15a). However, after the doping, only one remained with capacitive behaviour.

The EIS result for an electrode with 69.99% nitric acid doping is shown in figure 5.15b. The  $|Z|$  at 1 kHz has reduced to  $7412 \Omega$ . However, the phase suggests that this result is not reliable. This odd behaviour may be due to the damage to the insulating photoresist layer. However, the visual inspection did not reveal the damage. The behaviour of the second device with 69.99% nitric acid doping remained capacitive, and the  $|Z|$  at 1 kHz increased to  $33840 \Omega$ .

Of the devices doped with 35%, one exhibited resistive behaviour with  $|Z|$  at 1 kHz over  $1M\Omega$ . The EIS result for the other device is depicted in figure 5.15c. The  $|Z|$  at 1 kHz has also increased to  $34540 \Omega$ .

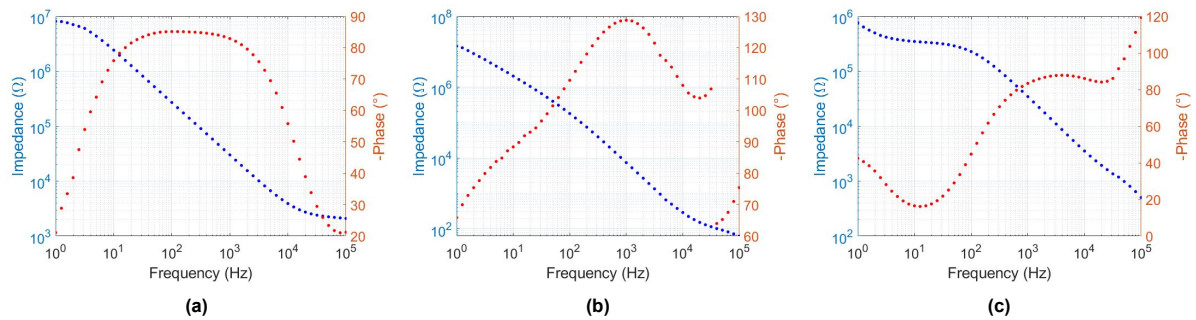


**Figure 5.15:** EIS measurements results (a) before doping, (b) after 69.99% nitric acid doping, (c) after 35% nitric acid doping

The electrodes doped with 69.99% nitric acid both showed an increase in the CSCs. The largest increase after 69.99% nitric acid doping was 64% for cathodic CSC at 0.1 V/s. Out of the devices with 35% nitric acid doping, the electrode with resistive showed a decrease in CSCs, and the other electrode an increase. Cathodic CSC at 0.1 V/s showed a higher increase of 66% after 35% nitric acid doping. The differences between cathodic CSC at 0.1 V/s can be seen in figure 5.16. The CSC values of all before and after measurements are given in the appendix B.

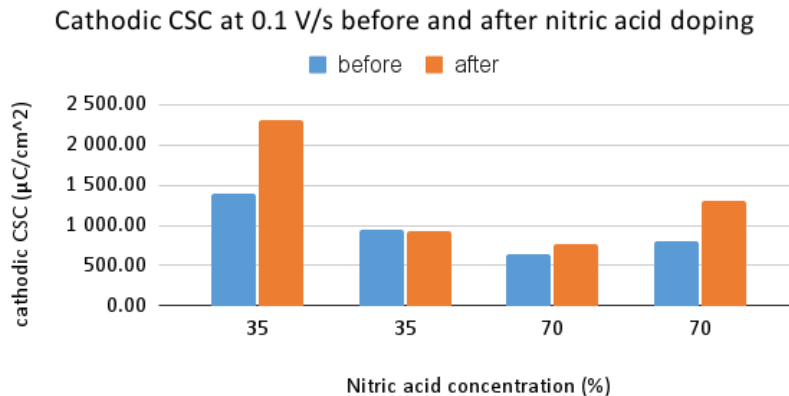


**Figure 5.16:** Cathodic CSC at 0.1 V/s before and after nitric acid doping.

Based on these measurements, it can be concluded that nitric acid doping does not improve the impedance of multilayer graphene electrodes. CSC, however, can be improved up to 66% for 0.1 V/s.

# 6

## Conclusions

Neural electrode design is moving towards flexible forms to reduce tissue damage and to provide long term stability. Transparent electrodes are being developed to combine electrical and optical modalities into one device for better spatiotemporal resolution. For this application, transparent and flexible conductive materials are needed. Graphene has shown a lot of potential as an electrode material. However, the impedance, charge storage capacity and charge injection capacity do not reach the levels of conventional materials such as platinum, TiN, and IrOx.

To improve the electrical characteristics of graphene, 3 methods were found in the literature that could be compatible with the transparent and flexible device. These methods include stacking multiple layers of graphene or growing a thicker layer of graphene, adding nanostructures on the surface of the electrode, and chemical doping.

In this work, graphene electrodes were fabricated and characterised. Compared to other graphene electrodes reported in the literature, the electrodes presented in this work perform well in terms of impedance and CSC. The minimum measured impedance at 1 kHz was  $993 \Omega$  which is better than reported in the literature. The highest measured total CSCs were  $4.98 \text{ mC/cm}^2$  at 0.1 V/s,  $2.76 \text{ mC/cm}^2$  at 0.2 V/s,  $1.52 \text{ mC/cm}^2$  at 0.6 V/s, and  $1.30 \text{ mC/cm}^2$  at 1.0 V/s. However, these might be overestimated since the water window for graphene is not known.

Three methods were used in this work to improve the electrical characteristics of graphene electrodes. Graphene was grown for 20 min, 40 min, and 60 min to achieve graphene with different thickness. Gold, platinum, and gold-platinum alloy nanoparticles were printed on the electrode. Nitric acid doping of graphene was performed with 69.99% and 35% nitric acid. Electrochemical impedance spectroscopy, cyclic voltammetry, 4-point probe measurements, and optical transmittance measurements were used to assess the performance of the electrodes.

The sheet resistance of graphene with different growth times correlated well with the transmittance. The average sheet resistance was lower for graphene grown with a longer growth time. However, the impedance of the electrodes with graphene with different thicknesses did not correlate with the growth time. The graphene grown for 20 minutes exhibited the lowest impedance and highest CSC. The 40-minute graphene showed the highest impedance and lowest CSC. These results may be affected by the poor contact between the wire and the device.

There is a correlation between the density of nanoparticles and the reduction in Z at 1 kHz for devices with gold nanoparticles. Gold nanoparticles showed the largest decrease in impedance (82%) and the largest increase in the charge storage capacity (529%). However, the electrodes had different impedances and CSCs before the nanoparticle deposition. Impedance was not improved for all samples, but the cathodic charge storage capacity improved after adding nanoparticles for all the conditions. The highest total CSCs were measured for samples with 22% and 47% Pt NPs coverage:  $9.40 \text{ mC/cm}^2$  at 0.1 V/s,  $4.90 \text{ mC/cm}^2$  at 0.2 V/s,  $2.24 \text{ mC/cm}^2$  at 0.6 V/s, and  $1.79 \text{ mC/cm}^2$  at 1.0 v/s. These values are higher than what has been reported for Tin electrodes ( $4.82 \text{ mC/cm}^2$  at 0.1 V/s), but still significantly lower than IrOx ( $21 \text{ mC/cm}^2$  at 0.1 V/s) [44].

A small number of devices were measured per condition. Thus, measurements on a more extensive sample set would be needed to study the correlations between nanoparticle densities and electrochemical characteristics.

Optical transmittance measurements correlate well with the densities of nanoparticles. With 47% coverage, only 30% of the light is absorbed. Therefore, having nanoparticles on the electrode should not affect neural activity imaging. Since the nanoparticles are metal, light-induced artefact testing should be performed to investigate the viability of graphene electrodes with metal nanoparticles for optogenetics application.

While maintaining high transmittance ( $< 90\%$ ), only a 7% reduction in impedance was observed with 10% coverage of Au NPs. The biggest improvement in impedance (82%) occurred with 47% coverage with Au NPs, but the optical transmittance was lowered by 30%.

Nitric acid doping did not improve the impedance of the graphene electrodes. Charge storage capacity, however, was improved up to 66% (0.1 V/s).

## 6.1. Future recommendations

During this project, it was observed that good contact between the wire and the device is crucial. Thus, to characterise the electrodes more accurately, a non-manual way of connecting wire to the graphene structure should be opted. Furthermore, other types of conductive adhesives could be tested with graphene.

Since graphene is permeable to liquid, the electrolyte also goes under graphene during electrochemical characterisation. The electrode design used in this work allows for a small contact area also with Mo. That can lead to variations in EIS and CV results. Therefore, an electrode design where Mo is completely etched should be developed for electrical characterisation.

As mentioned in the literature study chapter, the water window for graphene is not known. Therefore, the safe charge injection limits for graphene should be investigated. Furthermore, Pt NPs seemed to affect the water window. Thus, the investigation should also be done for electrodes after introducing the improvement methods.

Adding metal nanoparticles to the surface of the electrode has shown to improve the electrical characteristics of graphene neural electrode. Nevertheless, further investigation is needed to find the exact correlation between the improvement methods and the performance of the electrode.

Measuring voltage transients is a relevant characterisation method for stimulation electrodes. Even more so than cyclic voltammetry, since square wave pulses are used, which are actually also used to stimulate the tissue. Unfortunately, due to the unavailability of suitable equipment that could create a square wave with low amplitude and short pulse width, voltage transients could not be measured in this work. In future work, this characterisation should be performed on the graphene electrodes to assess their suitability for stimulation. Furthermore, the improvement methods could be characterised further with voltage transients measurement to investigate the performance of the safe charge injection capabilities.

Stability is an essential property of an implantable device. Therefore, stability testing should be done for pristine graphene electrodes and improved graphene electrodes. It is not known how strongly the nanoparticles are adhering to the graphene. Loose nanoparticles in the body can be dangerous. Thus it is important to investigate the stability. Stability testing could include performing several hundred cycles of CV or thousands of cycles of stimulation pulses and assessing the electrode properties' change. Long-term soaking tests in saline or an ultrasonic bath could also give valuable information about the stability.

Furthermore, since the final implant structure is flexible, the electrical measurements should also be performed under mechanical strain. The properties can change under mechanical strain. Thus these tests could give information about the graphene electrodes as a flexible material and the suitability of the improvement methods for a flexible implant.

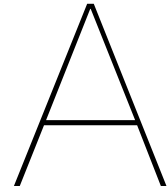
# References

- [1] Anoop C Patil and Nitish V Thakor. "Implantable neurotechnologies: a review of micro- and nano-electrodes for neural recording". In: *Medical & biological engineering & computing* 54.1 (2016), pp. 23–44.
- [2] Geon Hwee Kim et al. "Recent progress on microelectrodes in neural interfaces". In: *Materials* 11.10 (2018), p. 1995.
- [3] Christian Boehler et al. "Tutorial: guidelines for standardized performance tests for electrodes intended for neural interfaces and bioelectronics". In: *Nature Protocols* 15.11 (2020), pp. 3557–3578.
- [4] Kostas Kostarelos et al. "Graphene in the design and engineering of next-generation neural interfaces". In: *Advanced Materials* 29.42 (2017), p. 1700909.
- [5] The LibreTexts. *Neurophysiology*. Accessed on: March 22, 2021. [Online]. Available: [https://med.libretexts.org/Bookshelves/Anatomy\\_and\\_Physiology/Book:\\_Anatomy\\_and\\_Physiology\\_\(Boundless\)/10:\\_Overview\\_of\\_the\\_Nervous\\_System/10.5:\\_Neurophysiology](https://med.libretexts.org/Bookshelves/Anatomy_and_Physiology/Book:_Anatomy_and_Physiology_(Boundless)/10:_Overview_of_the_Nervous_System/10.5:_Neurophysiology).
- [6] Rich Vogel. *Understanding anodal and cathodal stimulation*. Accessed on: March 20, 2021. [Online]. Available: <https://www.asnm.org/blogpost/1635804/290597/Understanding-Anodal-and-Cathodal-Stimulation>.
- [7] Akash Guru et al. "Making sense of optogenetics". In: *International Journal of Neuropsychopharmacology* 18.11 (2015), pyv079.
- [8] Ofer Yizhar and Antoine Adamantidis. "Cell type-specific targeting strategies for optogenetics". In: *Optogenetics: a roadmap*. Springer, 2018, pp. 25–42.
- [9] Karl Deisseroth. "Optogenetics". In: *Nature methods* 8.1 (2011), pp. 26–29.
- [10] Christine Grienberger and Arthur Konnerth. "Imaging calcium in neurons". In: *Neuron* 73.5 (2012), pp. 862–885.
- [11] Guosong Hong and Charles M Lieber. "Novel electrode technologies for neural recordings". In: *Nature Reviews Neuroscience* 20.6 (2019), pp. 330–345.
- [12] Kyung Jin Seo et al. "Transparent electrophysiology microelectrodes and interconnects from metal nanomesh". In: *ACS nano* 11.4 (2017), pp. 4365–4372.
- [13] Dong-Wook Park et al. "Fabrication and utility of a transparent graphene neural electrode array for electrophysiology, in vivo imaging, and optogenetics". In: *Nature protocols* 11.11 (2016), pp. 2201–2222.
- [14] Stuart F Cogan. "Neural stimulation and recording electrodes". In: *Annu. Rev. Biomed. Eng.* 10 (2008), pp. 275–309.
- [15] Hyunwoo Yuk, Baoyang Lu, and Xuanhe Zhao. "Hydrogel bioelectronics". In: *Chemical Society Reviews* 48.6 (2019), pp. 1642–1667.
- [16] Yichen Lu, Xin Liu, and Duygu Kuzum. "Graphene-based neurotechnologies for advanced neural interfaces". In: *Current Opinion in Biomedical Engineering* 6 (2018), pp. 138–147.
- [17] Dong-Wook Park et al. "Electrical neural stimulation and simultaneous in vivo monitoring with transparent graphene electrode arrays implanted in GCaMP6f mice". In: *ACS nano* 12.1 (2018), pp. 148–157.
- [18] Yan-Gang Bi et al. "Ultrathin Metal Films as the Transparent Electrode in ITO-Free Organic Optoelectronic Devices". In: *Advanced Optical Materials* 7.6 (2019), p. 1800778.
- [19] Sang Min Won et al. "Recent advances in materials, devices, and systems for neural interfaces". In: *Advanced Materials* 30.30 (2018), p. 1800534.

- [20] Juergen Biener et al. "Advanced carbon aerogels for energy applications". In: *Energy & Environmental Science* 4.3 (2011), pp. 656–667.
- [21] Daniel R Merrill, Marom Bikson, and John GR Jefferys. "Electrical stimulation of excitable tissue: design of efficacious and safe protocols". In: *Journal of neuroscience methods* 141.2 (2005), pp. 171–198.
- [22] Giuseppe Schiavone et al. "Guidelines to Study and Develop Soft Electrode Systems for Neural Stimulation". In: *Neuron* 108.2 (2020), pp. 238–258.
- [23] Junqiao Lee. "Electrochemical sensing of oxygen gas in ionic liquids on screen printed electrodes". PhD thesis. Curtin University, 2014.
- [24] Allen J Bard, Larry R Faulkner, et al. "Fundamentals and applications". In: *Electrochemical Methods* 2.482 (2001), pp. 580–632.
- [25] Ana Cissal et al. "Application of a Novel Measurement Setup for Characterization of Graphene Microelectrodes and a Comparative Study of Variables Influencing Charge Injection Limits of Implantable Microelectrodes". In: *Sensors* 19.12 (2019), p. 2725.
- [26] Yichen Lu et al. "Flexible neural electrode array based on porous graphene for cortical microstimulation and sensing". In: *Scientific reports* 6.1 (2016), pp. 1–9.
- [27] Michael B Heaney. "Electrical conductivity and resistivity". In: *Electrical measurement, signal processing, and displays* 7.1 (2003).
- [28] Douglas A Skoog, F James Holler, and Stanley R Crouch. *Principles of instrumental analysis*. Cengage learning, 2017.
- [29] Yichen Lu et al. "Ultralow impedance graphene microelectrodes with high optical transparency for simultaneous deep two-photon imaging in transgenic mice". In: *Advanced Functional Materials* 28.31 (2018), p. 1800002.
- [30] Samira Naghdi et al. "Atmospheric chemical vapor deposition of graphene on molybdenum foil at different growth temperatures". In: *Carbon letters* 18 (2016), pp. 37–42.
- [31] Mingyu Sang et al. "Electronic and thermal properties of graphene and recent advances in graphene based electronics applications". In: *Nanomaterials* 9.3 (2019), p. 374.
- [32] Dimitrios Bitounis et al. "Prospects and challenges of graphene in biomedical applications". In: *Advanced Materials* 25.16 (2013), pp. 2258–2268.
- [33] Zhongfan Liu et al. "CVD synthesis of graphene". In: *Thermal transport in carbon-based nanomaterials*. Elsevier, 2017, pp. 19–56.
- [34] Fatemeh Parnianchi et al. "Combination of graphene and graphene oxide with metal and metal oxide nanoparticles in fabrication of electrochemical enzymatic biosensors". In: *International Nano Letters* 8.4 (2018), pp. 229–239.
- [35] Yi Zhang, Luyao Zhang, and Chongwu Zhou. "Review of chemical vapor deposition of graphene and related applications". In: *Accounts of chemical research* 46.10 (2013), pp. 2329–2339.
- [36] Choon-Ming Seah, Siang-Piao Chai, and Abdul Rahman Mohamed. "Mechanisms of graphene growth by chemical vapour deposition on transition metals". In: *Carbon* 70 (2014), pp. 1–21.
- [37] Andrea Cabrero-Vilatela et al. "Towards a general growth model for graphene CVD on transition metal catalysts". In: *Nanoscale* 8.4 (2016), pp. 2149–2158.
- [38] S Vollebregt et al. "A transfer-free wafer-scale CVD graphene fabrication process for MEMS/NEMS sensors". In: *2016 IEEE 29th International Conference on Micro Electro Mechanical Systems (MEMS)*. IEEE, 2016, pp. 17–20.
- [39] Daniel Wolverson. "Raman spectroscopy". In: *Characterization of Semiconductor Heterostructures and Nanostructures*. Elsevier, 2008, pp. 249–288.
- [40] Berit Koerbitzer et al. "Graphene electrodes for stimulation of neuronal cells". In: *2D Materials* 3.2 (2016), p. 024004.
- [41] Subramaniam Venkatraman et al. "In vitro and in vivo evaluation of PEDOT microelectrodes for neural stimulation and recording". In: *IEEE Transactions on Neural Systems and Rehabilitation Engineering* 19.3 (2011), pp. 307–316.

- [42] Rylie A Green et al. "Variation in performance of platinum electrodes with size and surface roughness". In: *Sensors and Materials* 24.4 (2012), pp. 165–180.
- [43] Berit Körbitzer et al. "Electrochemical characterization of graphene microelectrodes for biological applications". In: *ChemNanoMat* 5.4 (2019), pp. 427–435.
- [44] James D Weiland, David J Anderson, and Mark S Humayun. "In vitro electrical properties for iridium oxide versus titanium nitride stimulating electrodes". In: *IEEE transactions on biomedical engineering* 49.12 (2002), pp. 1574–1579.
- [45] Martin Thunemann et al. "Deep 2-photon imaging and artifact-free optogenetics through transparent graphene microelectrode arrays". In: *Nature communications* 9.1 (2018), pp. 1–12.
- [46] Xiaowei Du et al. "Graphene microelectrode arrays for neural activity detection". In: *Journal of biological physics* 41.4 (2015), pp. 339–347.
- [47] Xin Liu et al. "A compact closed-loop optogenetics system based on artifact-free transparent graphene electrodes". In: *Frontiers in neuroscience* 12 (2018), p. 132.
- [48] Dong-Wook Park et al. "Graphene-based carbon-layered electrode array technology for neural imaging and optogenetic applications". In: *Nature communications* 5.1 (2014), pp. 1–11.
- [49] Seunghyun Lee et al. "Homogeneous bilayer graphene film based flexible transparent conductor". In: *Nanoscale* 4.2 (2012), pp. 639–644.
- [50] Amal Kasry et al. "Chemical doping of large-area stacked graphene films for use as transparent, conducting electrodes". In: *ACS nano* 4.7 (2010), pp. 3839–3844.
- [51] Jong Sik Oh, Kyong Nam Kim, and Geun Young Yeom. "Graphene doping methods and device applications". In: *Journal of nanoscience and nanotechnology* 14.2 (2014), pp. 1120–1133.
- [52] Lorenzo D'Arzié et al. "Stable, efficient p-type doping of graphene by nitric acid". In: *RSC advances* 6.114 (2016), pp. 113185–113192.
- [53] Duyoung Choi et al. "Unusually high optical transparency in hexagonal nanopatterned graphene with enhanced conductivity by chemical doping". In: *Small* 11.26 (2015), pp. 3143–3152.
- [54] Duygu Kuzum et al. "Transparent and flexible low noise graphene electrodes for simultaneous electrophysiology and neuroimaging". In: *Nature communications* 5.1 (2014), pp. 1–10.
- [55] Sahil Kumar Rastogi et al. "Graphene microelectrode arrays for electrical and optical measurements of human stem cell-derived cardiomyocytes". In: *Cellular and molecular bioengineering* 11.5 (2018), pp. 407–418.
- [56] Ibrahim Khan, Khalid Saeed, and Idrees Khan. "Nanoparticles: Properties, applications and toxicities". In: *Arabian journal of chemistry* 12.7 (2019), pp. 908–931.
- [57] Nanowerk. *Nanoparticle production – How nanoparticles are made*. Accessed on: September 8, 2021. [Online]. Available: [https://www.nanowerk.com/how\\_nanoparticles\\_are\\_made.php#:~:text=Nanoparticles%20are%20created%20from%20the,takes%20place%20via%20homogeneous%20nucleation](https://www.nanowerk.com/how_nanoparticles_are_made.php#:~:text=Nanoparticles%20are%20created%20from%20the,takes%20place%20via%20homogeneous%20nucleation).
- [58] Domenica Tonelli, Erika Scavetta, and Isacco Gualandi. "Electrochemical deposition of nanomaterials for electrochemical sensing". In: *Sensors* 19.5 (2019), p. 1186.
- [59] Andreas Schmidt-Ott. *Spark Ablation: Building Blocks for Nanotechnology*. CRC Press, 2019.
- [60] Fethullah Gunes et al. "Layer-by-layer doping of few-layer graphene film". In: *ACS nano* 4.8 (2010), pp. 4595–4600.
- [61] Andrada Velea. "Flexible Graphene-Based Passive and Active Spinal Cord Implants". In: (2019).
- [62] Gandhika K Wardhana et al. "Towards an Active Graphene-PDMS Implant". In: *7th Dutch Bio-Medical Engineering Conference*. 2019.
- [63] Zongya Zhao et al. "In vivo neural recording and electrochemical performance of microelectrode arrays modified by rough-surfaced AuPt alloy nanoparticles with nanoporosity". In: *Sensors* 16.11 (2016), p. 1851.

- [64] VSPARTICLE. *G1 output estimator*. Accessed on: March 8, 2021. [Online]. Available: [https://vsparticle.com/products/vsp-g1-nanoparticle-generator/output-estimator?tx\\_vspg1outputestimator\\_fp001%5Bcontroller%5D=AblationRate&cHash=279fc29a9d4f6ca51d0c1af5cda9b1fa](https://vsparticle.com/products/vsp-g1-nanoparticle-generator/output-estimator?tx_vspg1outputestimator_fp001%5Bcontroller%5D=AblationRate&cHash=279fc29a9d4f6ca51d0c1af5cda9b1fa).
- [65] Viswanathan S Saji and Chi-Woo Lee. "Molybdenum, molybdenum oxides, and their electrochemistry". In: *ChemSusChem* 5.7 (2012), pp. 1146–1161.



## Measured sheet resistances for each location

Sheet resistances were measured on one quarter of a wafer. The structures are shown in figure A.1. The sheet resistances in  $\Omega/sq$  according to the location are given in figures A.2, A.3, A.4 for graphene grown for 20 min, 40 min, and 60 min, respectively.

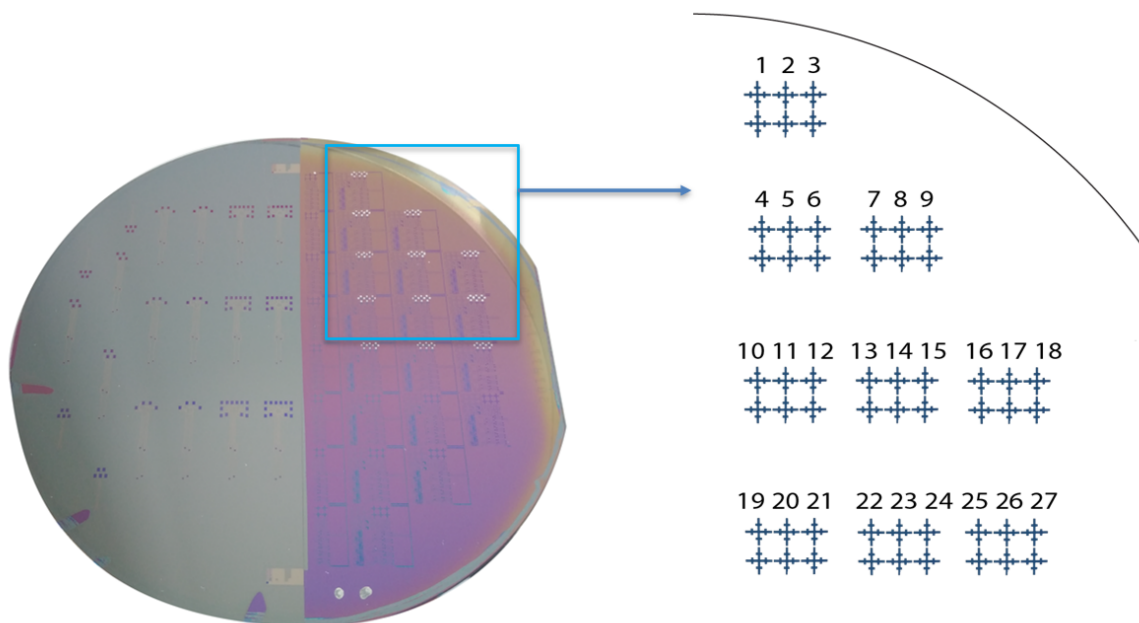


**Figure A.1:** Wafer with van der Pauw structures. Structures 1 to 27 were used for sheet resistance measurements.



# B

## Measured charge storage capacities before and after adding nanoparticles

In the table B.1, all measurement results for cathodic and total CSC with 0.1 V/s, 0.2 V/s, 0.6 V/s, 1.0 V/s are given. The measurements were done before and after adding nanoparticles to the electrode. Furthermore, the difference in the CSC between before and after is calculated and reported in the table.

**Table B.1:** CSC before and after adding nanoparticles ( $\mu C/cm^2$ )

CSC	Before				Addition	After				Change			
	0.1 V/s	0.2 V/s	0.6 V/s	1.0 V/s		0.1 V/s	0.2 V/s	0.6 V/s	1.0 V/s	0.1 V/s	0.2 V/s	0.6 V/s	1.0 V/s
total CSC	806.74	414.65	169.63	112.58	<b>47% Au NPs</b>	2 591.99	1 540.00	671.88	469.30	221.3 %	271.4 %	296.1 %	316.8 %
cathodic CSC	626.37	338.89	140.82	92.86	<b>47% Au NPs</b>	2 499.05	1 456.72	599.56	403.15	299.0 %	329.9 %	325.8 %	334.2 %
total CSC	3 610.28	1 913.48	933.47	752.19	<b>47% Au NPs</b>	8 547.06	4 757.38	2 124.57	1 570.27	410.6 %	431.7 %	409.9 %	397.1 %
cathodic CSC	2 327.12	1 279.66	605.67	471.16	<b>47% Au NPs</b>	7 987.86	4 392.56	1 836.02	1 288.50	529.1 %	521.7 %	483.7 %	465.9 %
total CSC	720.91	390.01	163.16	111.21	<b>26% Au NPs</b>	3 681.14	2 073.67	831.95	552.85	136.7 %	148.6 %	127.6 %	108.8 %
cathodic CSC	575.80	326.37	137.21	92.80	<b>26% Au NPs</b>	3 622.26	2 028.96	800.94	525.13	243.3 %	243.3 %	203.1 %	173.5 %
total CSC	3 689.73	2 361.71	1 522.65	1 296.23	<b>26% Au NPs</b>	4 084.53	2 455.26	1 380.31	1 147.97	10.7 %	4.0 %	- 9.3 %	- 11.4 %
cathodic CSC	1 943.49	1 263.42	790.56	683.71	<b>26% Au NPs</b>	3 405.83	1 982.01	995.97	777.96	75.2 %	56.9 %	26.0 %	13.8 %
total CSC	2 684.47	1 581.31	901.26	780.32	<b>10% Au NPs</b>	5 465.39	3 172.72	1 617.12	1 286.10	103.6 %	100.6 %	79.4 %	64.8 %
cathodic CSC	2 026.07	1 184.18	609.92	494.59	<b>10% Au NPs</b>	4 951.83	2 829.95	1 301.30	959.88	144.4 %	139.0 %	113.4 %	94.1 %
total CSC	3 789.75	1 865.55	869.03	654.62	<b>30% Au+Pt NPs</b>	7 136.56	3 909.44	1 909.91	1 516.06	88.3 %	109.6 %	119.8 %	131.6 %
cathodic CSC	2 604.49	1 426.95	645.09	467.79	<b>30% Au+Pt NPs</b>	5 440.25	2 916.36	1 184.23	861.29	108.9 %	104.4 %	83.6 %	84.1 %
total CSC	3 659.11	1 961.32	922.42	710.16	<b>15% Au+Pt NPs</b>	6 635.04	3 997.45	1 933.68	1 459.22	81.3 %	103.8 %	109.6 %	105.5 %
cathodic CSC	3 007.69	1 627.00	714.33	521.81	<b>15% Au+Pt NPs</b>	6 337.39	3 549.41	1 527.25	1 091.41	110.7 %	118.2 %	113.8 %	109.2 %
total CSC	4 548.21	2 459.55	1 109.31	828.86	<b>6% Au+Pt NPs</b>	7 047.30	4 058.63	1 882.55	1 370.10	54.9 %	65.0 %	69.7 %	65.3 %
cathodic CSC	3 796.75	2 043.95	872.37	619.58	<b>6% Au+Pt NPs</b>	7 090.94	3 774.59	1 536.18	1 037.29	86.8 %	84.7 %	76.1 %	67.4 %
total CSC	4 019.54	2 170.01	963.04	711.68	<b>47% Pt NPs</b>	9 395.11	4 795.51	2 018.69	1 786.00	133.7 %	121.0 %	109.6 %	151.0 %
cathodic CSC	3 098.23	1 691.65	726.39	518.69	<b>47% Pt NPs</b>	8 916.45	4 592.25	1 835.38	1 394.61	187.8 %	171.5 %	152.7 %	168.9 %
total CSC	3 089.46	1 782.69	993.32	824.83	<b>22% Pt NPs</b>	7 686.84	4 903.51	2 239.49	1 774.52	148.8 %	175.1 %	125.5 %	115.1 %
cathodic CSC	2 194.63	1 250.64	631.92	496.80	<b>22% Pt NPs</b>	6 139.70	3 588.46	1 353.07	988.93	179.8 %	186.9 %	114.1 %	99.1 %
total CSC	3 499.86	1 909.66	879.94	668.20	<b>8% Pt NPs</b>	6 595.24	3 822.94	1 785.14	1 357.48	88.4 %	100.2 %	102.9 %	103.2 %
cathodic CSC	2 487.37	1 387.54	616.75	450.60	<b>8% Pt NPs</b>	6 240.54	3 404.02	1 380.99	995.95	150.9 %	145.3 %	123.9 %	121.0 %

**Table B.2:** CSC before and after nitric acid doping ( $\mu C/cm^2$ )

CSC	Before				Treatment	After				Change			
	0.1 V/s	0.2 V/s	0.6 V/s	1.0 V/s		0.1 V/s	0.2 V/s	0.6 V/s	1.0 V/s	0.1 V/s	0.2 V/s	0.6 V/s	1.0 V/s
total CSC	713.46	403.38	171.27	117.71	<b>69.99% HNO<sub>3</sub></b>	805.39	451.15	194.07	136.71	12.89 %	11.84 %	13.31 %	16.14 %
cathodic CSC	640.93	364.60	154.34	105.23	<b>69.99% HNO<sub>3</sub></b>	768.57	428.61	181.09	125.68	19.92 %	17.55 %	17.33 %	19.43 %
total CSC	1 070.13	666.94	319.69	218.60	<b>69.99% HNO<sub>3</sub></b>	1 451.01	867.08	387.87	268.70	35.59 %	30.01 %	21.33 %	22.92 %
cathodic CSC	797.72	500.54	239.01	164.18	<b>69.99% HNO<sub>3</sub></b>	1 309.89	772.02	339.66	235.76	64.20 %	54.24 %	42.11 %	43.60 %
total CSC	2 227.42	1 302.71	726.94	617.19	<b>35% HNO<sub>3</sub></b>	2 719.24	1 586.67	938.92	810.52	22.08 %	21.80 %	29.16 %	31.32 %
cathodic CSC	1 389.19	828.44	443.85	366.39	<b>35% HNO<sub>3</sub></b>	2 306.33	1 296.69	676.89	550.64	66.02 %	56.52 %	52.50 %	50.29 %
total CSC	1 204.11	728.46	336.51	229.41	<b>35% HNO<sub>3</sub></b>	1 129.76	685.57	319.09	223.36	- 6.17 %	- 5.89 %	- 5.18 %	- 2.64 %
cathodic CSC	953.94	580.49	270.36	185.06	<b>35% HNO<sub>3</sub></b>	930.84	561.95	261.14	182.66	- 2.42 %	- 3.19 %	- 3.41 %	- 1.30 %